2024

# UNDERSTANDING OF PROCESSING ADDITIVES INFLUENCE IN TIN HALIDE PEROVSKITES: CHEMISTRY, DEFECT, AND PHOTOVOLTAIC PERFORMANCE

Syed Rahmath Ullah Joy
*University of Kentucky*, syedjoydu@gmail.com
Author ORCID Identifier:
 https://orcid.org/0000-0001-6118-6388
Digital Object Identifier: https://doi.org/10.13023/etd.2024.156

Right click to open a feedback form in a new tab to let us know how this document benefits you.

UNDERSTANDING OF PROCESSING ADDITIVES INFLUENCE IN TIN HALIDE
PEROVSKITES: CHEMISTRY, DEFECT, AND PHOTOVOLTAIC PERFORMANCE

_____

DISSERTATION
_____

A dissertation submitted in partial fulfillment of the
requirements for the degree of Doctor of Philosophy in the
College of Arts and Sciences
at the University of Kentucky

By
Syed Rahmath Ullah Joy
Lexington, Kentucky
Director: Dr. Kenneth R. Graham, Professor of Chemistry
Lexington, Kentucky
2024

ABSTRACT OF DISSERTATION


UNDERSTANDING OF PROCESSING ADDITIVES INFLUENCE IN TIN HALIDE
PEROVSKITES: CHEMISTRY, DEFECT, AND PHOTOVOLTAIC PERFORMANCE

Metal halide perovskite semiconductors have attracted much interest for various applications, such as solar cells, light emitting diodes, photodetectors, and lasers, due to their excellent optoelectronic properties. Photovoltaic cell development is centered on Pb-based perovskites, which have equal photovoltaic performance compared to the traditional silicon photovoltaic. But concerns arising from the usage of toxic lead metal have motivated the research community to seek an alternative derivative. Among those, tin halide perovskites show much promise as an alternative to Pb-counterparts due to their ideal bandgap for single junction photovoltaics and similar optoelectronic properties to Pb perovskites. Nevertheless, tin perovskites suffer from easy oxidation of $Sn^{2+}$ and intrinsic p-type doping, which results in poor device performance and stability compared to their Pb-counterparts. To overcome these issues, additive engineering and formation of mixed 2D/3D perovskite phases are widely being investigated.

To select an effective additive, it is important to understand the mechanisms by which these additives act in perovskite precursor solution as well as in thin film to mitigate and stabilize the $Sn^{2+}$ oxidation. We found that additives stabilize the $Sn^{2+}$ from oxidation and alleviate the $Sn^{4+}$ concentration through halide exchange, reducing ability, and antioxidant ability. To further investigate the additives role on electronic and ionic defects, photothermal deflection spectroscopy (PDS), ultraviolet photoemission spectroscopy (UPS) and thermal admittance spectroscopy (TAS) were employed. Our results show that $FASnI_3$ perovskite films with $SnF_2$ as an additive, where $SnF_2$ is a universally used additive in tin halide perovskites, show decreased $Sn^{4+}$ formation, reduced sub-gap energy states and less ion migration due to the strong Sn-F bond and halide exchange with $SnI_4$ impurities, that help improve photovoltaic device efficiency.

KEYWORDS: Perovskite, Additives, Defect, Ion Migration, Photoemission Spectroscopies, Solar Cells.

Syed Rahmath Ullah Joy
*(Name of Student)*

05/10/2024
Date

UNDERSTANDING OF PROCESSING ADDITIVES INFLUENCE IN TIN HALIDE
PEROVSKITES: CHEMISTRY, DEFECT, AND PHOTOVOLTAIC PERFORMANCE

By
Syed Rahmath Ullah Joy

Dr. Kenneth R. Graham
Director of Dissertation

Dr. Mark Lovell
Director of Graduate Studies

05/10/2024
Date

iii

# DEDICATION

*To my  parents…*

# ACKNOWLEDGMENTS

TABLE OF CONTENTS

# LIST OF TABLES

LIST OF FIGURES

x

CHAPTER 1.  INTRODUCTION

## 1.1    General Overview of Renewable Energy

Over the past decades, energy demand has been rising as a result of the growth in the world's population and technological advancements. To tackle this demand, energy has mostly been generated from non-sustainable fossil fuel sources, such as coal, oil and gas. It is now an undebated fact that fossil fuels are the main culprit for climate change. The main trigger for climate change is greenhouse gases, such as methane, carbon dioxide, and nitrous oxide, which are emitted to the atmosphere from the burning of fossil fuels. Greenhouse gases cause to rise the global temperature at an alarming rate. In the Paris Agreement 2015, many countries have agreed to keeping the global average temperature to below 2 ºC and reaching a net-zero carbon emissions target by 2050. To achieve these goals, renewable energy considered as zero-carbon energy has attracted scientists and governments for mass deployments. Renewable energy consisting of solar energy, wind energy, hydropower, geothermal energy, biofuel, are produced from natural sources, and they are replenished than they are consumed. In 2022, 38% of total global electricity were produced from renewable sources and the remaining were from fossil fuels.[1] The fossil fuels consumption is expected to reduce to 21% in 2050, on the contrary, solar energy is expected to be responsible for over 50% of total global electricity generation in 2050.[2] More than 80% of new electricity generation capacity are from renewable energy sources over the past three years where solar energy itself is over 50%.[1] Solar energy share of global electricity generation has increased from ~3.6% in 2021 to ~4.5% in 2022. Solar

energy is expected to be the cheapest energy source of global electricity generation by 2030

compared to other renewable energy sources and fossil fuels.[2]
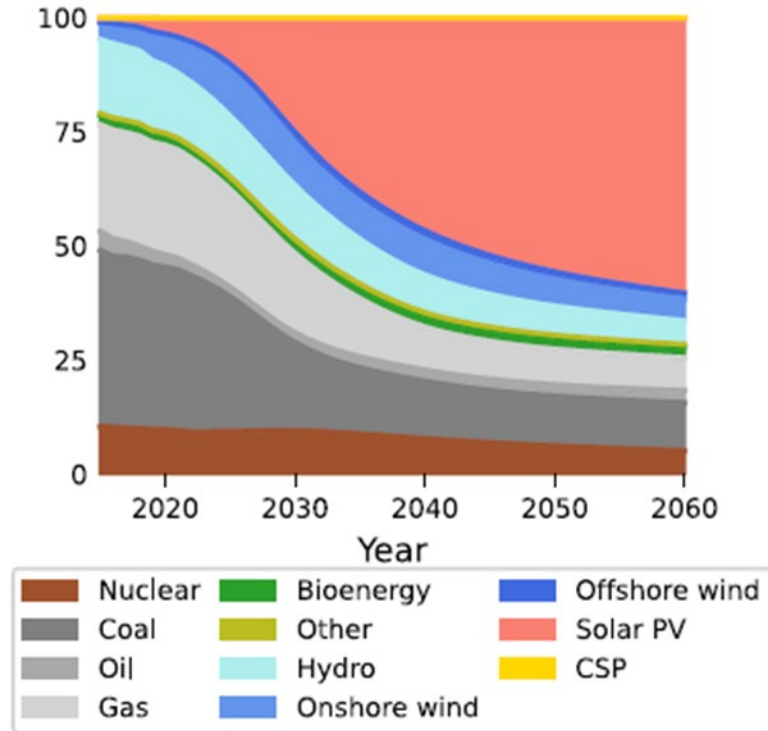


Figure 1.1 Shares of electricity production worldwide by various sources. Reprinted with permission from reference 2.

## 1.2 Materials for Solar Energy Application

Solar cells, also known as photovoltaic (PV) cells, convert sunlight to electricity.

This process is called the photovoltaic effect. When sunlight is absorbed by an active

material, electrons in the valence band are excited to the conduction band, forming bound

electron-hole pairs (excitons). These excitons are separated to free charge carriers, which

are then extracted to the external circuit to generate electricity. The first solar cell invented

by American Scientist Charles Fritts in 1883 was made of selenium, but the efficiency was

less than 1%.[3] Later in 1954, the first silicon (Si) solar cell was developed with about 6% efficiency by Daryl Chapin, Calvin Fuller, and Gerald Pearson at Bell laboratory.[4]

Solar cells can be categorized into three different types depending on the materials being used. First-generation solar cells are made of crystalline silicon, either mono or poly crystalline silicon. Silicon has an ideal bandgap of 1.2 eV and module efficiency of over 20%. It was initially used for space applications. Crystalline Si was very costly because it required high temperature and high energy during the extensive purification process of making PV grade Si crystals. However, the swift expansion of PV industries and technologies has led to a reduction in the cost of crystalline silicon over the years. The crystalline Si panel requires a thick Si layer of >100 μm to absorb adequate light energy because of their low absorption coefficient.[5, 6] This marks the beginning of second-generation PV technologies featuring thinner and more efficient light-absorbing materials.

Second-generation solar cells, also referred to as thin-film solar cells, consist of amorphous silicon (a-Si), cadmium telluride (CdTe), copper indium gallium selenide (CIGS), and gallium arsenide (GaAs). The second-generation PV technologies use vapor deposition process for fabricating thin-films, which makes it cheaper to produce than conventional crystalline silicon. The thickness of thin-film solar cells ranges from 1 to 10 μm. One such thin film technology is amorphous Si. It has a lower diffusion length of around 0.1 μm compared to the crystalline Si of order of 200 μm.[5, 6] It requires low temperature processing and low materials consumption, resulting in a shorter energy payback time. Cadmium telluride (CdTe) has a bandgap of 1.45 eV and is suitable for absorbing most of the incident light. It achieves a certified efficiency of 22.4% on the

industrial scale. Gallium arsenide (GaAs) has a bandgap of 1.42 eV and achieves the highest 27.8% efficiency certified by the national renewable energy laboratory (NREL).[7]

Third-generation solar cells consist of dye sensitized solar cells, quantum dot solar cells, perovskite solar cells, organic solar cells and copper zinc tin sulfide (CZTS) solar cells. Third generation cells also utilize a thin film approach (same as the second-generation solar cells) through the use of earth abundant materials to reduce the production cost. One of the advantages of this PV technology is that they are usually solution processed and can be employed by roll-to-roll printing techniques to achieve easily scalable production and reduce the fabrication cost. It also has tunable bandgap characteristics, which make it suitable for absorbing a wide range of visible light spectrum.[8] Over a decade, perovskite solar cells have attracted much attention with achieving an efficiency of 26.1% on the laboratory scale competing with conventional silicon. But these materials are not stable enough like silicon under thermal and light stress. Many industries and start-up companies are now devoted to commercializing perovskite technology by solving their stability issues.

## 1.3    Perovskite Materials

Perovskite, named after Russian mineralogist Lev Perovski, refers to the class of compounds which share the same type of crystal structure as the mineral calcium titanate (CaTiO$_3$).[9] The most common perovskite materials take the form of oxides, sharing a similar crystal structure to CaTiO3, with the general chemical of $A^{2+}B^{4+}(X^{2-})_3$. The general formula of halide perovskite (HP) semiconductors used for solar cell application is ABX$_3$, where A is the monovalent cation, B is the divalent metal cation, and X is the halide. HPs

consist of $Cs^+$, $MA^+$, $FA^+$ as A-site cation and $Pb^{2+}$ and $Sn^{2+}$ as B-site cation where $MA^+$ and $FA^+$ represent methylammonium and formamidinium, respectively.[10, 11] Halide perovskites are composed of a three-dimensional cubic structure of corner-sharing $[BX_6]^{4-}$ octahedra and A-site cations that occupy the cubooctahedral cavities by coordinating 12-fold X anions.[9] HPs comprise either inorganic ($CsPbI_3$) or organic-inorganic hybrid ($FA_{0.85}Cs_{0.15}PbI_3$).
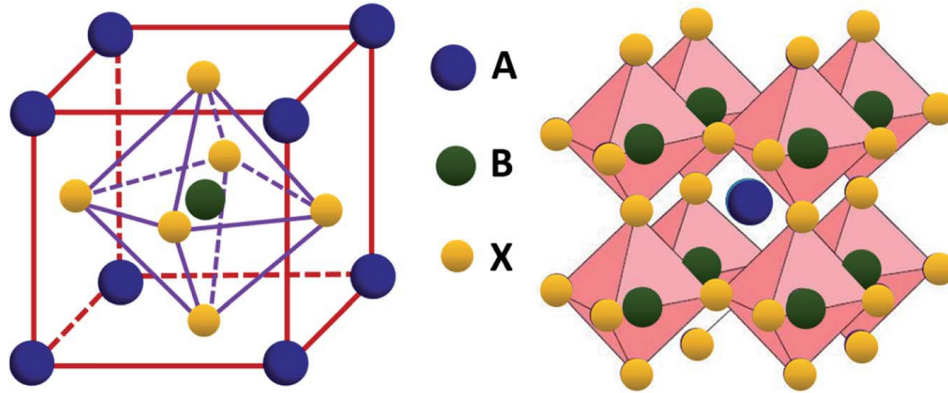


Figure 1.2 Structure of halide perovskite crystal with $ABX_3$ chemical formula. Reprinted with permission from reference 10.

In order to determine the stable perovskite structure, the Goldschmidt tolerance factor (t) is calculated using the following formula:[12]

$$t = \frac{r_A + r_X}{\sqrt{2}\,(r_B + r_X)}$$

Where $r_A$, $r_B$, and $r_X$ are the ionic radii of A-site cation, B-site cation and X-site anion, respectively. For stable cubic perovskite structure, the t value ranges from 0.80 to 1.0. $MAPbI_3$ shows cubic structure because of its t value of 0.91. A bigger or smaller cation results in a tilted/distorted structure.[13, 14] For example, $FAPbI_3$ and $CsPbI_3$ show t value ~1.0 and ~0.80, respectively. The size of FA and Cs cation is bigger and smaller than MA

5

cation, respectively, which results in distorted perovskite crystal. When Cs is incorporated into FAPbI$_3$ to form hybrid FA$_{0.85}$Cs$_{0.15}$PbI$_3$ composition, t value is lowered down to 0.95, leading to ideal cubic structure and more stability at room temperature.[15]

1.4    Lead-based Perovskite Photovoltaics Development

Although hybrid HPs were explored for application in light emitting diodes and transistors in the late 20th century, an outburst of interest of these materials in solar cell application started in the early 21st century.[16] In 2009, Miyasaka and coworkers first reported the use of methylammonium lead bromide (MAPbBr$_3$) and methylammonium lead iodide (MAPbI$_3$)  as sensitizers for dye-sensitized solar cell with power conversion efficiency of 3.1% and 3.8%, respectively.[17] Later in 2012, Kanatzidis and coworkers first reported all solid-state perovskite PV with 10.2% efficiency.[18] After a decade of tremendous efforts, perovskite solar cells (PSCs) have achieved the highest efficiency of 26.1%, similar to single-junction crystalline silicon PVs. The most efficient PSCs are made of Pb-based HP materials. The astonishing PV performance of these materials can be attributed to their excellent optoelectronic properties, such as tunable bandgap, high absorption coefficient, low exciton binding energy, high carrier mobility, long diffusion length, and most importantly, it can be solution-processed, which lowers the fabrication cost.[16]

HP solar cell structures can be classified as mesoporous, n-i-p (regular), and p-i-n (inverted) structure.[19] Planar regular and inverted structures consist of a transparent conductive electrode (TCO), hole transporting layer (HTL), perovskite absorber layer, electron transporting layer (ETL), and counter electrode. The most common HTLs are

6

PTAA, PEDOT:PSS, Spiro-OMeTAD and $NiO_x$. The commonly used ETLs are $C_{60}$, PCBM, and $SnO_2$. The inverted structure requires lower processing temperature than regular structure, leading to even lower fabrication cost. In the mesoscopic structure, a mesoporous metal oxide layer *e.g.,* $mp-TiO_2$ and $mp-Al_2O_3$ is used on top of a compact $TiO_2$ layer. The problem of this structure is that it needs high temperature to process $mp-TiO_2$ layer and device shows high hysteresis.[19]
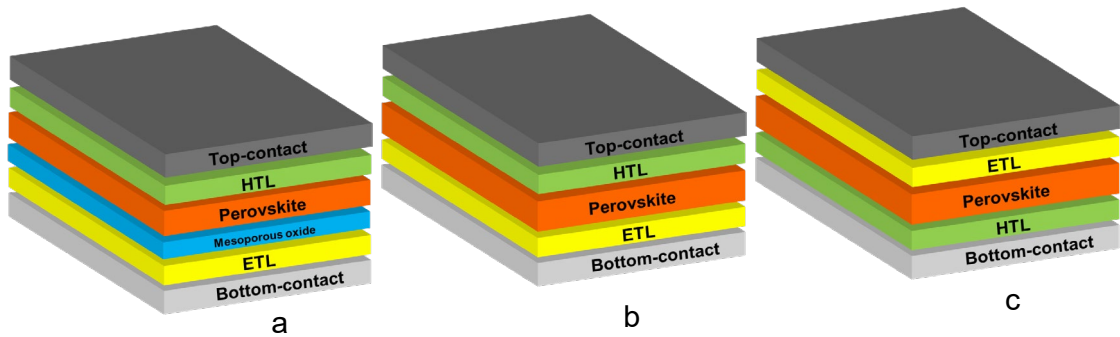


Figure 1.3 Schematic device structures of a) mesoporous (n-i-p), b) conventional (n-i-p), and c) inverted (p-i-n).

### 1.4.1 Fabrication of Perovskite Film

Various fabrication techniques such as spin coating,[20] blade coating,[21] slot-die coating,[22] spray coating,[23] ink-jet printing,[24] screen printing[25] etc. have been used to deposit HP film. For laboratory scale research, spin coating is a widely chosen technique to make high quality perovskite films, but it is only suitable for small-area PV devices. For large-area devices, blade coating, slot-die coating, spray coating, ink-jet printing, screen printing etc. are suitable scalable deposition techniques for scaling up HPs PV technology. The PV performance loss of large-area devices is higher than small-area devices since film coating is not uniform over a large area, resulting in higher series resistance and shunting loss. In

recent years, significant progress has been made to scale up the efficiency of large-area perovskite PV modules.[26, 27]

In spin-coating technique, the HP film is fabricated through one-step and two-step deposition methods. An antisolvent dripping is a crucial stage in the one-step process. Antisolvent dripping facilitates the heterogenous nucleation followed by immediate supersaturation of solution and formation of an intermediate adduct.[27] This intermediate adduct phase controls the kinetics of perovskite crystal growth during thermal annealing. Antisolvents such as chlorobenzene, toluene and diethyl ether in which perovskite precursor salts are insoluble are typically used to drip onto the perovskite film while spinning. Perovskite precursors, for example MAI and $PbI_2$ to make $MAPbI_3$ perovskite, are dissolved in a mixed-solvent DMF and DMSO system. Tuning of the ratio of mixed-solvent system and their interaction with the antisolvent are the keys to obtaining better morphology of the resultant film.[27, 28]
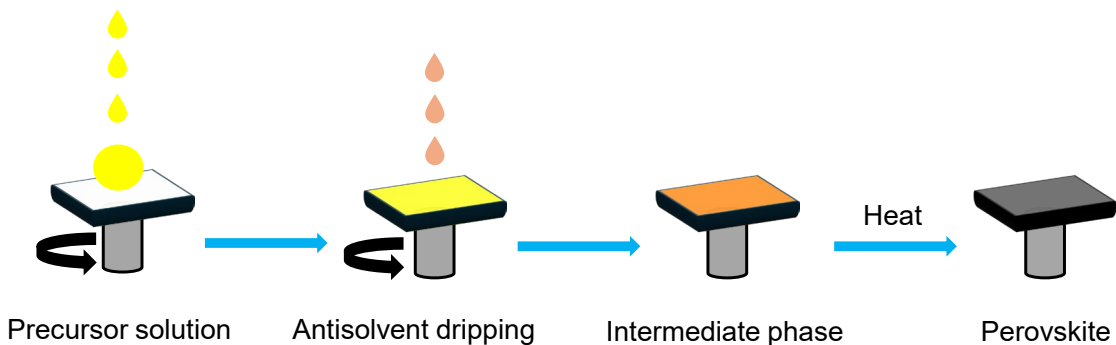


Figure 1.4 One-step process of halide perovskite film fabrication.

HP film can be fabricated through a two-step route where first lead halide salt is deposited followed by the conversion to perovskite phase upon reaction with organic halide salt. The disadvantage of the two-step process is that it takes a long time to convert lead halide salt to corresponding perovskite, which results in incomplete reaction, small grain sizes, and high density of pinholes. Despite this issue, it can be adapted to make uniform film over a large area and is suitable for upscaling large-area PV modules. Approaches such as solvent and additive engineering, or developing new precursor materials, can be utilized for further development.[29]
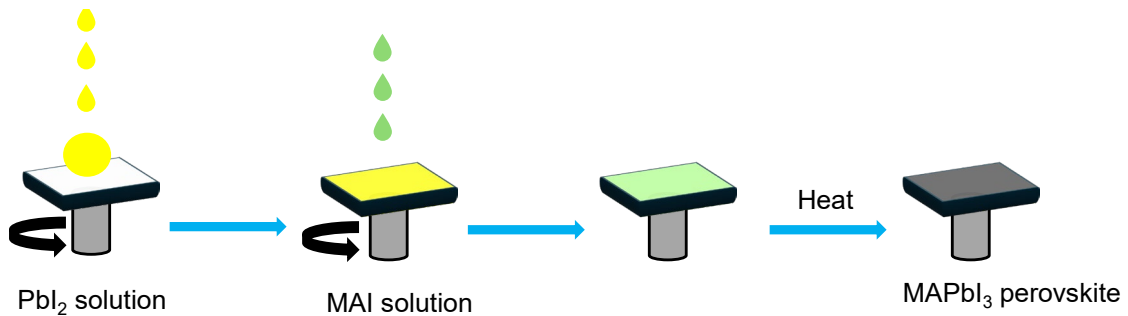


Figure 1.5 Two-step process of MAPbI$_3$ perovskite film fabrication.

### 1.4.2 Dimensionality of Perovskite Materials

3D HP materials are easily degraded under different stresses such as moisture, oxygen, light, heat, and bias. To address this issue, mixed 2D/3D phase of HPs are significantly studied due to their enhanced stability compared to 3D perovskite. Mixed 2D/3D HPs can be formed either by introducing bulky organic cations into 3D precursor solutions or treating the surface of 3D HP film using large organic cations.[30] The ammonium-based (R-NH$_3^+$) cation is commonly used to form mixed 2D/3D perovskite phase. There are different classes of quasi-2D or mixed 2D/3D HPs, but among those

Ruddlesden-Popper (RP) hybrid HP structures are widely studied.[30] The general formula of RP crystal structure is $(RNH_3)_2A_{n-1}B_nX_{3n+1}$, (n = 1, 2, 3, 4 ... $\alpha$), where $[A_{n-1}B_nX_{3n+1}]^{2-}$ represents the common parent 3D perovskite layer which is isolated by a large aromatic or aliphatic $R-NH_3^+$ spacer cation. Pure 2D phase forms when n=1 and n=$\infty$ represents 3D phase.[31]
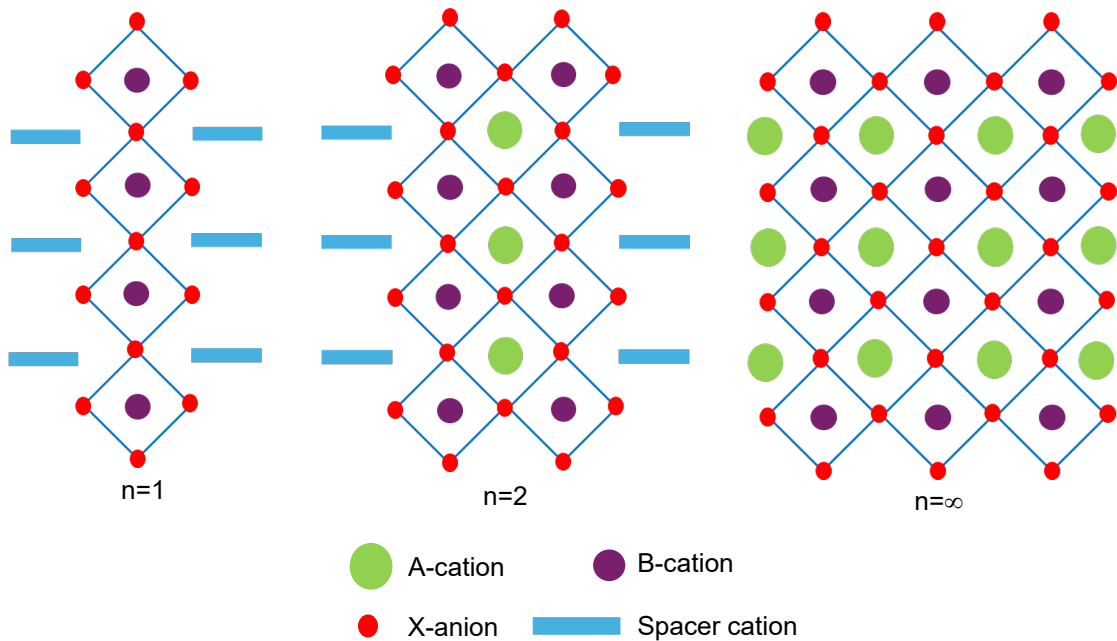


Figure 1.6 Different dimensions of perovskite structures; pure 2D (n=1), quasi 2D (n=2), and 3D (n=$\infty$).

Due to the large size of these cations, 2D/3D structures show higher defect tolerance ability. Also, the hydrophobic nature of these cations retards the ingression of moisture into the 3D phase, resulting in improved stability. However, large spacer cations impede the charge transport in the material, which results in decreased PV efficiency as compared to the 3D material. The optoelectronic properties of quasi-2D perovskites can be tuned by varying the n value and R group.[32] In 2014, Karunadasa first used the quasi-2D

10

$(PEA)_2(MA)_2Pb_3I_{10}$ material as an absorber layer and achieved 4.73% PV efficiency.[33] In 2022, Wolf reported 22.4% efficiency of 2D/3D phase by tailoring the dimensionality at the heterojunction interface, and the device retained >95% of the initial value after >1000 hours at 85 ºC and 85% relative humidity.[34]

### 1.4.3   Defect in Perovskite Materials

Defects can be formed in crystalline semiconducting materials either unintentionally *i.e.*, when they are being synthesized and/or processed, or intentionally by introducing foreign impurities *i.e.*, doping. In reality, the presence of defects is unavoidable in semiconductors, and it also exists in HP materials. Figure 2.1 depicts the native point defects, for example vacancies, interstitials, anti-site substitutions, Frenkel pair defects, Schottky defects etc., and higher-dimensional defects, for example dislocations, grain boundaries, voids, and precipitates, formed in HP semiconductors. In the case of $MAPbI_3$ perovskite, point defects such as vacancies $V_{MA}$, $V_{Pb}$, and $V_I$; interstitials $MA_i$, $Pb_i$, and $I_i$; and anti-sites $MA_{Pb}$, $MA_I$, $Pb_{MA}$, $Pb_I$, $I_{MA}$, and $I_{Pb}$ can be present.[35, 36] The lower the formation energy, the easier it is for certain types of defects to be formed. Different growth conditions *i.e.*, atomic and electronic chemical potentials affect the formation energy of defects.[35]
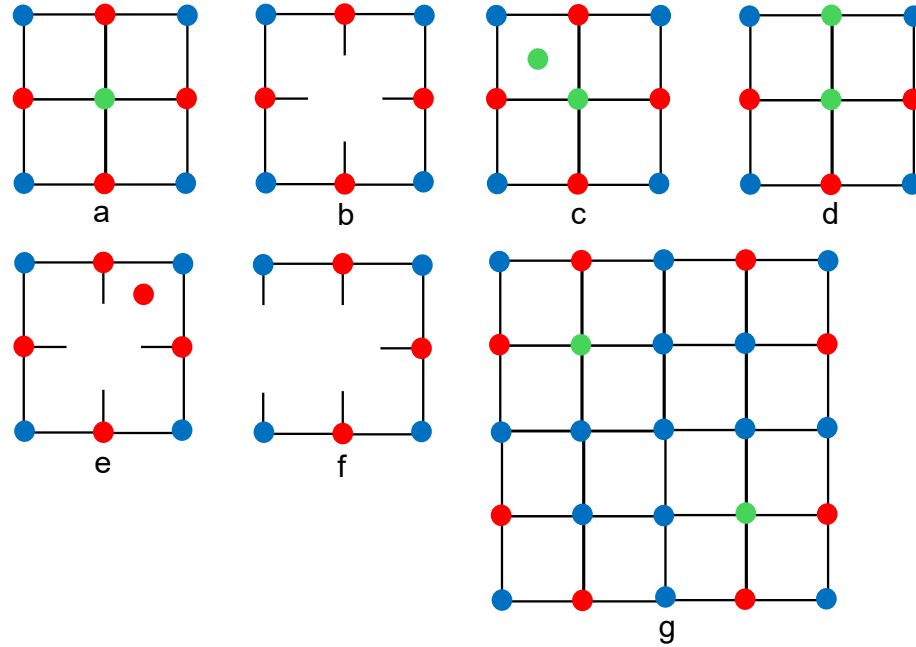
Figure 1.7 Different types of defects of perovskite materials; a) perfect crystal, b) vacancy ($V_B$), c) interstitial ($A_i$), d) anti-site ($A_X$), e) Frenkel defect, f) Schottky defect, and g) precipitate. Green, blue, and red circles represent A-cation, B-cation, and X-anion, respectively.

Defects can form additional energy levels in the band gap, and it can be divided into two general categories based on the energy level of the defect relative to the band edge, *i.e.*, shallow level and deep level. When the energy level is close to the valence band maximum (VBM) and conduction band minimum (CBM), it is referred to as shallow-level trap, and when the energy level locates at middle third of the band gap, it is termed as deep-level trap (Figure 2.2). Charges can easily be released from the shallow-level traps to the band edges at elevated temperature, but it cannot be easily de-trapped from deep-level traps.[37] Therefore, deep-level traps are more detrimental and negatively affect the charge carrier density, carrier lifetime, and diffusion length.[38] Since perovskite consists of ionic species, these ions are also responsible for defect-mediated migration phenomenon. It is now established that hysteresis in J-V scan originates from migration of ions, and these

mobile ionic species are responsible for device degradation under light illumination.[39, 40] Therefore, defect management is indispensable to improve perovskite PV device efficiency and stability.
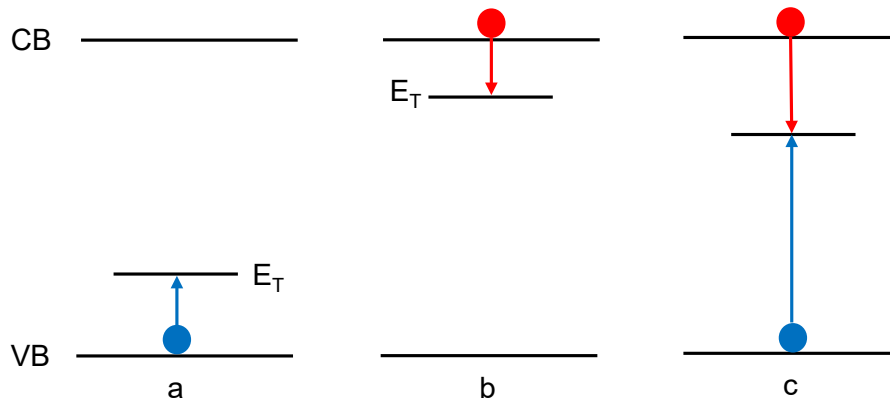


Figure 1.8  Hole (a) and electron (b) captured or trapped by a defect of $E_T$ energy level, and hole-electron recombination at a trap level (c).

### 1.4.4   Lead Toxicity

To date, all of the most efficient PSCs utilize heavy-metal Pb as a B-site cation. Using toxic Pb element in PSCs can pose adverse effects to the environment and human health when exposed to nature. The maximum accepted value for Pb content in drinking water and air is 15 and 0.15 µg/L, respectively, regulated by the EPA. When MAPbI$_3$ reacts with water, a decomposition reaction takes place through the formation of methylamine (CH$_3$NH$_2$), hydroiodic acid (HI), and lead iodide (PbI$_2$). The solubility product (K$_{sp}$) of PbI$_2$ is on the order of $10^{-8}$, whereas other heavy-metals (CdS, PbS, CdTe) have much lower K$_{sp}$ values ranging from $10^{-27}$ to $10^{-34}$.[41] One study found that lead from halide perovskite is 10 times more bioavailable and more dangerous than other lead sources already presents in the ground.[42] Organic cation from halide perovskite can also alter the soil pH and increase the lead uptake of plants grown in soil containing PbI$_2$.[42] One should consider

eliminating or minimizing the Pb content from perovskite PVs. The possible option is to replace $Pb^{2+}$ from halide perovskites with a promising alternative with similar optoelectronic properties as $Pb^{2+}$. To do so, divalent cations such as $Sn^{2+}$, $Ge^{2+}$ and $Cu^{2+}$ were explored as an alternative. Another viable route is to make double perovskite structure where the divalent cation is replaced by one monovalent ($Ag^+$) and one trivalent cation ($Bi^{3+}$, $Sb^{3+}$, $In^{3+}$).[43, 44] Among those, tin ($Sn^{2+}$) is considered as the most promising alternative to $Pb^{2+}$.

## 1.5 Lead-free Tin-based Perovskite Photovoltaics

Both Sn and Pb are the same group elements and have similar electronic configuration. Sn has excellent optoelectronic properties like Pb, including low bandgap (~1.3 eV), high absorption coefficient, small exciton binding energy, and high charge-carrier mobility etc. According to the Shockley-Queisser theoretical limit,[45] a maximum efficiency of 33.7% can be achieved with a bandgap of 1.34 eV from a single-junction solar cell. In that case, $ASnI_3$ perovskites (A=FA, MA, Cs) show bandgap of between 1.3 to 1.4 eV, which is less than their Pb analogs (>1.5 eV) and near the Shockley-Queisser theoretical limit.[46] Therefore, Sn perovskites have the potential to attain better PV performance compared to their Pb counterparts.

First in 2012, Kanatzidis and coworkers used $CsSnI_3$ as a hole transporting material in dye-sensitized solar cells and obtained 10.2% efficiency.[18] Later in 2014, Snaith and coworkers first employed $MASnI_3$ absorber layer in a mesoscopic structure and achieved 6.4% efficiency.[47] In the same year, Kanatzidis and coworkers achieved maximum 5.7% efficiency where $MASnI_{3-x}Br_x$ (X=1,2, and 3) perovskites were used as an active layer.[48]

After that, enormous efforts have been devoted to improving the performance of Sn perovskite PVs. To date, a maximum efficiency of 14.8% is obtained, though it is far less than their Pb analogs.[49]

The main impediment to better performance of Sn-PSCs is the intrinsic instability of the $Sn^{2+}$ oxidation state. Due to the lack of lanthanide shrinkage, $Sn^{2+}$ easily oxidizes to stable $Sn^{4+}$ state, whereas in the case of Pb, $Pb^{2+}$ is the stable oxidation state required for perovskite structure stability.[50] Moreover, self p-doping characteristic increases the background hole density, resulting in metallic nature and high defect concentration of Sn perovskites. Despite these disadvantages, Sn is less toxic than Pb. When Sn halide perovskites are exposed to air and water, it decomposes to form water insoluble $SnO_2$, which is in $Sn^{4+}$ state, as a degradation product.[51] The low water solubility of the Sn product means reduced bioavailability. The Sn uptake by the plants grown in the Sn perovskite-contaminated soil is far less than Pb uptake.[42] Therefore, it is concluded that Sn perovskites are the most promising candidate for the replacement of Pb if their intrinsic instability issues are solved or minimized.

1.6    Conclusion and Outline

Perovskite semiconductor-based materials show much promise for solar cell applications and are considered as next-generation solar materials due to their excellent optoelectronic properties. They can be solution-processed and are more cost-effective than the other existing technologies. Research communities and many industries are working together to commercialize perovskite PVs sooner rather than later. Although this technology shows similar PV efficiencies as traditional crystalline silicon, all

developments are centered on Pb-based perovskite materials. We can't neglect the environmental and health risks caused by Pb usage. Sn-based perovskite can be a good alternative since it shows similar optoelectronic properties as Pb and most importantly it is less toxic than Pb derivatives. The intrinsic instability of Sn-perovskites resulting from the $Sn^{2+}$ oxidation is the main reason for their poor PV performance compared to their Pb-analogs. Approaches such as additive engineering and forming mixed 2D/3D phases are considered as effective routes to mitigate their instability issues.

This dissertation will discuss the aspects of additives used in tin perovskites to suppress $Sn^{2+}$ oxidation and decrease defect densities in the materials. Chapter 2 discusses the application of photothermal deflection spectroscopy (PDS) and ultraviolet photoemission spectroscopy (UPS) to characterize the electronic defect states, and characterization of photovoltaic device. Chapter 3 discusses the use of thermal admittance spectroscopy (TAS) to determine the activation energy of mobile ionic defect species in $FASnI_3$ perovskite solar cell. Chapter 4 investigates the fundamental understanding of additive functions to decrease $Sn^{4+}$ concentration in tin perovskite thin films. Chapter 5 examines why $SnF_2$ is a better additive for tin perovskites than other $SnX_2$ additives in terms of electronic and ionic defects.

CHAPTER 2.  METHODS

## 2.1    Photothermal Deflection Spectroscopy

Photothermal deflection spectroscopy (PDS) is an important tool to measure the sub-band gap states or defects in the materials. The sub-band gap states contribute to trap-assisted non-radiative recombination. The absorption coefficient of the sub-band gap states gives rise to tail states near or at the band edge. The absorption coefficient in the tail states decreases exponentially as the photon energy decreases below the bandgap energy.[52-54] An exponential decaying of the absorption onset tail near the band edge is referred to as Urbach tail or Urbach energy ($E_U$). The Urbach energy can be calculated by using the following equation:

$$ln\alpha = \frac{1}{E_U}E - \frac{E_g}{E_U} + ln\alpha_0$$

where, $\alpha$ is the absorption coefficient, $\alpha_0$ is the material dependent constant, E is the photon energy, $E_g$ is the band gap energy.

The Urbach energy can be extracted from the inverse slope of the linear fit using the above equation. $E_U$ quantifies the energetic disorder present at the band edge in the materials. The $E_U$ value depends on the steepness of the exponential function. The steeper the slope, the less the $E_U$. In other words, the smaller the $E_U$ value, the less energetic disorder and less band-edge defects are present in the material. The PDS spectra are presented as plots of PDS signal or absorption coefficient vs. photon energy. A sample PDS spectrum of FASnI$_3$ perovskite sample is shown in Figure 2.4a. The shaded area is characterized as the tail states region. A linear fit to the absorption onset tail determines the Urbach energy ($E_U$) as shown in Figure 2.4b of a FASnI$_3$ sample.
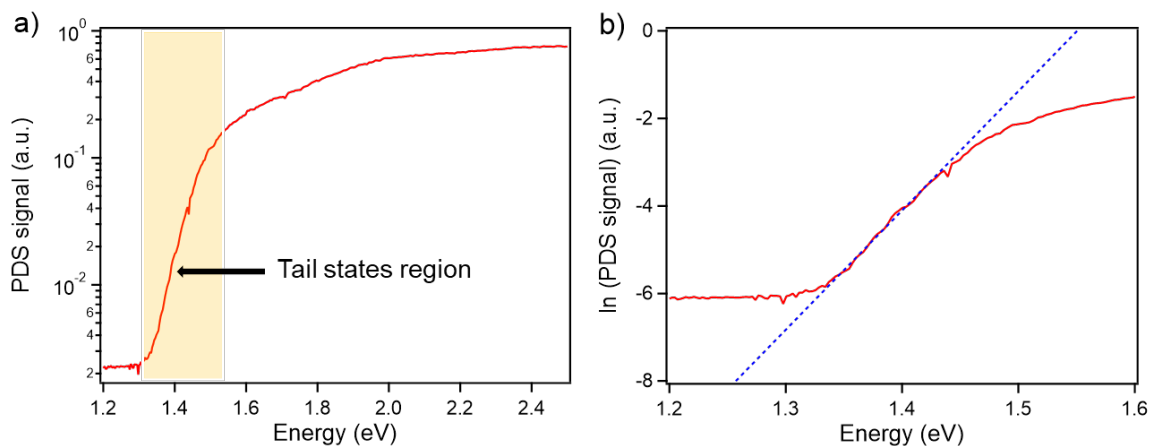
Figure 2.1 a) PDS spectra on a semi-log plot and b) taking the natural log of the PDS signal to extract the Urbach energy ($E_U$) of FASnI$_3$ perovskite thin film.

Figure 2.3 shows the schematic diagram of the PDS system. PDS uses the deflection of a probe beam travelling parallel to a sample surface to detect minute changes in temperature via the mirage effect.[55]  The sample, in this case the perovskite film, is immersed in a perfluorohexane (Fluorinert) liquid that has a high thermo-optic coefficient but does not react with the perovskite film.  A 300 W Xe Arc lamp that is coupled into a 1/8-meter monochromator and chopped at 4 Hz is focused onto the sample perpendicular to the probe beam, which causes a periodic temperature change in the sample.  This periodic temperature change is conveyed to the Fluorinert fluid whose changing index of refraction causes a periodic deflection of the ~100 μm diameter probe beam.  The position of the probe beam is monitored with a quad-cell photodiode and fed into a lock-in amplifier along with the 4 Hz chopper reference signal.
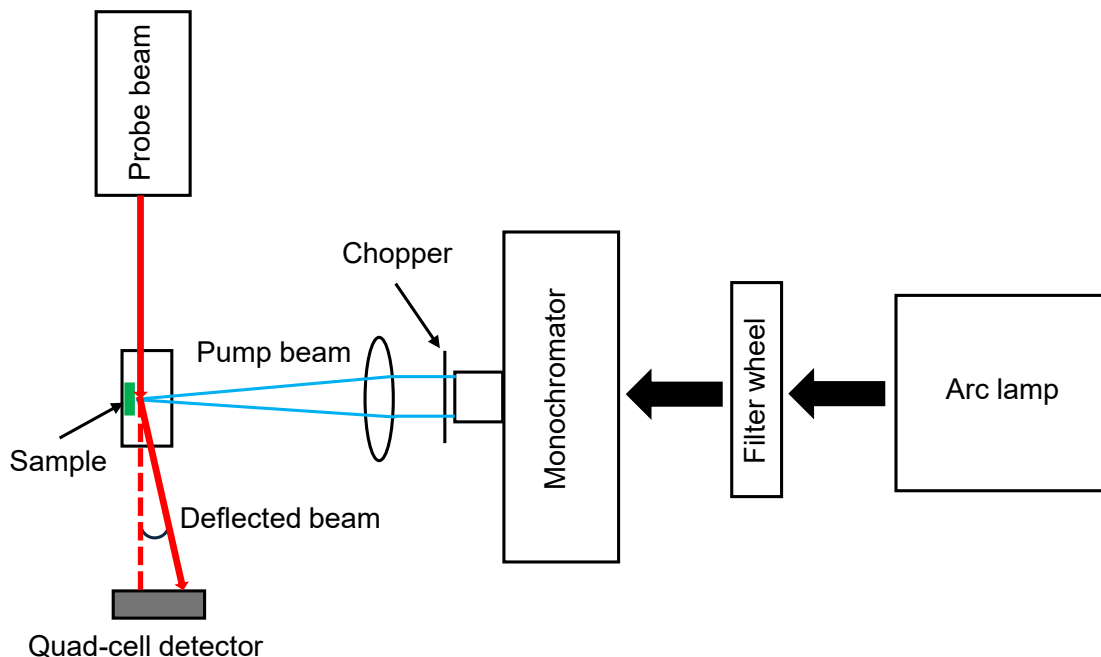
Figure 2.2 Schematic diagram of PDS instrument set-up.

## 2.2 Ultraviolet Photoemission Spectroscopy

Ultraviolet photoemission spectroscopy (UPS) measures the kinetic energy of photoelectrons emitted from a sample upon absorbing the ultraviolet light, typically in the higher energy vacuum ultraviolet range with photon energy of >6.2 eV. Since this energy of photons can only excite electrons from the valence band (VB) region, therefore UPS technique is used to characterize the electronic structure of VB region of semiconductor materials. The photoelectric effect is the basis for UPS measurements, where the kinetic energy of emitted electron is determined by the equation: $KE = hv - BE - \phi$, where KE is the kinetic energy of emitted photoelectron, BE is the binding energy of photoelectron in the solid, and $\phi$ is the work function of the sample. Figure 2.3 shows the important parameters determined from the UPS measurement.
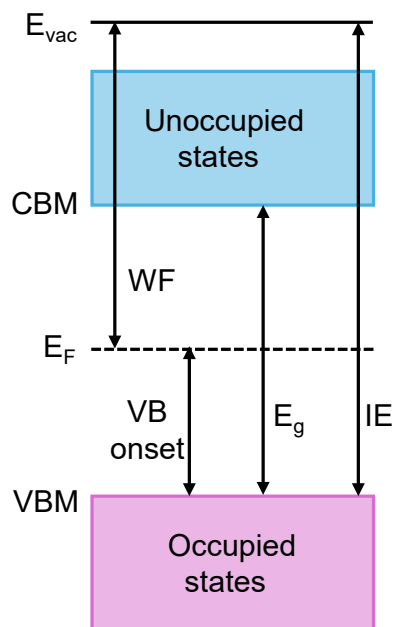
Figure 2.3 Schematic representation of energetics determined from the UPS measurement.

Work function (WF) defines the minimum energy required to remove an electron from a solid surface to the vacuum level. Vacuum level ($E_{vac}$) describes the energy of an electron at rest outside of the solid. Fermi level ($E_F$) is the hypothetical energy level of an electron at thermodynamic equilibrium with 50% probability of being occupied at any time. HOMO or VBM is the highest occupied orbitals (for organic semiconductors) or valence band maxima (for inorganic semiconductors). LUMO or CBM is the lowest unoccupied orbitals (for organic semiconductors) or conduction band minima (for inorganic semiconductors). Band gap ($E_g$) is the energy difference between the VBM/HOMO and CBM/LUMO. Ionization energy (IE) defines the energy required to remove an electron from the VBM/HOMO to $E_{vac}$.

Figure 2.4 shows the schematic diagram of our UPS measurement set-up that is installed in our PHI 5600 UHV system. Helium discharge lamp is the most common photon source (21.2 eV) used for UPS measurements. The drawback of this high energy light source is that it can induce significant sample damage and surface charging effect for organic semiconductors.[56, 57] In our system, a vacuum ultraviolet (VUV) light source (Excitech E-LUXTM 12) with photon energy of 10.2 eV is used for the measurement to avoid sample damage and charging.[58] Low-energy H Lyman-α emission line UV beam is passed through a vacuum chamber filled with ultrapure oxygen or nitrogen gas and reflected by a 90º mirror to the ultrahigh vacuum (UHV) chamber. A -5 V bias is applied between the sample and electron analyzer to accelerate the secondary electrons generated from the sample and enable the electrons with KE=0 to reach the detector.
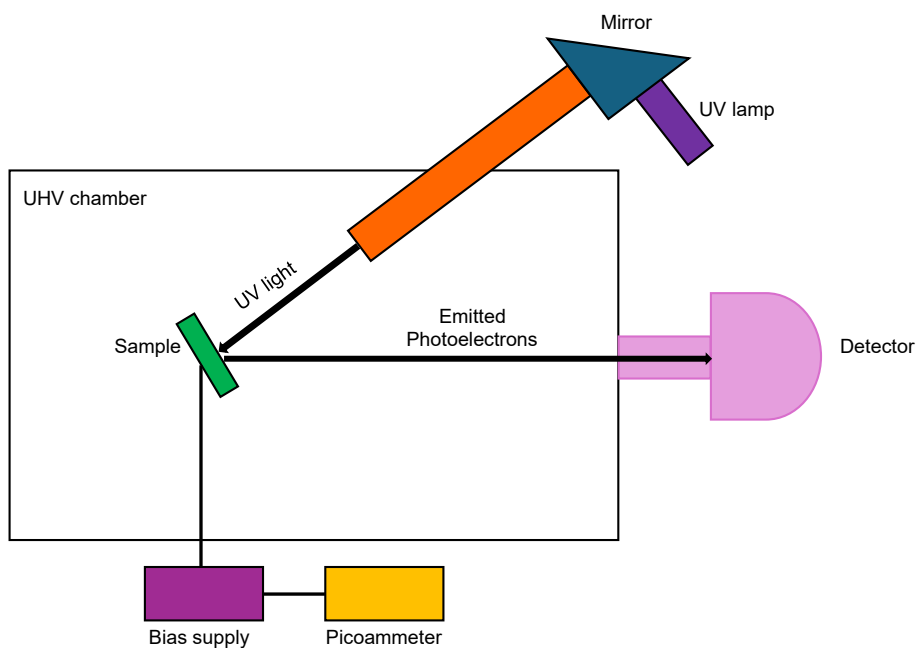


Figure 2.4 Schematic diagram of UPS instrument set-up.

UPS spectra are usually presented as a plot of intensity vs. binding energy with respect to the Fermi energy ($E_F$= 0 eV). A sample UPS spectrum of FASnI$_3$ perovskite film is shown in Figure 2.5. The key two key features i.e., secondary electron cut-off (SECO) and VB onset energy are determined from UPS spectrum. SECO is higher binding energy electrons that have zero kinetic energy after leaving from the sample surface and they can only overcome the work function of the material. Thus, work function of the material can be calculated by subtracting the SECO energy from the photon energy *i.e.*, $WF = (10.2 - SECO)\ eV$. VB/HOMO onset is at the lowest binding energy region, and corresponds to the energy difference between the Fermi level and highest occupied state/valence band maxima (VBM) level *i.e.*, $VBM = (WF + onset)\ eV$. For organic semiconductors, HOMO onset can be determined by a linear fit at the onset region (as shown in Figure 2.5a) due to higher density of states at the band edge, however, in the case of some inorganic materials *i.e.*, metal halide perovskite materials, a gaussian fit approach is used to determine the VB onset energy since they have lower density of states at the band edge (as shown in Figure 2.5b).[59] Based on defect densities at the band edge, VB onset moves towards or away from the Fermi level that can give insight into the defects in the materials. For example, if there is more $Sn^{4+}$ concentration in FASnI$_3$ sample, then VB onset moves towards the Fermi level corresponding to more p-type characteristic, and vice-versa. This provides indirect information about the defect densities in FASnI$_3$ film.
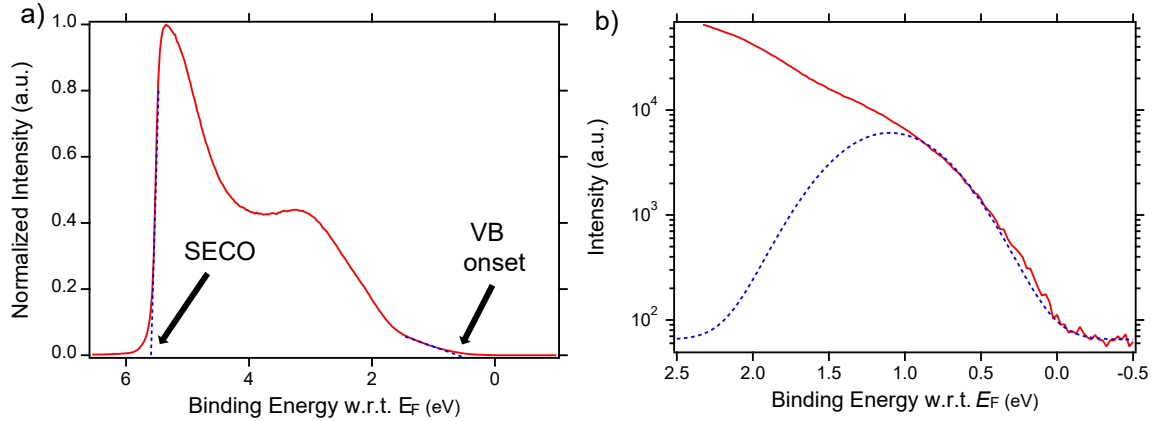
Figure 2.5 a) Sample UPS spectrum and b) Semi-log plot with the Gaussian fit used to extract the VB onset energy of FASnI$_3$ perovskite film.

## 2.3    Characterization of Photovoltaic Device

The power conversion efficiency (PCE) of a photovoltaic device is defined as the ratio of electrical energy output power to incident solar energy input power. For solar input power, standardized illumination systems such as AM0, AM1, or AM1.5 are embraced across the research community. AM stands for air mass and number stands for the path length of solar irradiance passing through the atmosphere. AM0 means solar light has not passed through none of the atmosphere that is used to test solar cells designed for space applications. AM1.5 denotes the solar irradiance passes through 1.5 atmospheres at an angle of 48° from the zenith and is received on a titled surface positioned at 37°. AM1.5 is the widely adopted illumination system at a terrestrial level and provides 100 mW/cm$^2$ solar power.

The electrical output power is determined by multiplying current and voltage under illumination. PV device is characterized by measuring the current while voltage is swept under continuous standardized light exposure. The measured current is converted  to

current density (J) by dividing the PV device area. From current density-voltage (J-V) scan, parameters such as short-circuit current ($J_{SC}$), open circuit voltage ($V_{OC}$) and field factor (FF) are determined. The $J_{SC}$ and $V_{OC}$ denote maximum current obtainable at negligible or zero resistance, and maximum voltage attainable at infinite resistance from the device under illumination, respectively. The FF is determined from the ratio of maximum power generated by the device to the maximum power achievable theoretically. FF can be determined by using the equation below:

$$FF = \frac{J_{MP} \times V_{MP}}{J_{SC} \times V_{OC}}$$

Finally, PCE is calculated from the following equation:

$$PCE = \frac{J_{sc} \times V_{oc} \times FF}{P_{in}}$$
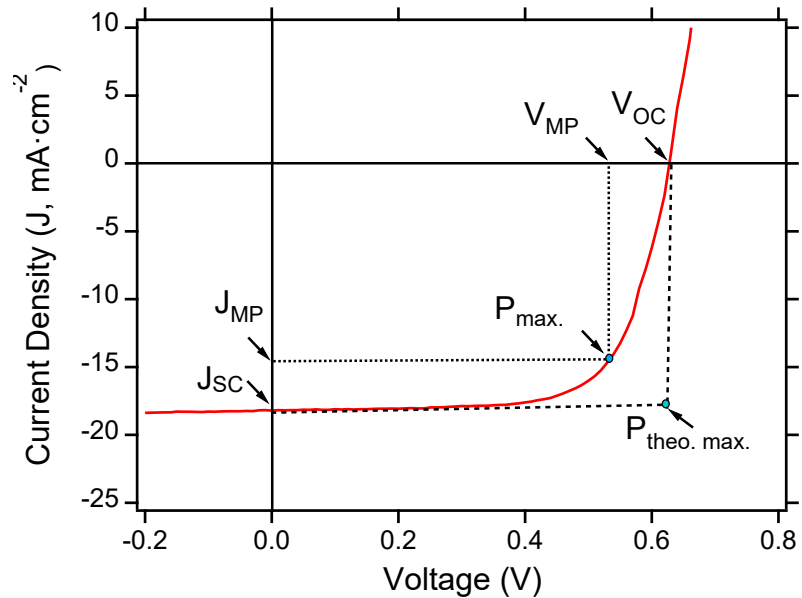


Figure 2.6 Sample J-V curve of a PV device measured under AM1.5 illumination condition.

# CHAPTER 3.  THERMAL ADMITTANCE SPECTROSCOPY TO DETERMINE THE ACTIVATION ENERGY OF ION MIGRATION IN TIN HALIDE PEROVSKITE SOLAR CELLS

## 3.1    Introduction

Ion migration is a common phenomenon in hybrid halide perovskites. Ionic transport in halide perovskites typically involves the movement of ions by hopping through defect sites. For example, halide ions can migrate through halide vacancies to the perovskite/charge transporting layer interface, that can increase the junction capacitance and bring about electrochemical reaction at the interface, resulting in interface energetic modification and non-radiative recombination of charge carriers. Ion migration under external driving forces such as voltage, light, and temperature results in poor efficiency and stability of the photovoltaic device and hysteresis in current-voltage curve.[60, 61] Therefore, mitigation of ion migration is necessary to improve overall device performance and stability.

Thermal admittance spectroscopy (TAS) was first proposed by Walter et al.[62] and applied to inorganic solar cells to investigate the defect distribution.[63, 64] Now, it has been a widely employed technique to characterize the defect distribution in organic solar cells and perovskite photovoltaics.[65-67] By using TAS, the activation energy of ion migration can also be calculated in perovskite solar cells. The smaller the activation energy, the more readily the ion migration of specific type of ionic defects will occur.

In a TAS measurement, the capacitance is measured as a function of frequency under a small AC voltage perturbation with varying temperature.[63, 68, 69] Any diode-like device such as a solar cell acts as a parallel-plate capacitor, and the width of the space

charge region and junction capacitance can be modulated by changing applied AC voltage when device is operating at zero bias condition.
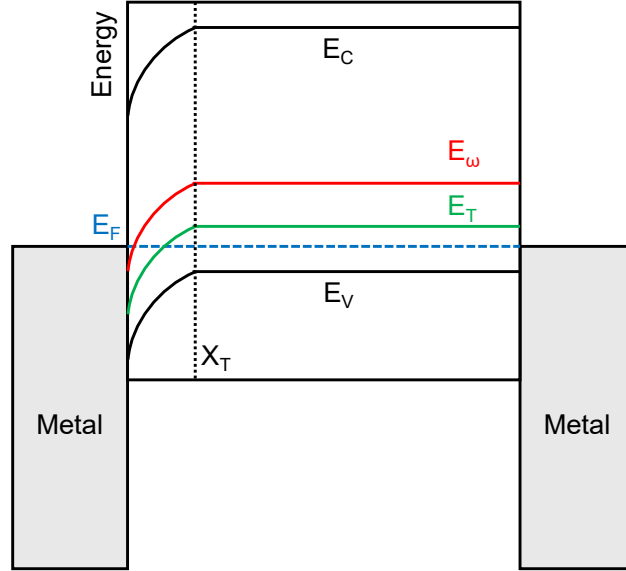


Figure 3.1 Schematic diagram of band bending in a p-doped Schottky junction with a trap state located at $X_T$ position with $E_T$ energy level. $E_\omega$ is the deepest level of trap state to be detected. $E_V$ and $E_C$ are the valence band and conduction band energy level, respectively.

Figure 3.1 shows the band diagram of a Schottky device with p-type active layer sandwiched in between two metal electrodes. The trap energy level ($E_T$) in the space charge region is filled with electrons up to the Fermi level ($E_F$), and those traps can be charged and discharged by applying an AC voltage. When a small AC voltage with an angular frequency ($\omega=2\pi f$) is applied, trap states position near $X_T$ will be redistributed due to the change of band bending which contributes to the junction capacitance. If the angular frequency of the AC voltage is higher than the emission rate of the trap states, then trap states will not respond to the applied AC signal and will not contribute to the junction

capacitance. In other words, if the AC frequency is lower than the emission rate, trap states will respond to the AC signal and increase the junction capacitance.

The emission rate $(e_p)$ of trap states can be expressed as:[70]

$$e_p = N_V v_{th} \sigma_p \exp\left(\frac{-E_T}{kT}\right) = \xi T^2 \exp\left(\frac{-E_T}{kT}\right) = \omega_0 \exp\left(\frac{-E_A}{kT}\right) \qquad (1)$$

where $N_V$ is the effective density of states of the valence band, and $v_{th}$ is the average thermal velocity. Here, it is assumed that $N_V$ and $v_{th}$ are the temperature dependent parameters with $N_V \propto T^{3/2}$ and $v_{th} \propto T^{1/2}$. Therefore, $\omega_0$ is the temperature independent attempt-to-escape angular frequency of the trap state *i.e.*, $\omega_0 = 2\pi f_0 T^2$. $\sigma_p$ is the capture cross section of the trap state, $k$ is the Boltzmann's constant, $T$ is the temperature, and $E_A$ is the trap activation energy w.r.t. to the valence band.

A trap state near $X_T$ location with $E_T$ energy depth to the band edge equals to the demarcation energy $E_\omega$. This demarcation energy defines the maximum depth of a trap state level that can be detected by the AC signal at a given angular frequency $(\omega)$ and temperature $(T)$. For a specific trap state, demarcation frequency $\omega_0$ equals to the trap emission rate $(e_p)$. When the applied AC frequency $\omega$ is lower than the $\omega_0$, the trap states will respond to the AC frequency and increase the junction capacitance, but when $\omega > \omega_0$, trap states will not contribute to the capacitance. Therefore, demarcation energy $E_\omega$ can be derived from equation (1) as follows:

$$E_\omega = kT \ln\left(\frac{\omega}{\omega_0}\right) \qquad (2)$$

where, $\omega$ is the angular frequency of the applied AC signal. Thus, $E_\omega$ can be swept from near the band edge to the mid-gap by decreasing $\omega$ or increasing $T$.

The trap emission rate $(e_p)$ can be denoted as the characteristic frequency $(\omega_p)$ at which the trap peak occurs at a given temperature. The characteristic peak frequency $(\omega_p)$ at each temperature can be found by plotting the derivative of capacitance with respect to the applied frequency $i.e., -\omega.\frac{dC}{d\omega} \, vs. \, \omega$. Following that, equation (1) can be written as:[70]

$$\ln\left(\frac{\omega_p}{T^2}\right) = ln\omega_0 - \frac{E_A}{kT} \qquad (3)$$

Activation energy $(E_A)$ of a trap can be obtained from Arrhenius plot by using equation (3) at different temperature $(T)$. Upon plotting $\ln\left(\frac{\omega_p}{T^2}\right) \, vs. \, \frac{1}{T}$, slope of the straight line provides $E_A$.

## 3.2    Experimental Details

*Materials*

Tin powder (99.8%, Sigma Aldrich), iodine (99.8%, Thermo Scientific), formamidinium iodide (FAI, Greatcell solar), ethane-1,2-diamine (EDA, 99%, Alfa Aesar), poly(3,4-ethylenedioxythiophene) polystyrene sulfonate (PEDOT:PSS, Clevios PVP.Al 4083 Heraeus), indene-C60 bisadduct (ICBA, Nano-C), bathocuproine (BCP, 99.0%, TCI), silver (99.99%, Kurt J. Lesker), anhydrous N,N-dimethylformamide (DMF, 99.98%, DriSolv), anhydrous dimethyl sulfoxide (DMSO, 99.9%, Sigma-Aldrich), anhydrous toluene (99.8%, Alfa Aesar), anhydrous chlorobenzene (CB, 99.8%, Acros Organics), indium tin oxide (ITO) coated glass (12 $\Omega/\square$).

*FASnI₃ solar device fabrication*

ITO patterned glass was cleaned through sequential sonication with a sodium dodecylsulfate solution, deionized water, acetone, and 2-propanol for 20 minutes each, followed by 20 min UV-ozone cleaning. Before deposition, PEDOT:PSS solution was filtered through a 0.45 μm Nylon filter, followed by spin coating at 5000 rpm for 30 s, and then annealed at 140 °C for 10 min in air. After annealing, PEDOT:PSS-coated ITO substrates were immediately transferred to the $N_2$-filled glovebox with oxygen and moisture levels of <0.1 ppm. Film processing inside the glovebox was carried out under continuous $N_2$ purging to remove solvent vapors. The $FASnI_3$ precursor solution ($FAI:SnI_2$ mixed in a mole ratio of 1:1) was prepared in a mixed DMF:DMSO solvent (5:1 volume ratio) and spun-cast at 8000 rpm with 0 s ramp time for 60 s while 120 μL of CB was dropped after 12 s of spinning. The resulting perovskite film was annealed at 80 °C for 10 min. After cooling the substrates, 100 μL of EDA (0.1 mM in toluene) was dynamically spun-cast on $FASnI_3$ films at 5000 rpm for 30 sec, followed by annealing at 80 °C for 3 min. Then, 40 μL of ICBA (20 mg/mL in CB) was spun-cast at 1200 rpm for 30 s, followed by annealing at 100 °C for 10 min. The substrates were then transferred to a thermal evaporator chamber without being exposed to air. Finally, 5 nm BCP (0.25 Å/s) and 100 nm Ag (10 nm at 0.5 Å/s and 90 nm at 2.0 Å/s) were thermally evaporated under a base pressure of $< 2 \times 10^{-6}$ mbar using an Angstrom Engineering deposition system.

## 3.3    Instrumentation

Figure 3.2 shows the TAS measurement set-up. TAS measurements were carried out using a Zurich Instruments MFLI lock-in amplifier. The sample is placed inside a liquid nitrogen cooled cryo-station (Janis ST100) equipped with a Lakeshore 336 temperature controller and connected with a 2-probe wires to the MFLI analyzer. TAS was performed in the temperature range of 160 to 300 K with a step size of 10 K. All temperatures were stabilized within ±1 K for 10 min before measurement. All measurements were recorded under dark at 0 V DC bias and 10 mV AC voltage with AC frequency ranging from 10 Hz to 1 MHz. Raw data from TAS measurement was analyzed by using Python programming.
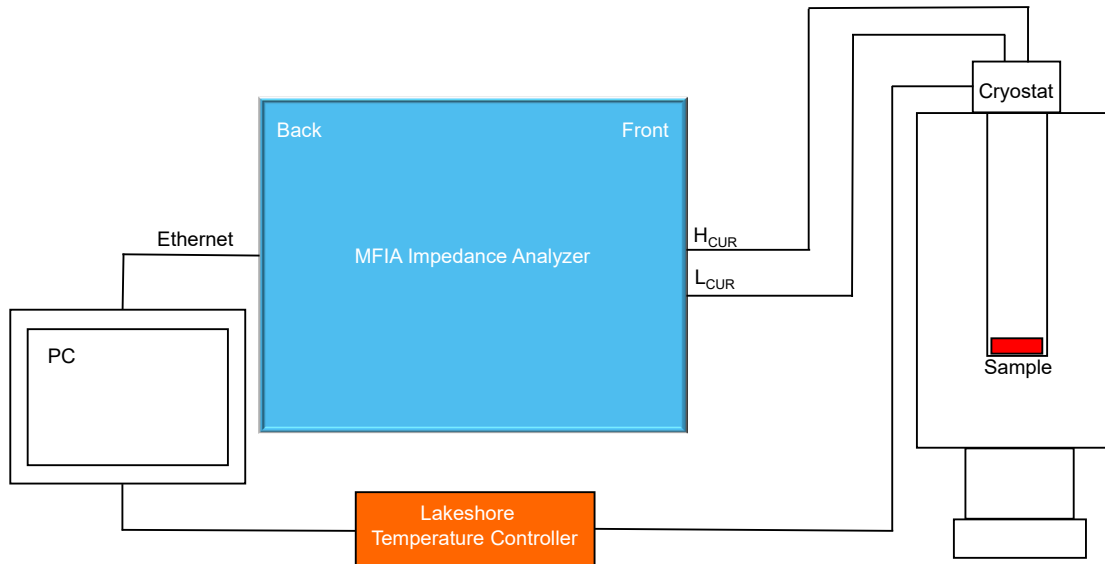


Figure 3.2 Schematic diagram of TAS measurement set-up.

## 3.4    Results and Discussion

TAS measurement is carried out in a FASnI$_3$ perovskite-based solar cell with the device structure of ITO/PEDOT:PSS/FASnI$_3$/ICBA/BCP/Ag. Figure 3.3 shows the capacitance-frequency data measure at varying temperatures from 160 to 300 K. By taking the capacitance derivative with respect to the applied frequency (Figure 3.4), characteristic peak frequency corresponding to the ion migration rates can be determined. From Figure 3.4, it is seen that there are two responses: a lower frequency response of $<10^3$ Hz, and a higher frequency response of $>10^3$ Hz. These responses can be assigned to two distinct ionic defects species.
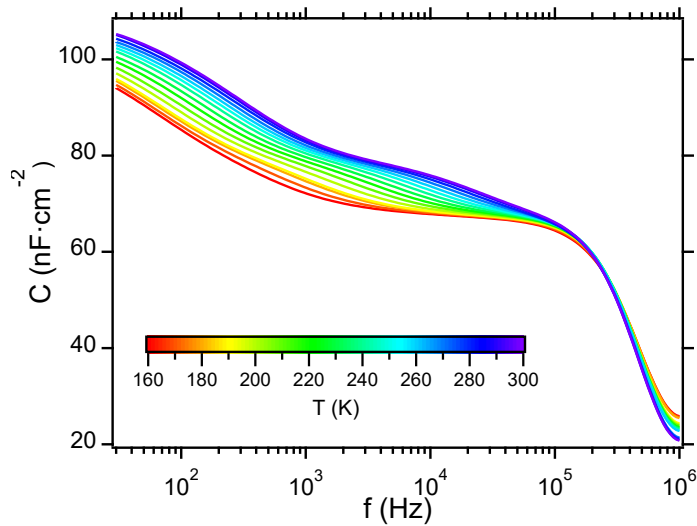


Figure 3.3 Capacitance-frequency (C-f) plot of FASnI$_3$ solar cell.
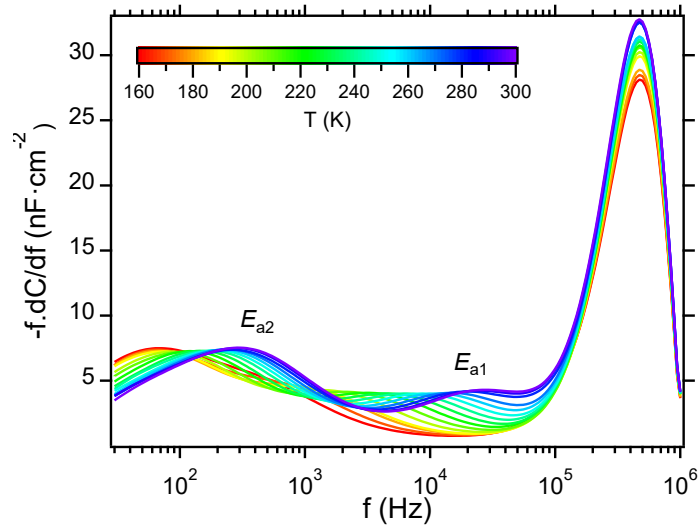
Figure 3.4 Plot of the derivative of capacitance w.r.t. frequency.

The activation energies of these two ionic defects species can be determined from Arrhenius plot (Figure 3.5). The slope of the straight line gives the activation energy ($E_a$). The activation energy of defect species at higher frequency is determined to be 1.05 eV, and the activation energy of defect species at lower frequency is found to be 0.24 eV.
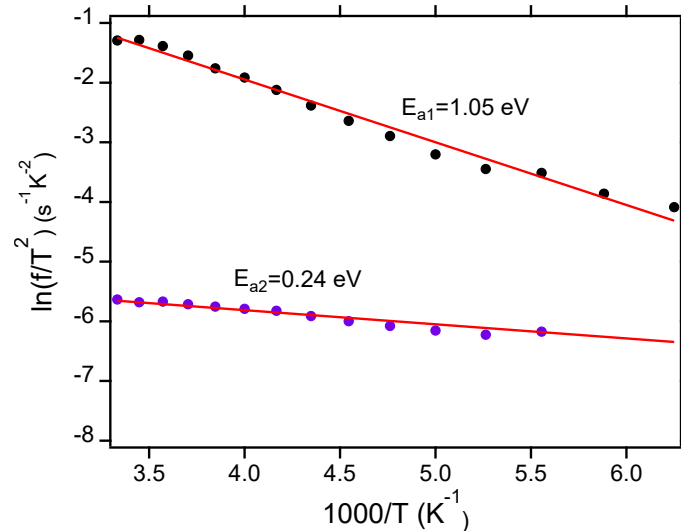


Figure 3.5 Activation energy ($E_a$) of ion migration determined from Arrhenius plot.

CHAPTER 4. HOW ADDITIVES FOR TIN HALIDE PEROVSKITES INFLUENCE THE $Sn^{4+}$ CONCENTRATION

*"Adapted with permission from Joy, S.; Atapattu, H. R.; Sorensen, S.; Pruett, H.; Olivelli, A. B.; Huckaba, A. J.; Miller, A.-F.; Graham, K. R. How Additives for Tin Halide Perovskites Influence the $Sn^{4+}$ Concentration. J. Mater. Chem. A 2022, 10, 13278–13285. Copyright (2024) Royal Society of Chemistry."*

## 4.1 Introduction

Organic metal halide perovskite (HP) based solar cells (PSCs) are widely considered as the most promising materials for high efficiency and low-cost photovoltaics (PVs), with the power conversion efficiency (PCE) of Pb-based PSCs increasing from 3.8 to 25.2% within just over a decade of intensive research efforts.[71, 72] Nevertheless, these Pb-based PSCs face several impediments to widespread commercialization, one of which is the toxicity of Pb. Desire for less-toxic PSCs has motivated intense efforts to identify Pb-free HPs for PSCs, with Sn-HPs currently being the front-runners.[73-76] Tin has a similar ionic radius (118 pm and 119 pm for $Sn^{2+}$ and $Pb^{2+}$, respectively),[77] relatively high charge-carrier mobilities,[47, 78] and a near-ideal bandgap (~1.3 eV) for reaching high PCEs.[76, 79] However, the highest certified PCE for Sn-based PSCs to date is 14.6%,[73] which is much lower than the Pb analogues. Current understanding is that the biggest impediment to high Sn-PSC performance is the oxidation of $Sn^{2+}$ to $Sn^{4+}$,[50, 74, 76] which results in deformation of the perovskite structure, defect state introduction, and rapid degradation of device performance. Thus, a major challenge for Sn-PSC development is to minimize $Sn^{4+}$ content.

Oxidation of Sn-HPs can lead to $SnI_4$ formation and eventually $I_2$ as degradation products, which perpetuates an oxidative degradation cycle that continuously deteriorates the material and device.[80] Furthermore, $SnI_4$ is present as an impurity in the $SnI_2$ precursors used to form Sn-HPs.[81] Eliminating or minimizing $Sn^{4+}$ is critical and central to all reports of relatively high-performing Sn-PSCs. Strategies to eliminate $Sn^{4+}$ include purifying $SnI_2$ or synthesizing high purity $SnI_2$ to minimize $SnI_4$ content in the precursor,[73, 81] using reducing agents to reduce $Sn^{4+}$ impurities to $Sn^{2+}$,[82] using antioxidants to prevent the formation of $Sn^{4+}$,[83, 84] and adding bulky A-site cations to stabilize the resulting films.[85, 86] A combination of these strategies is often used to fabricate high-performing Sn-PSCs.[49, 73]

Various additives have been explored to limit the amount of $Sn^{4+}$ present in HPs, with the proposed mechanism based on either $Sn^{4+}$ to $Sn^{2+}$ reduction or retarding the oxidation of $Sn^{2+}$.[82-84, 87, 88] These additives include $SnF_2$ and $SnCl_2$,[89-91] hydrazine and hydrazine containing compounds,[82, 88, 92-96] metallic tin,[97] and organic acids.[83, 84, 87] Although these additives are highly important, the mechanisms of action often remain unclear. For example, the mechanistic understanding for even the most common additive for Sn-HPs, $SnF_2$, continues to evolve.[91, 98, 99] Previously, $SnF_2$ was often regarded as a reducing additive; however, a detailed investigation by Pascual *et. al.*[99] showed that $SnF_2$ does not reduce $Sn^{4+}$ but instead undergoes a ligand exchange with $SnI_4$ to form $SnI_2$ and $SnF_4$. Here, the authors attribute the improved PSC performance with $SnF_2$ addition to the exclusion of $Sn^{4+}$ from the $FASnI_3$ crystalline grains.

In an early investigation, Song *et. al.*[88] reported that hydrazine ($N_2H_4$) vapor creates a reducing environment to suppress the formation of $Sn^{4+}$ during tin perovskite deposition. Following this report, several groups used hydrazinium iodide and hydrazine

dihydrochloride to reduce the amount of $Sn^{4+}$ and further improve the PCE and stability of Sn PSCs.[92-95] These reports suggest that hydrazine and its HI and HCl salts could reduce $Sn^{4+}$; however, no direct proof was offered to show that $Sn^{4+}$ reduction occurs. Importantly, the reduction and oxidation potentials of both the Sn species (e.g., $SnI_2$ and $SnI_4$) and the hydrazine derivatives may depend on the solvent, solution pH, and reactants present.[87, 100] Consequently, standard redox potentials reported in aqueous solutions may lead to incorrect predictions regarding redox activity in anhydrous organic solvents.

Metallic Sn, if appropriately removed from the precursor solution prior to HP film formation, can serve as an effective reducing agent for $Sn^{4+}$ to yield improved PSCs.[97, 101] Here, metallic Sn undergoes a comproportionation reaction with $Sn^{4+}$ to form $Sn^{2+}$.[97] Various acids have also been investigated as reducing agents and antioxidants, including hypophosphorous acid,[102] formic acid,[103] hydroquinonesulfonic acid potassium salt,[83] ascorbic acid,[104] and caffeic acid.[84] These examples of organic acids appear to involve the additive acting as an antioxidant rather than a reducing agent. However, whether the additive acts as an antioxidant or reducing agent is ambiguous in many reports.

Despite the significant amount of investigation into decreasing the amount of $Sn^{4+}$ in films, there is a dearth of mechanistic understanding on how different additives function and what aspects are most important. Additives may decrease the $Sn^{4+}$ concentration via three primary mechanisms, which include acting as reducing agents to directly convert $Sn^{4+}$ to $Sn^{2+}$, preventing $Sn^{2+}$ oxidation, or reacting with $Sn^{4+}$ to make it more benign, as observed for $SnF_2$ addition. In the case of antioxidants, these may react with $O_2$ to prevent $O_2$ from oxidizing the Sn-HP or they may coordinate $Sn^{2+}$ at the film surface or at grain boundaries to make the Sn-HP less susceptible to oxidation.[83, 87, 105] Occasionally,

antioxidant and reducing agent are used interchangeably in the literature, yet antioxidants are often incapable of acting as reducing agents for the species of interest. For instance, an antioxidant may react with oxidizing agents to prevent them from oxidizing the compound of interest or coordinate the compound of interest to reduce its susceptibility to oxidation.

The work presented herein seeks to improve our mechanistic understanding of how various additives diminish the amount of $Sn^{4+}$ in thin films. Included in this investigation are additives that may reduce $Sn^{4+}$, coordinate $Sn^{2+}$ in solution without reducing $Sn^{4+}$, act as antioxidants, or facilitate a halide exchange with $SnI_4$. First, we use electrochemistry to probe redox activity of the HP precursors in the typically used DMF:DMSO processing solution, including $SnI_2$ and $SnI_4$, as well as the redox potentials of a host of additives. This electrochemistry data provides a first assessment of the thermodynamic favorability of $SnI_4$ reduction. Using a combination of CV, $^1H$ and $^{119}Sn$ NMR, x-ray photoemission spectroscopy (XPS), and ultraviolet photoemission spectroscopy (UPS), we determine the impact of reducing and antioxidant additives on the concentration of $Sn^{4+}$ in solution and in thin films.

## 4.2    Experimental Details

*Materials*

Tin (II) iodide ($SnI_2$, 99.99% metals basis, Alfa Aesar), tin (II) fluoride ($SnF_2$, 99.99%, Acros Organics), tin (IV) iodide ($SnI_4$, 99.99%, Alfa Aesar), tin (II) chloride ($SnCl_2$, 98%, Fluka), tin (IV) chloride ($SnCl_4$, 99.99% trace metals basis, Beantown chemical) formamidinium iodide (FAI, Greatcell solar), methylammonium chloride (MACl, Greatcell solar),  silver nitrate ($AgNO_3$, 99.9% metals basis, Alfa Aesar),

tetrabutylammonium hexafluorophosphate (TBAPF$_6$, TCI), anhydrous N,N-dimethylformamide (DMF, 99.98%, DriSolv®), anhydrous dimethyl sulfoxide (DMSO, 99.9%, Sigma-Aldrich), anhydrous chlorobenzene (CB, 99.8%, Acros Organics), anhydrous dichloromethane (DCM, 99.8%, Acros Organics), indium tin oxide (ITO) glass (12 Ω/□), 1,2-dihydroxybenzene (Cat, TCI), 1,4-dihydroxybenzene (HQ, TCI), pyrogallol (PG, TCI), dopamine hydrochloride (DHCl, TCI), 3,5-di-tert-butylcatechol (DTBC, Thermoscientific), benzylhydrazine monohydrochloride (BHzHCl, TCI), benzoic acid (BA, Matrix Scientific), 3,4-dihydroxybenzoic acid (DHBA, 97%, Alfa Aesar), dihydrocaffeic acid (DHCA, 98%, Alfa Aesar), caffeic acid (CA, TCI), 4-fluorobenzohydrazide (4-FBH, 97%, Alfa Aesar), hydroquinonesulfonic acid potassium salt (KHQSA, Aldrich), hydrazine dihydrochloride (HzHCl, Aldrich), 1,4-dihydroxynapthalene (DHNT, TCI), 1,4-naphthaquinone (NQ, TCI), 2,5-dihydroxy-1,4-benzoquinone (DHBQ, 98%, Alfa Aesar), 1,8-dihydroxyanthraquinone (1,8-DHAQ, Acros Organics), 2,6-dihydroxyanthraquinone (2,6-DHAQ, TCI). All chemicals were used as received without further purification. All solvents were degassed before use.

*Perovskite Film Processing*

Non-patterned ITO glass was cleaned through sequential sonication with a sodium dodecylsulfate solution, distilled water, acetone, and 2-propanol for 15 minutes each, followed by 15 min UV-ozone cleaning. Immediately following UV-ozone cleaning the substrates were taken into a glovebox. To prepare 1.0 mL of 1.0 M FASnI$_3$ solution, SnI$_2$ (0.3725 g, 1.0 mmol), FAI (0.1719 g, 1.0 mmol), and 10% SnF$_2$ (0.0157 g, 0.1 mmol) were measured in a vial, and then 800 µL of DMF and 200 µL of DMSO (4:1) were added to it.

The mixture was heated at 70 ºC for 30 min to dissolve the solids. Before deposition, the mixture was filtered through a 0.2 μm PTFE filter and cooled down to room temperature. Then the precursor solution was spun-cast at 6000 rpm for 30 s while 120 μL of CB anti-solvent was added after 12 s of spinning. The resulting film was then annealed at 100 ºC for 10 min. For FASnI$_3$ films with additives, 2.5 mol% of additives were added to the perovskite precursor solution before coating the thin film. Film processing was carried out under continuous purging of the N$_2$-filled glovebox to maintain O$_2$ and H$_2$O levels of less than 0.1 ppm.

*Cyclic Voltammetry*

Glassy carbon, Pt wire, and a non-aqueous Ag/AgNO$_3$ (Ag/Ag+, 1.0 M in DMF:DMSO, 4:1) were used as working electrode, counter electrode and reference electrode, respectively. TBAPF$_6$ was dried at 100 ºC under vacuum overnight prior to use. TBAPF$_6$ was used as the supporting electrolyte at 0.1 M in DMF:DMSO. All analyte concentrations were kept at 0.01 M. A 0.02 V/sec scan rate was used for all CVs. Solution preparation and CV measurements were carried out in the N$_2$-filled glovebox (O$_2$ and H$_2$O level were <0.1 ppm). Working electrode was polished with alumina and DI water slurry before each measurement. Anhydrous and degassed solvents were used to avoid H$_2$O and O$_2$ presence during CV measurements. For the CV of FASnI$_3$ film, perovskite film was made on non-patterned ITO glass according to the description before. Anhydrous and degassed DCM solvent was used for this measurement. The redox potential (E$_{1/2}$) of analytes was calculated by taking the average of cathodic (Ep,c) and anodic (Ep,a) peak potential *i.e.*, E$_{1/2}$ = (Ep,c + Ep,a)/2.

The NMR solutions (0.5 M of $SnI_4$, $SnI_2$, $SnCl_2$, $SnCl_4$, MACl, DHCl, BHzHCl, DHCA, HzHCl, 4-FBH, BA, KHQSA, DHNT, HQ, NQ; or 0.1 M of 1,8-DHAQ and 2,6-DHAQ) were prepared in anhydrous and degassed DMSO-$d_6$ solvent. Additives and $SnI_4$ were mixed in a 1:1 stoichiometry. Tin (II) chloride solutions were filtered with 0.2 μm PTFE filters to remove precipitates.

$^1H$ and $^{119}Sn$ NMR studies were carried out using a Bruker Advance NEO (400MHz) spectrometer equipped with a 5mm broadband SmartProbe. All experiments were run at 298K. Chemical shifts in the $^{119}Sn$ NMR studies were referenced to an external standard $Sn(CH_3)_4$ ($\delta = 0.00$ ppm) and the $^1H$ NMR chemical shifts were referenced to the residual solvent protons. $^{119}Sn$ was detected via the broadband channel using a 3.33 μs 30° excitation pulse, and inverse gated $^1H$ decoupling during the 0.655 s signal acquisition, with 4 s relaxation delays between transients. A spectral width of 500k Hz encompassing -3000 ppm to 1000 ppm was collected.  Spectra were processed with 120 Hz line broadening and represent averaging of 512 to 6144 scans. $^1H$ spectra were obtained using a 30 ° excitation pulse, digitization over 3.99 seconds and 4 s relaxation delay between transients.  Spectra were processed with 0.3 Hz line broadening and represent averages of 512 and 1024 scans.

*Absorbance*

UV-vis absorbance spectra were collected using an Ocean Optics QE Pro high-performance spectrometer with 700 ms integration time and 5 μm slit width. The final

concentration of analytes was kept at 1.0 mM and the solutions were prepared by mixing $SnI_4$ and additives in a 1:1 mole ratio in DMF:DMSO (4:1).

*Photoluminescence*

PL spectra of thin films were collected using a 550 nm laser (Thorlabs, CPS532) and an Ocean Optics QE pro high-performance spectrometer with 1100 ms integration time and 200 μm slit width.

*X-Ray Diffraction*

Thin films for XRD measurements were prepared on non-pattered ITO glass as mentioned before. The XRD patterns were recorded with a Bruker-AXS D8 DISCOVER diffractometer with Cu Kα radiation ($\lambda = 1.5418$ Å) operating at 40 kV and 40 mA.

*X-ray Photoelectron (XPS) and Ultraviolet Photoelectron (UPS) Spectroscopy*

All films were prepared on non-pattered ITO glass as mentioned before. XPS and UPS measurements were carried out in a PHI 5600 UHV system with a base pressure < 4 x $10^{-10}$. XPS were carried out using an Al Kα source (1486.6 eV) with a pass energy of 23.5 eV. UPS were obtained with 10.2 eV photons for excitation (Excitech H Lyman-α lamp). The pass energy used for UPS was 5.85 eV and all samples were biased at -5 V. All the samples were measured within 24 h after sample preparation and the samples were kept entirely under nitrogen (<0.1 ppm $O_2$ and $H_2O$). Our UHV system is directly connected to one of our gloveboxes, thereby completely eliminating air exposure.

## 4.3    Results and Discussion

Cyclic voltammetry (CV) provides a direct way to measure reduction and oxidation of Sn-HP precursors in solution. Herein, we focus our discussion on anodic ($E_{p,a}$) and cathodic ($E_{p,c}$) peak potentials, as the reduction potentials for some species cannot be determined due to the irreversibility of the electrochemical reaction. To ensure that the anodic and cathodic potentials reported are directly relevant to Sn-HPs, we measured CVs in both pure DMF and the commonly used DMF:DMSO (4:1) solvent system. Although DMSO can act as an oxidizing agent for $SnI_2$,[106, 107] the CV spectra for the formamidinium tin iodide ($FASnI_3$) precursors in DMF and DMF:DMSO solutions are nearly identical, as shown in Figure 4.1 and 4.7. Tin (II) iodide shows a $E_{p,c}$ of -1.15 V (*vs.* Ag/Ag$^+$), whereas $E_{p,c}$ for $SnI_4$ occurs at -0.72 V. Films of $FASnI_3$ also show nearly the same onset for the cathodic wave of $Sn^{2+}$ as is observed for $SnI_2$ in solution, with an $E_{p,c}$ of -1.20 V (*vs.* Ag/Ag$^+$) (Figure 4.8). The $E_{1/2}$ for $SnI_2 + 2e^- \leftrightarrow Sn^0 + 2I^-$ is -1.02 V; however, with an irreversible reduction the $E_{1/2}$ for $SnI_4 + 2e^- \leftrightarrow SnI_2 + 2I^-$ cannot be determined. The commonly used additive $SnF_2$ shows a more negative $E_{1/2}$ than $SnI_2$ at -1.13 V. Given the reduction behavior of $SnI_2$ and $SnI_4$, ideal reducing agents for reducing $SnI_4$ to $SnI_2$ should have redox potentials in the range of *ca.* -0.75 to -1.0 V vs. Ag/Ag$^+$ when measured in DMF:DMSO. In this range $SnI_4$ reduction to $SnI_2$ is thermodynamically favorable, while further reduction to metallic Sn is not favorable. That is, the upper limit of this recommend range (*ca.* -0.75 V) is more negative than the $E_{p,c}$ for $SnI_4$ (-0.72 V) and thus reduction of $SnI_4$ to $SnI_2$ is favorable, while the lower limit (*ca.* -1.0 V) avoids reducing $SnI_2$ to metallic Sn, as $SnI_2$ shows an onset of reduction at *ca* -1.04.
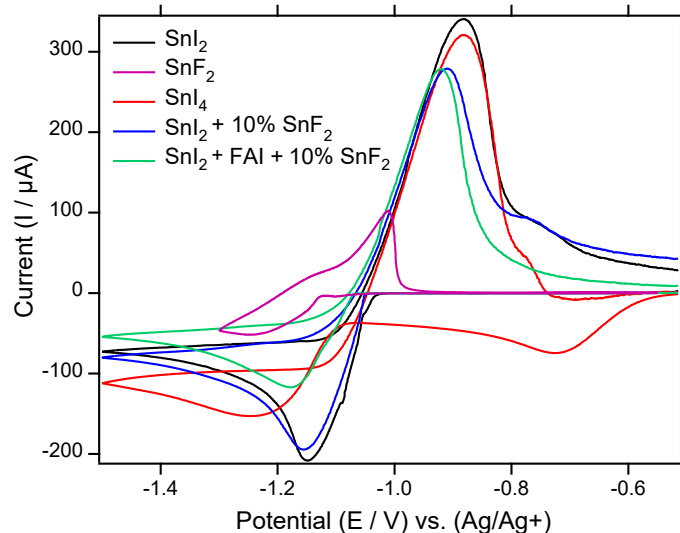
Figure 4.1 CV of SnI$_2$, SnF$_2$, SnI$_4$, SnI$_2$ + 10% SnF$_2$, and SnI$_2$ + FAI + 10% SnF$_2$ in DMF:DMSO (4:1) with 0.1 M TBAPF$_6$ as the supporting electrolyte.

With the oxidation and reduction behavior of SnI$_2$ and SnI$_4$ in DMSO:DMF determined, we now turn to investigating the influence of the additives. To investigate the mechanism through which several reported additives for Sn HPs function and to identify new additives, the molecules and complexes shown in Figure 4.2a were initially investigated with CV, as shown in Figure 4.2b and c. The additives investigated include quinones and hydroxyquinones, catechols and structurally related derivatives, hydrazine containing derivatives, and hydrochloride containing species. Specifically, the quinones and hydroxyquinones are selected for their large variation in redox potentials, the catechols for their anticipated abilities to coordinate Sn halides, and the hydrazine derivatives for their low oxidation potentials that make them amenable for use as reducing agents.
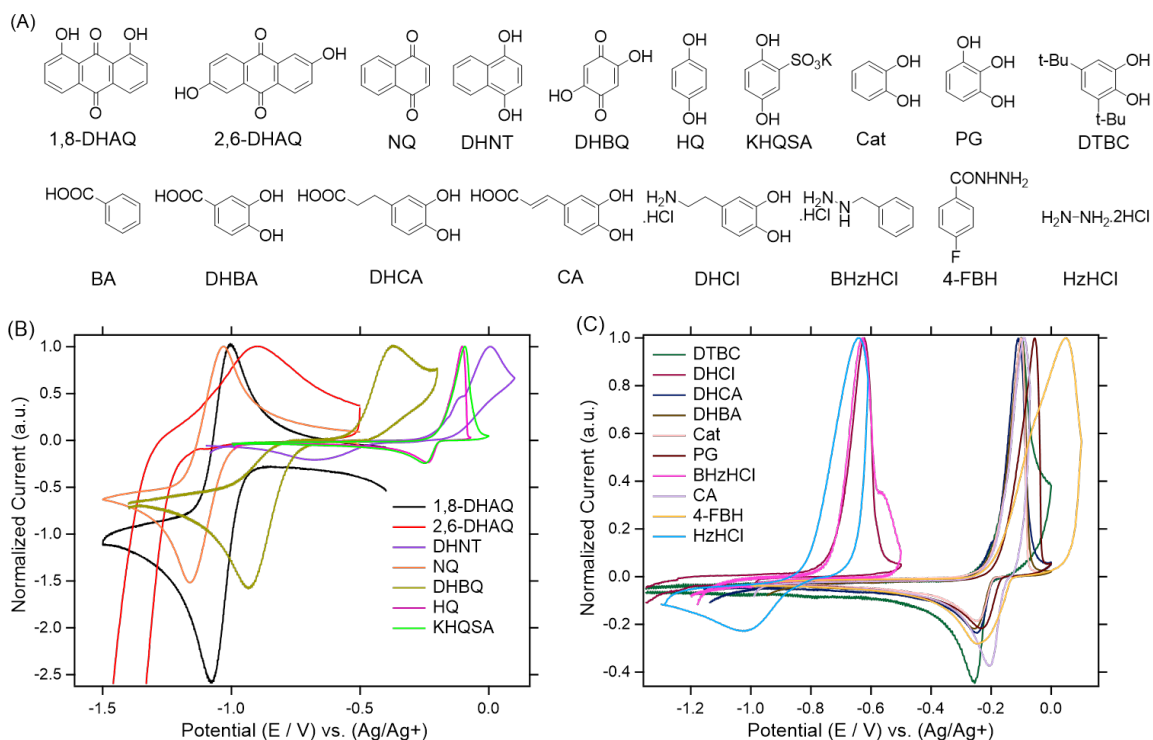
Figure 4.2 Chemical structures (A) and CV of additives (B and C) in DMF:DMSO (4:1) with 0.1 M TBAPF$_6$ as the supporting electrolyte.

The CV data show three clusters of anodic peaks, with the dihydroxyanthroquinone derivatives (1,8-DHAQ and 2,6-DHAQ) and naphthoquinone (NQ) showing E$_{p,a}$ near -1.0 V; the hydrochloride (HCl) salts including dopamine HCl (DHCl), benzylhydrazine HCl (BzHCl), and hydrazine HCl (HzHCl) showing E$_{p,a}$ near -0.6 V; and the catechol and hydroquinone derivatives displaying E$_{p,a}$ close to -0.1 V. One additive, 2,5-dihydroxy-1,4-benzoquinone (DHBQ), has E$_{p,a}$ outside of these regions at -0.37 V. Based on these anodic peak positions and E$_{1/2}$ values, HzHCl, BHzHCl, and DHCl are near the range where SnI$_4$ to SnI$_2$ reduction becomes favorable, while 1,8-DHAQ, 2,6-DHAQ, and NQ are in a range where SnI$_4$ to SnI$_2$ reduction is favorable with the possibility of SnI$_2$ to metallic Sn reduction occuring. However, to act as reducing agents the additives must originally be in their reduced form, which is not the case with 1,8-DHAQ, 2,6-DHAQ, and NQ. A

commercially available reduced form of NQ, DHNT, shows an anodic peak near 0 V and an $E_{1/2}$ of -0.33 V, which is not appropriate for reducing $SnI_4$. The fact that the electrochemically reduced form of NQ does not show an anodic peak at the same potential as DHNT indicates that NQ does not undergo a two-proton coupled electron transfer upon reduction in the DMF:DMSO solvent system, as it does in aqueous solution.[108] Rather, the electrochemically reduced form of NQ is a singly charged anion.[108]

Table 4.1 Anodic and cathodic peak potentials of $SnI_2$, $SnI_4$, and additives. $E_{p,a}$, $E_{p,c}$ and $E_{1/2}$ values are reported vs. Ag/Ag+ (1 M) reference electrode.

| Compound | $E_{p,a}$ (V) | $E_{p,c}$ (V) | $E_{1/2}$ (V) |
|---|---|---|---|
| $SnI_2$ ($SnI_2 \leftrightarrow Sn^0$) | -0.88 | -1.15 | -1.02 |
| $SnI_4$ ($SnI_4 \leftrightarrow SnI_2$) | NA* | -0.72 | NA |
| $SnF_2$ ($SnF_2 \leftrightarrow Sn^0$) | -1.01 | -1.25 | -1.13 |
| Cat | -0.10 | -0.25 | -0.18 |
| PG | -0.05 | -0.23 | -0.14 |
| DTBC | -0.09 | -0.26 | -0.18 |
| DHBA | -0.10 | -0.25 | -0.18 |
| CA | -0.09 | -0.21 | -0.15 |
| DHCA | -0.10 | -0.24 | -0.17 |
| DHCl | -0.65 | NA | NA |
| BHzHCl | -0.63 | NA | NA |
| HQ | -0.10 | -0.24 | -0.17 |
| KHQSA | -0.09 | -0.25 | -0.17 |
| 4-FBH | 0.05 | -0.25 | -0.10 |
| HzHCl | -0.64 | -1.03 | -0.84 |
| DHBQ | -0.37 | -0.93 | -0.65** |
| NQ | -1.03 | -1.16 | -1.09 |
| DHNT | 0.008 | -0.67 | -0.33** |
| 1,8-DHAQ | -0.99 | -1.12 | -1.06 |
| 2,6-DHAQ | -0.93 | -1.45 | -1.19** |

*NA indicates that peak was not observed. If either the cathodic or anodic peak is missing, then $E_{1/2}$ cannot be calculated.**Quasireversible process, $E_{1/2}$ calculated from the anodic and cathodic peak potential.

Several additives that were shown to decrease the amount of $Sn^{4+}$ present in Sn-HPs, including caffeic acid (CA),[84] potassium hydroquinonesulfonate (KHQSA),[83] and 4-fluorobenzohydrazide (4-FBH),[105] show $E_{p,a}$ and $E_{1/2}$ values that are far too positive to act as reducing agents for $SnI_4$. The fact that all three of these additives have been shown to diminish the concentration of $Sn^{4+}$ in Sn-HPs indicates that something other than $SnI_4$ reduction is occurring, likely involving coordination to $Sn^{2+}$ to prevent oxidation. Another additive that was demonstrated to decrease the $Sn^{4+}$ concentration, HzHCl, has an $E_{p,a}$ of -0.64 V and an $E_{1/2}$ in the ideal range for $SnI_4$ reduction without over reduction to metallic Sn at -0.84 V. Additionally, BHzHCl and DHCl show similar anodic peaks of -0.63 and -0.65 V, respectively, suggesting that they may also be able to reduce $SnI_4$ to some extent. To further probe the ability of selected additives to reduce $SnI_4$ we carried out solution state $^{119}$Sn NMR measurements.
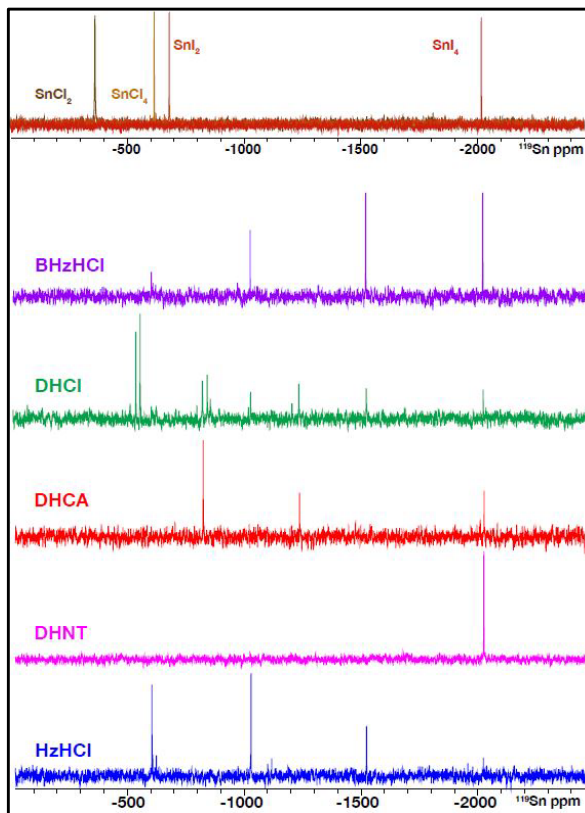
Figure 4.3 $^{119}$Sn NMR of the reference Sn compounds (SnI$_2$, SnI$_4$, SnCl$_2$, SnCl$_4$) (top) and SnI$_4$ + additive (1:1 mole ratio) in DMSO-$d_6$.

The $^{119}$Sn NMR shows clear and well separated peaks for SnI$_2$ and SnI$_4$. Here, SnI$_4$ shows a signal at a chemical shift of -2025 ppm while SnI$_2$ falls at -691 ppm. To probe for SnI$_4$ to SnI$_2$ reduction, selected additives were added to SnI$_4$ in DMSO solutions at a 1:1 concentration and $^{119}$Sn NMR spectra recorded, as shown in Figure 4.3 and 4.16. No clear evidence of SnI$_4$ reduction to SnI$_2$ is observed for any of the additives investigated; although, it cannot be excluded that some of the peaks in the -500 to -700 ppm range correspond with complexes of SnI$_2$. The three additives with $E_{p,a}$ in the -0.63 to -0.65 V range all show the presence of several other Sn peaks; however, none of these peaks align directly with SnI$_2$. Notably, all these additives (BHzHCl, DHCl, and HzHCl) contain HCl. All three display peaks at -606 ppm near that of SnCl$_4$, as well as peaks at *ca.* -1030 and -

46

1525 ppm, which we attribute to the presence of $SnI_2Cl_2$ and $SnI_3Cl$, respectively.[109, 110] These products originate from halide exchange, similar to that observed between $SnI_4$ and $SnF_2$.[99] This halide exchange does not depend on the oxidation potential of the additives, as it also occurs when methylammonium chloride is added to $SnI_4$, as shown in Figures 4.16 and 4.17. A series of $^{119}Sn$ NMR and UV-Vis absorbance spectra were recorded with varying $SnI_4$:MACl ratios to further support the NMR peak assignments and the formation of $SnI_xCl_y$ species, as shown in Figure 4.17. Here, the $^{119}Sn$ NMR shows that as the ratio of $SnI_4$:MACl decreases the peak intensities corresponding with increased y values in $SnI_xCl_y$ increase, while the UV-Vis shows a decrease in $SnI_4$ absorbance intensity and a blue shift in absorbance maxima as the amount of MACl increases. At a 1:4 ratio, where the moles of I and Cl are equal, Cl completely displaces I and results in the presence of only $SnCl_4$ in the $^{119}Sn$ NMR spectra. In accordance with the explanation for F exchange with I in $SnI_4$,[99] the Cl exchange can also be attributed to the increased stability of $SnCl_4$ relative to $SnI_4$ described by hard-soft acid-base theory. The formation of $SnI_xCl_y$ complexes is likely to have a significant influence on the resulting defect states in Sn-HPs, potentially leading to exclusion of the $Sn^{4+}$ species from the $FASnI_3$ crystalline grains or a change in the energies of the resulting defect states. Additionally, these species may evaporate from the film considering the relatively low boiling point of $SnCl_4$ of 114 °C.[111]

In addition to the formation of $SnI_xCl_y$, other products and complexes are also evident in the $^{119}Sn$ NMR. Here, DHCl shows several additional strong peaks, including at -540, -558, -825, and -845 ppm. The $^1H$ NMR of DHCl with $SnI_4$ shows a large shift in the hydroxyl protons from a doublet centered at 8.83 ppm to a broad singlet at 6.8 ppm and a reduction in the integrated intensity. This combination of $^{119}Sn$ and $^1H$ NMR strongly

supports that DHCl is forming a coordination complex with the Sn species through the hydroxyl groups, potentially with one of the hydroxyl groups becoming deprotonated. The coordination of Sn species is not unique to DHCl, as all additives investigated with hydroxyl or carboxylic acid groups show significant shifts and broadening of the hydroxyl and carboxylic acid protons upon $SnI_4$ addition (Figures 4.20-4.23). The ability of these additives to coordinate Sn species in solution is also expected to have an impact on the amount of $Sn^{4+}$ in HP films due to reduced reactivity of the coordinated Sn species. Aside from BHzHCl, DHCl, and HzHCl, the only other additive that shows a large decrease in the amount of $SnI_4$ present is DHCA. When DHCA is added to $SnI_4$ new peaks in the $^{119}Sn$ NMR spectrum appear at -825 and -1238 ppm, the carboxylic acid proton shifts up field by 2.5 ppm, and the hydroxyl group protons shift down field by 0.5 ppm. These results indicate strong coordination between the Sn complexes and DHCA.

Further investigation into solution behavior of Sn species upon addition of various additives was carried out by recording cyclic voltammograms of $SnI_2$ + FAI + $SnI_4$ solutions with and without additives, as displayed in Figure 4.14. When HzHCl, BHzHCl, DHCl, or DHCA are added to the Sn-HP precursor solutions with $SnI_4$ there is a decrease in the current arising from $SnI_4$ reduction. (Figure 4.14A, B). This decrease in current may arise from a combination of (1) the formation of $SnI_xCl_y$ species, as $SnCl_4$ shows a significantly higher reduction potential than $SnI_4$ (Figure 4.14C), (2) strong coordination between $SnI_4$ and the additive that shifts the reduction potential of $SnI_4$, or (3) complex formation between reduced forms of Sn, such as $SnI_2$, SnICl, or $SnCl_2$. Absorbance of $SnI_4$ in solution with HzHCl, BHzHCl and DHCl additives show large (78, 48 and 55%, respectively) decreases in $SnI_4$ absorbance at 400 nm (Figure 4.15), which agrees with the

decreased $SnI_4$ concentration observed in CV and NMR. The absorbance of $SnI_4$ at 400 nm also decreases with DHCA. Although, the decrease is only 33%, suggesting either strong coordination between $SnI_4$ and DHCA or fractional reduction of $SnI_4$ to $SnI_2$. Based on the $^{119}Sn$ NMR, if $SnI_2$ is formed upon reaction with DHCA, the $SnI_2$ is coordinated to DHCA.

We now shift to how solution behavior relates to the concentration of $Sn^{2+}$ and $Sn^{4+}$ in the $FASnI_3$ films. We initially fabricated Sn-HP films with additive concentrations of 0.5, 1, and 2.5% and recorded the UV-Vis absorbance and photoluminescence (PL) spectra, as displayed in Supporting Information Figures 4.9 and 4.10. Nearly all additives show an enhancement in the PL intensity at all additive concentrations. Furthermore, x-ray diffraction spectra (Figure 4.11) are similar for all $FASnI_3$ films with 2.5% of the additives incorporated. All additives were thus incorporated at 2.5% for the XPS and UPS measurements to increase our ability to detect their effects on the $FASnI_3$ films. Here, using XPS we probed the concentration of $Sn^{4+}$ relative to $Sn^{2+}$ for the $FASnI_3$ films with various additives, as shown in Figure 4.4 and Figure 4.12. In the control $FASnI_3$ sample with no additive the $Sn^{4+}$ content is 6.9% and $Sn^{2+}$ is 93.1%. Similar $Sn^{4+}$ concentrations between 6.1 and 7.6% are found with 1,8-DHAQ, NQ, DHBQ, HQ, and 4-FBH. As may be expected, none of these additives show reduction potentials suitable for reducing $SnI_4$. The three HCl containing additives, BHzHCl, HzHCl, and DHCl, all show a depressed concentration of $Sn^{4+}$ relative to the control, with $Sn^{4+}$ concentrations of 3.6, 4.5, and 5.1%, respectively. DHCA, which diminished the free $SnI_4$ concentration based on the $^{119}Sn$ NMR also shows a significant decrease in $Sn^{4+}$ content at 4.1%.

Surprisingly, DHNT displays the lowest $Sn^{4+}$ concentration of 3.3% relative to $Sn^{2+}$. We attribute this low $Sn^{4+}$ content with DHNT to two methods of antioxidant behavior, including the reaction of DHNT with oxygen to prevent the reaction of oxygen with the perovskite and coordination to Sn species at the perovskite surface. The reaction of DHNT with oxygen is supported by ^{1}H NMR measurements (Figure 4.22), where DHNT shows a decrease in the hydroxyl proton intensity and massive broadening of the remaining proton signal following exposure to ambient atmosphere. The same behavior is also observed when $SnI_2$ is present with DHNT at a 1:1 mole ratio, only now the aromatic protons on DHNT all shift up field. We attribute this up field shift following air exposure to coordination between $SnI_2$ and the ionized DHNT derivative formed upon air exposure.
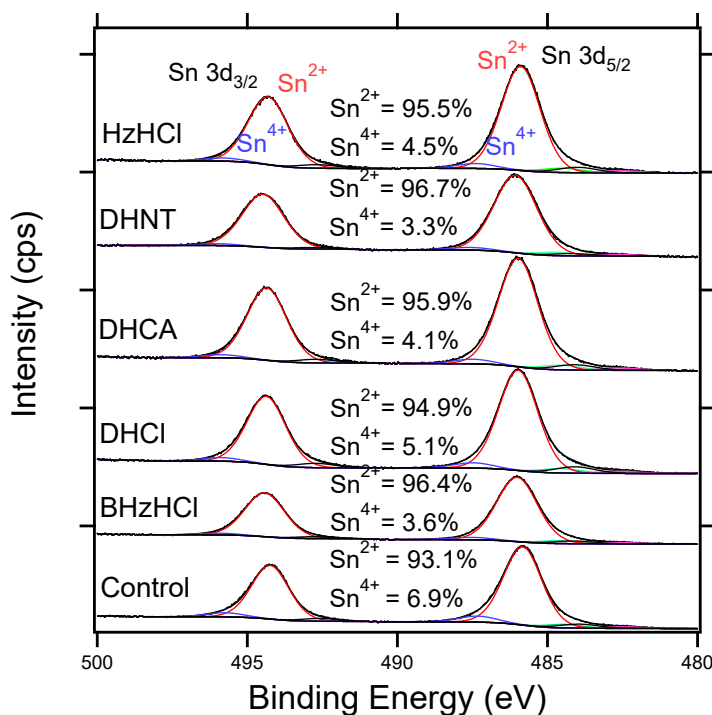


Figure 4.4 XPS spectra of the Sn 3d region for $FASnI_3$ films with fits to the $Sn^{2+}$ and $Sn^{4+}$ peaks for the films made with 2.5 mol% of varying additives.

Ultraviolet photoelectron spectroscopy can also provide insight into the concentration of $Sn^{4+}$, as the presence of $Sn^{4+}$ leads to high concentrations of holes (*p*-type charge carriers) in $FASnI_3$. Here, a more *p*-type film will, to a first approximation, be associated with a higher work function and a valence band onset that is closer to the Fermi energy ($E_F$). The $FASnI_3$ film without any additive shows a work function of 4.85 eV, which is similar to $FASnI_3$ with the additives that showed comparable $Sn^{4+}$ compositions (Figure 4.5, SI Figure 4.13 and Table 4.2). On the other hand, when the $Sn^{4+}$ composition determined by XPS decreases, the work function also generally decreases and the valence band onset shifts further from $E_F$. For example, DHNT shows the lowest work function and the lowest $Sn^{4+}$ content and BHzHCl, DHCl, and DHCA all have lower $Sn^{4+}$ content and work functions that are 0.3 to 0.4 eV lower than the control. These UPS results agree with the $Sn^{4+}$ concentrations determined by XPS and support that increased $Sn^{4+}$ content leads to more *p*-type character.
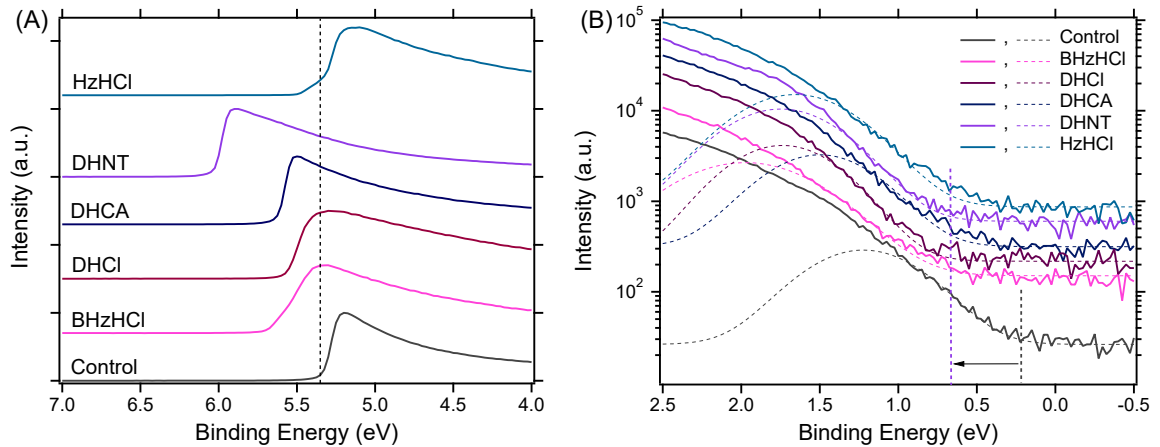


Figure 4.5 UPS spectra of $FASnI_3$ film with 2.5 mol% varying additives A) the secondary electron cut-off regions, B) the valence band onset regions.

The various pathways through which the additives can influence the defect states present in Sn halide perovskites are summarized in Figure 4.6. The ability of the additive to coordinate $SnI_2$ and Sn species at grain boundaries and surfaces of $FASnI_3$ films is one parameter that can significantly impact the amount of $SnI_2$ present. For example, both the ^{119}Sn and ^{1}H NMR support that DHCA coordinates with Sn halide species in solution and reduces the concentration of $Sn^{4+}$ in the $FASnI_3$ films. Another important consideration is the ability of the additive to reduce $SnI_4$ to $SnI_2$. Reduction of $SnI_4$ to $SnI_2$ does not appear to be a primary mode of action for most organic additives used thus far in Sn-HP, except for possibly hydrazine containing species. Identification of additives that can reduce $SnI_4$ to $SnI_2$ without over reduction to metallic Sn is a promising path forward; however, it may be important that these reducing additives be driven off during thermal annealing to prevent them from acting as charge traps in the Sn-HP films. Halide exchange with both $SnF_2$ and chloride containing salts is a clear route for reducing the debilitating impact of $Sn^{4+}$ on Sn-PSCs, and our work clarifies that halide exchange occurs with HCl salts that are being applied to improve Sn-PSCs.[95, 112, 113] Finally, the additive may act as a sacrificial antioxidant to impede the oxidation of Sn species in the solution or solid state. We propose that it will be necessary to consider multiple of these factors when designing additives, or combinations of additives, for Sn-HPs. For example, two additives with different primary functions may be necessary. In this case one additive could reduce $SnI_4$ to $SnI_2$ in solution and be driven off during HP formation, and another additive could coordinate Sn species at surfaces and grain boundaries to prevent oxidation after film formation.
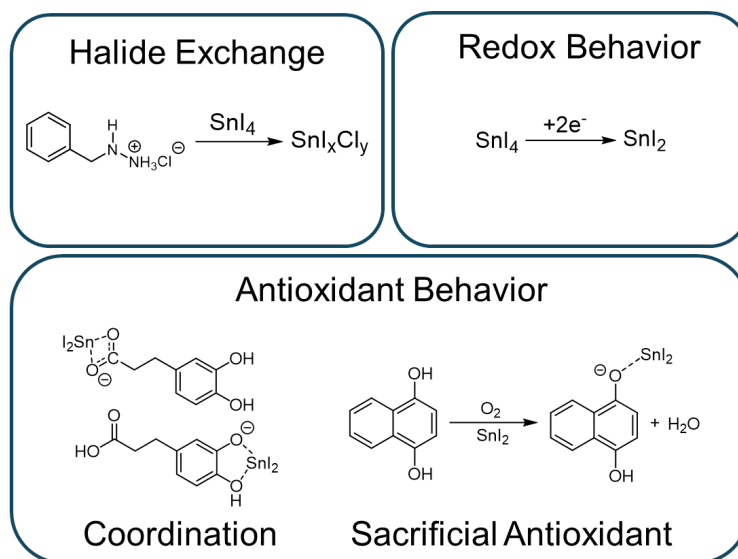
Figure 4.6 Schematic of the various mechanisms through which additives can influence the concentration of $Sn^{4+}$ species and their impact on material properties.

## 4.4    Conclusion

In summary, the work presented here identifies an ideal range for the reduction potentials of additives to remove $SnI_4$ impurities and shows that many commonly used additives do not fall within this ideal range. Identifying and applying reducing agents that can both fully reduce $SnI_4$ to $SnI_2$ and coordinate Sn at the Sn-HP surface to prevent further Sn oxidation is a promising path forward for improving Sn-based PSCs. We also show that $SnI_4$ readily undergoes halide exchange when $Cl^-$ is present in solution, potentially resulting in less harmful defect states in the Sn-HP film or evaporation of $Sn^{4+}$ species ($SnI_xCl_y$) from the film. This halide exchange may be a primary explanation for the success of several additives for Sn-HPs. Through UPS and XPS we show that the lowest $Sn^{4+}$ content is found for an additive that does not reduce $SnI_4$ or result in the formation of $SnI_xCl_y$ complexes. The ability of this additive, DHNT, to lower the concentration of $Sn^{4+}$ in $FASnI_3$ films is

53

attributed to its reactivity with oxygen as a sacrificial antioxidant. Overall, our work highlights that the reduction potential, coordination with Sn species, ability to react with oxygen, and the potential for halide exchange should all be taken into consideration when evaluating or designing additives for Sn-HPs.

## 4.5    Additional Figures and Tables
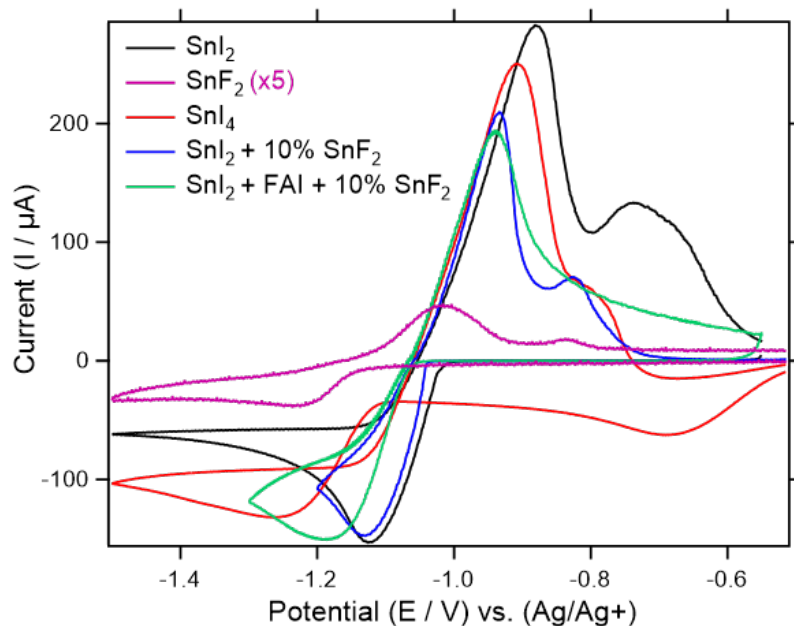


Figure 4.7 CV of $SnI_2$, $SnF_2$ (multiplied by a factor of 5), $SnI_4$, $SnI_2$ + 10% $SnF_2$, and $SnI_2$ + FAI + 10% $SnF_2$ in DMF with 0.1 M $TBAPF_6$ as the supporting electrolyte.
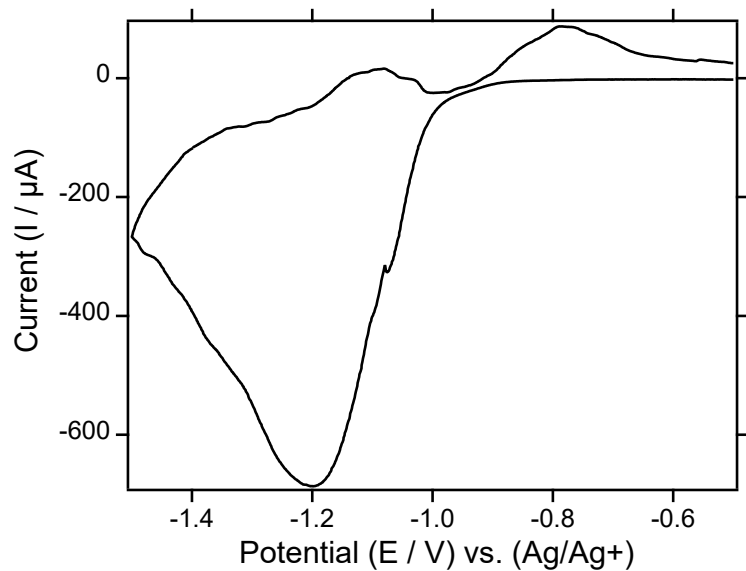
Figure 4.8 CV of FASnI$_3$ thin film in DCM with 0.1 M TBAPF$_6$ as the supporting electrolyte.
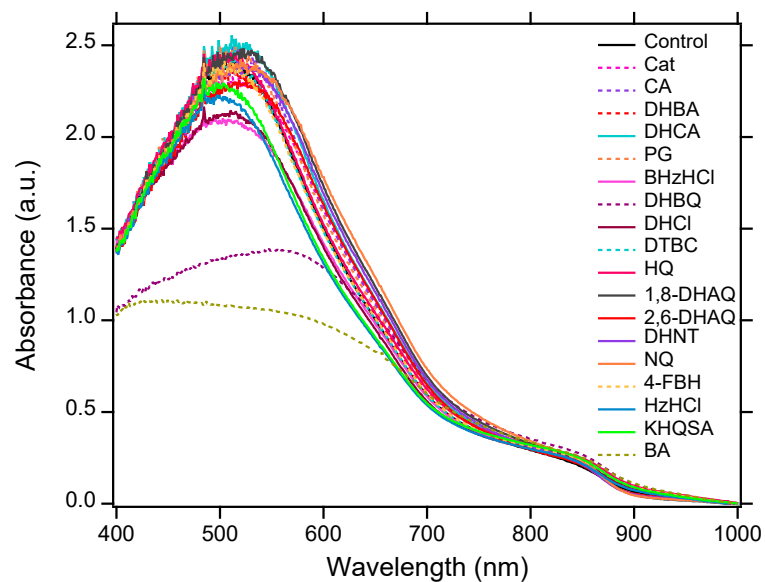


Figure 4.9 UV-vis absorbance spectra of FASnI$_3$ films with 1.0 mol% of varying additives.
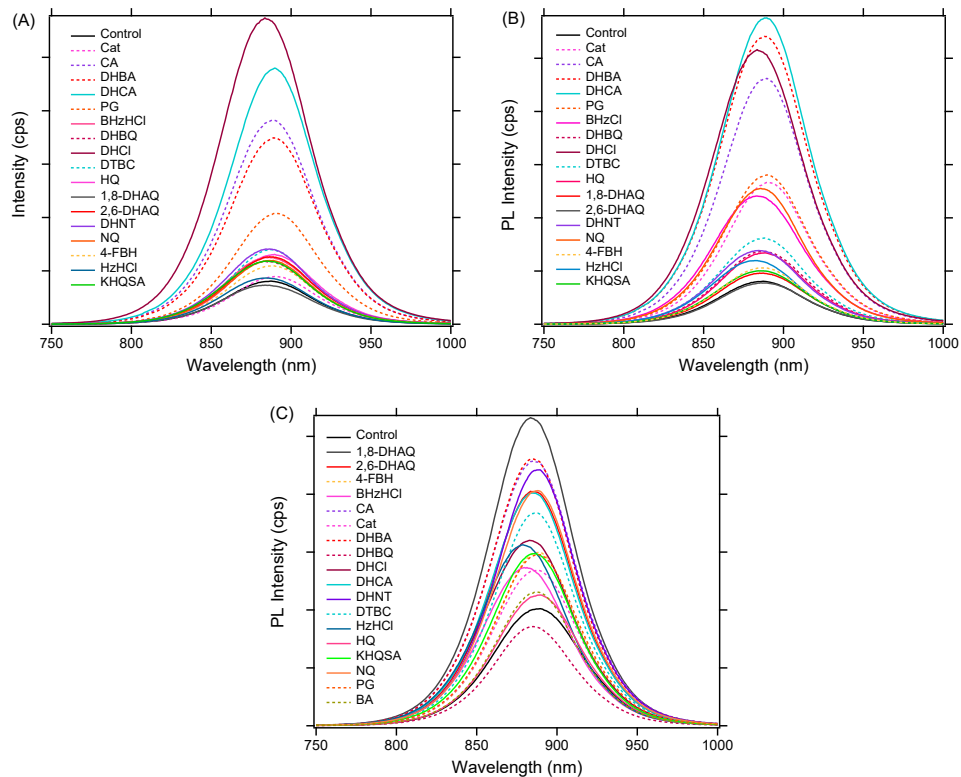
Figure 4.10 Photoluminescence intensity of FASnI₃ films with A) 0.5; B) 1.0; and C) 2.5 mol% of varying additives, respectively.
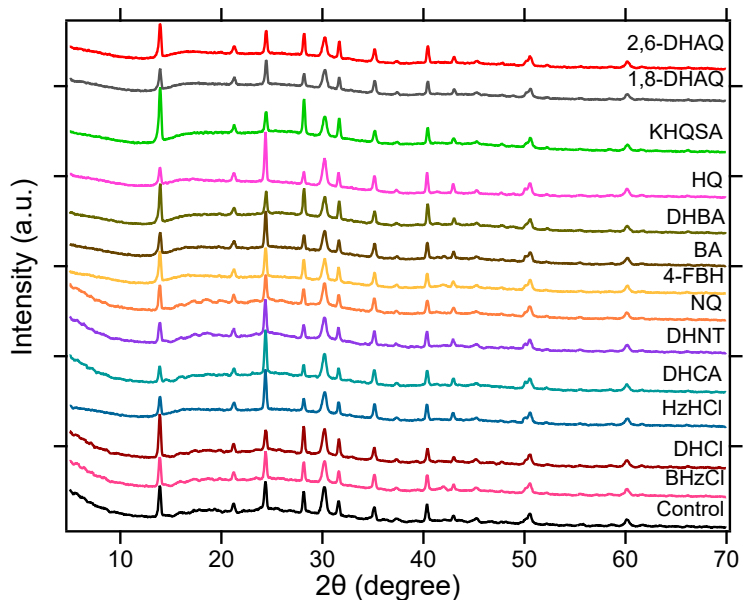


Figure 4.11 XRD patterns of FASnI₃ films with 2.5 mol% of varying additives.

Table 4.2 $Sn^{4+}$ to $Sn^{2+}$ ratio in 2.5 mol% additive treated $FASnI_3$ films.

| Additive | $Sn^{4+}:Sn^{2+}$ ratio |
|---|---|
| None (control) | 0.07 |
| BHzHCl | 0.04 |
| DHCl | 0.05 |
| DHCA | 0.04 |
| DHBA | 0.06 |
| BA | 0.06 |
| DHNT | 0.03 |
| HzHCl | 0.05 |
| 4-FBH | 0.06 |
| HQ | 0.08 |
| KHQSA | 0.03 |
| DHBQ | 0.07 |
| NQ | 0.08 |
| 2,6-DHAQ | 0.05 |
| 1,8-DHAQ | 0.07 |
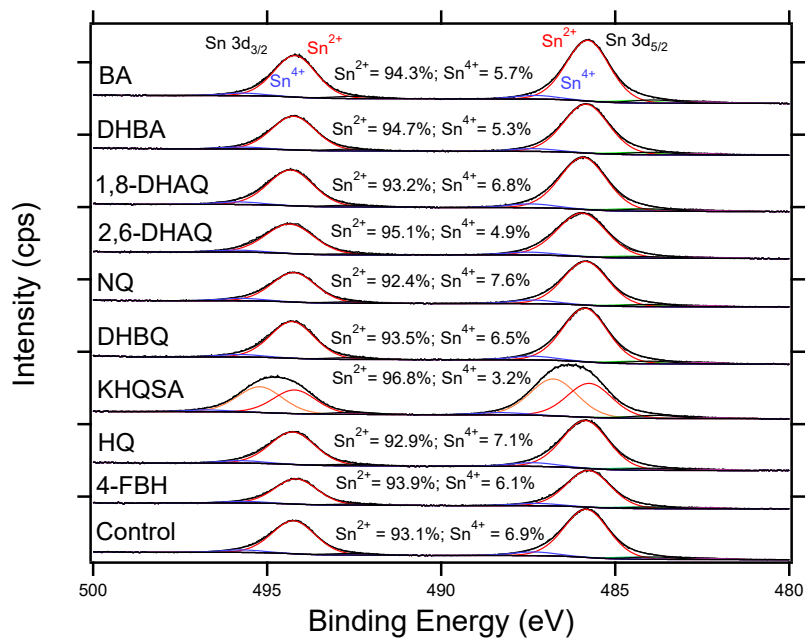
Figure 4.12 XPS spectra of the Sn 3d region for FASnI$_3$ films with fits to the Sn$^{2+}$ and Sn$^{4+}$ peaks for the films made with 2.5 mol% of varying additives.
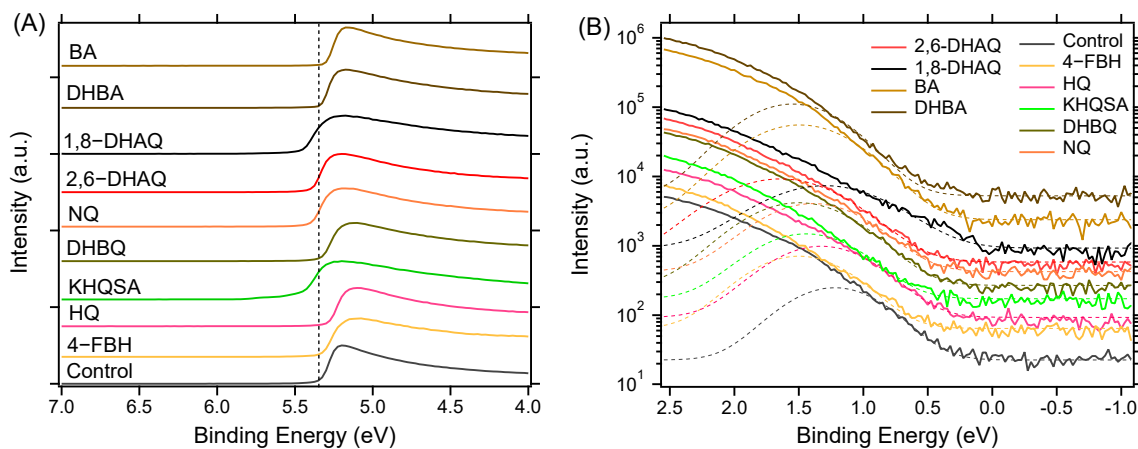


Figure 4.13 UPS spectra of FASnI$_3$ film with 2.5 mol% varying additives; A) the secondary electron cut-off regions; B) the valence band onset regions.

Table 4.3 Work Function vs. Ionization energy (IE) of 2.5 mol% additive treated FASnI$_3$ films.

| Additive | Work Function (eV) | IE (eV) |
|---|---|---|
| None (control) | 4.85 | 5.09 |
| BHzHCl | 4.50 | 5.24 |
| DHCl | 4.62 | 5.41 |
| DHCA | 4.57 | 5.13 |
| DHNT | 4.17 | 4.91 |
| HzHCl | 4.83 | 5.36 |
| DHBA | 4.86 | 5.39 |
| BA | 4.90 | 5.29 |
| 4-FBH | 4.87 | 5.36 |
| HQ | 4.97 | 5.26 |
| KHQSA | 4.73 | 5.15 |
| DHBQ | 4.88 | 5.27 |
| NQ | 4.77 | 5.10 |
| 2,6-DHAQ | 4.82 | 5.23 |
| 1,8-DHAQ | 4.72 | 4.78 |
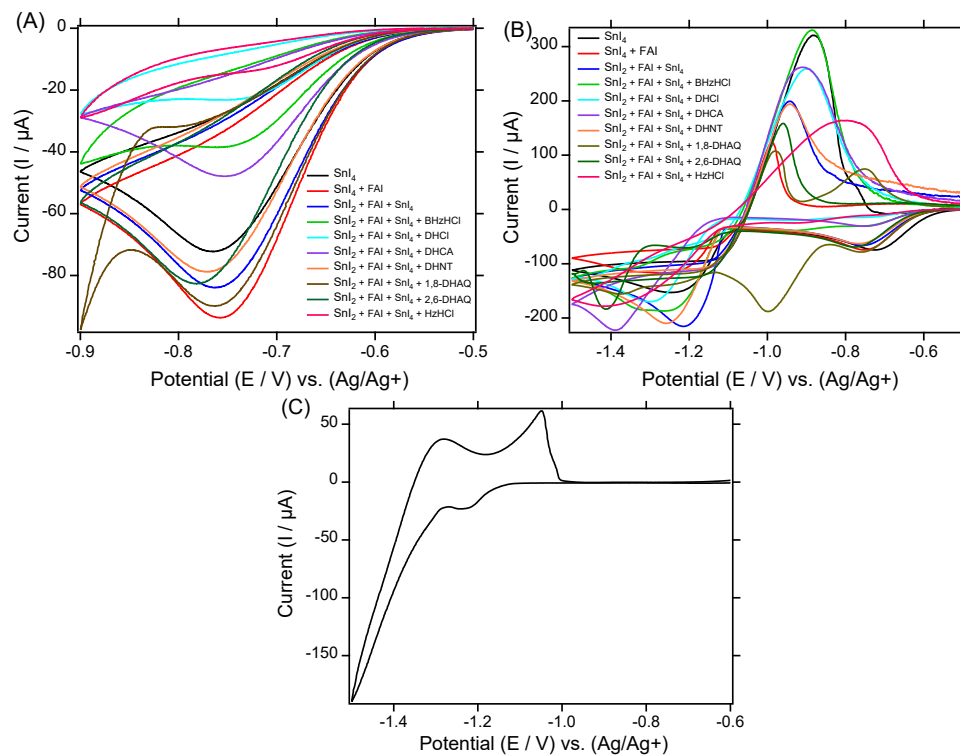
Figure 4.14 CV of (A, B) $SnI_4$, $SnI_4$ + FAI, $SnI_2$ + $SnI_4$ + FAI, and $SnI_2$ + $SnI_4$ + FAI + additive (1:1:1:1 mole ratio); and (C) $SnCl_4$ in DMF:DMSO (4:1) with 0.1 M $TBAPF_6$ as the supporting electrolyte.
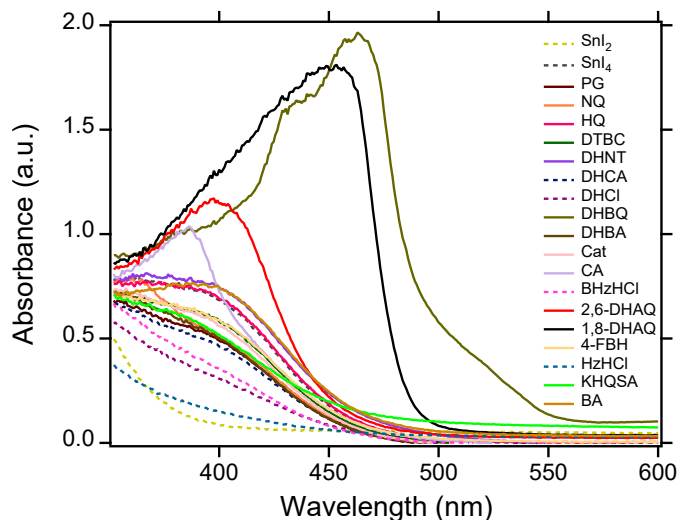


Figure 4.15 Absorbance spectra of solutions of $SnI_4$ with varying reducing additives (1:1 mol ratio) in DMF:DMSO (4:1). The spectra were recorded 10 min after addition of the additives into $SnI_4$ solution in $N_2$-filled glovebox.
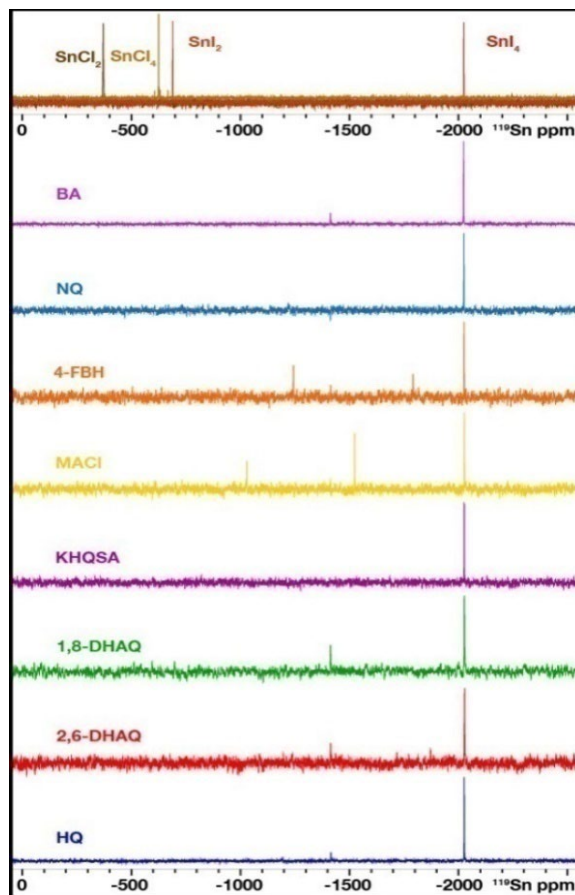
Figure 4.16 $^{119}$Sn NMR of the reference Sn compounds (SnI$_2$, SnI$_4$, SnCl$_2$, SnCl$_4$) (top) and SnI$_4$ + additive (1:1 mole ratio) in DMSO-$d_6$.

61
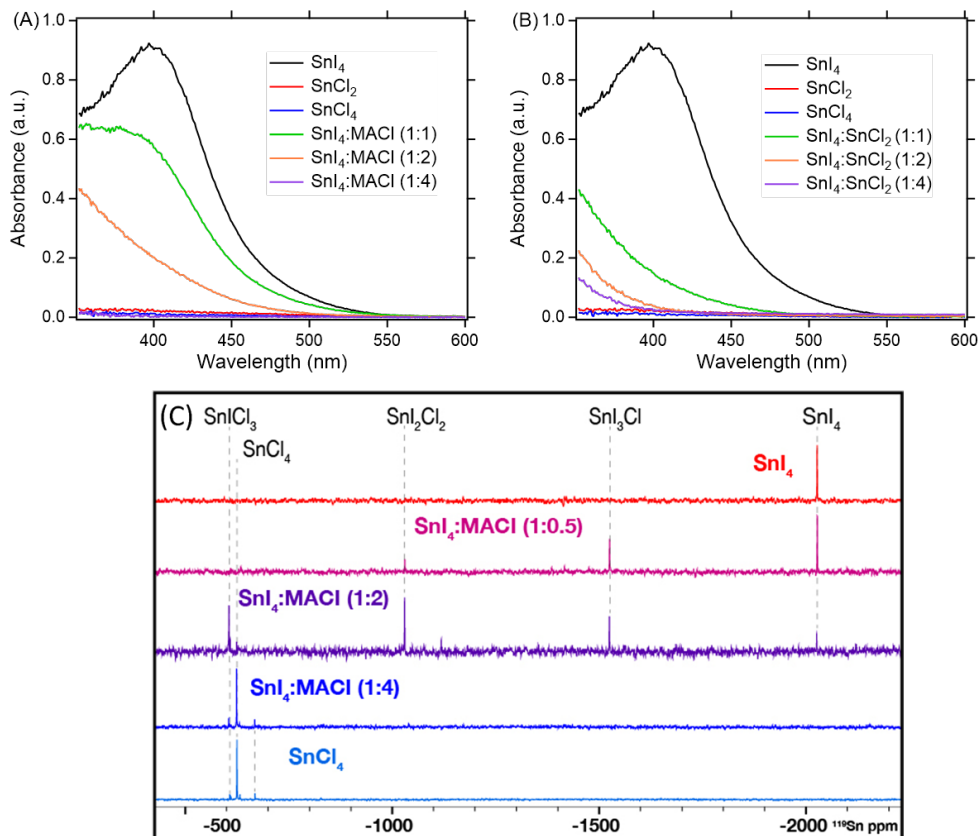
Figure 4.17 Absorbance spectra supporting that halide exchange occurs between $SnI_4$ and A) MACl and between $SnI_4$ and B) $SnCl_2$ with varying mole ratios. C) $^{119}$Sn-NMR of $SnI_4$ and MACl in DMSO-$d_6$ with varying mole ratios.
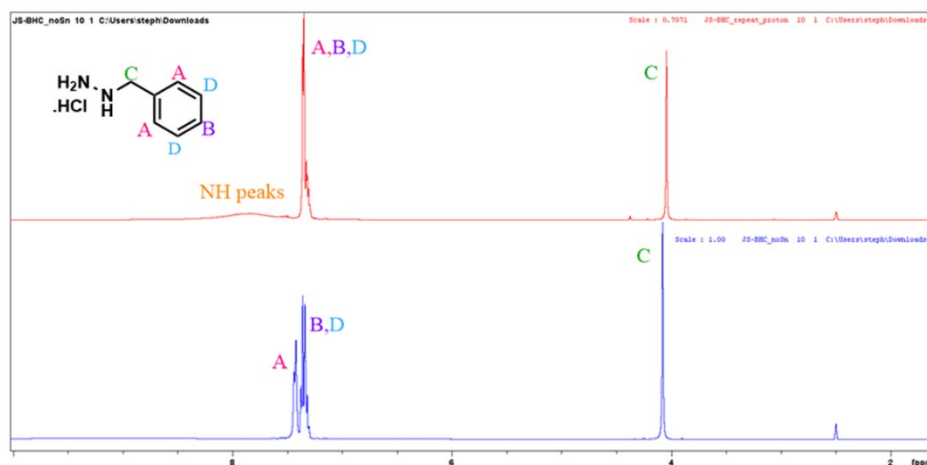


Figure 4.18 Comparison of $^1$H NMR spectra of BHzHCl ligand alone (blue) and coordinating $SnI_4$ (red) in DMSO-$d_6$, at $\delta = 2.50$ ppm.
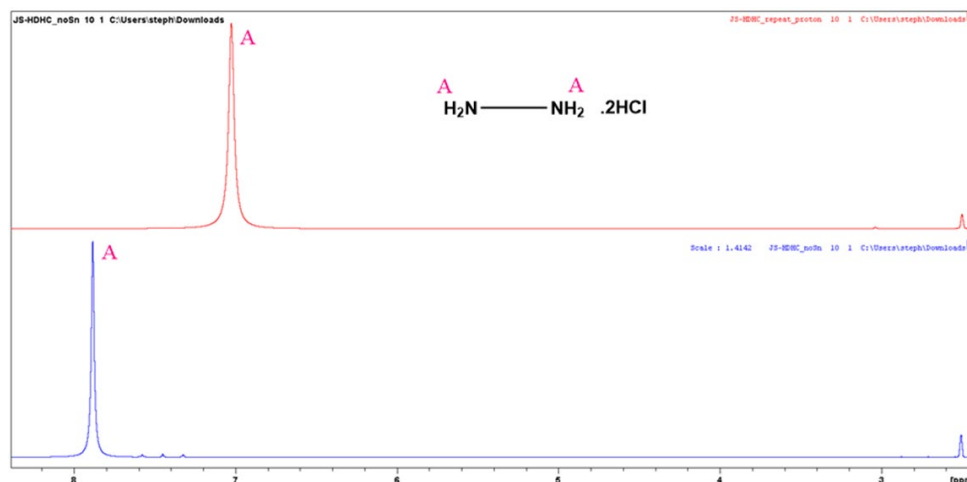
Figure 4.19 Comparison of $^1$H NMR spectra of HzHCl ligand alone (blue) and coordinating SnI$_4$ (red) in DMSO-$d_6$, at δ = 2.50 ppm.
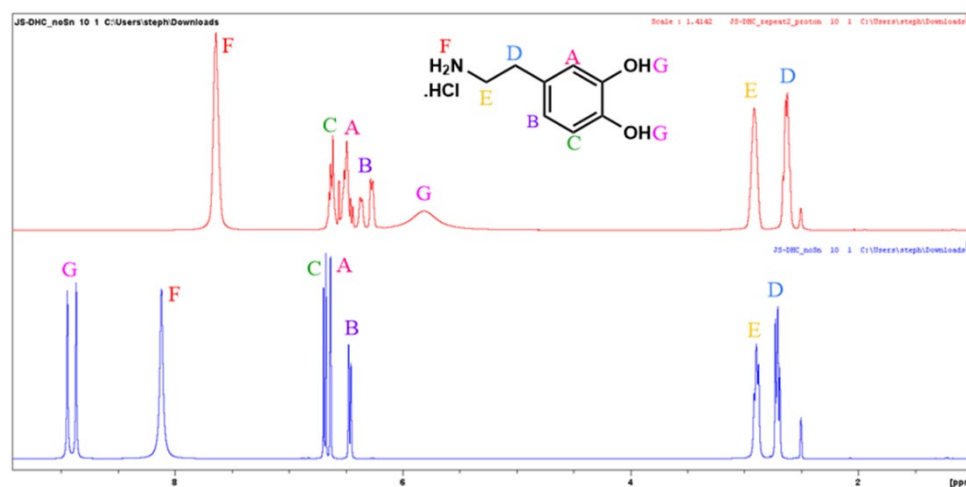


Figure 4.20 Comparison of $^1$H NMR spectra of DHCl ligand alone (blue) and coordinating SnI$_4$ (red) in DMSO-$d_6$, at δ = 2.50 ppm.
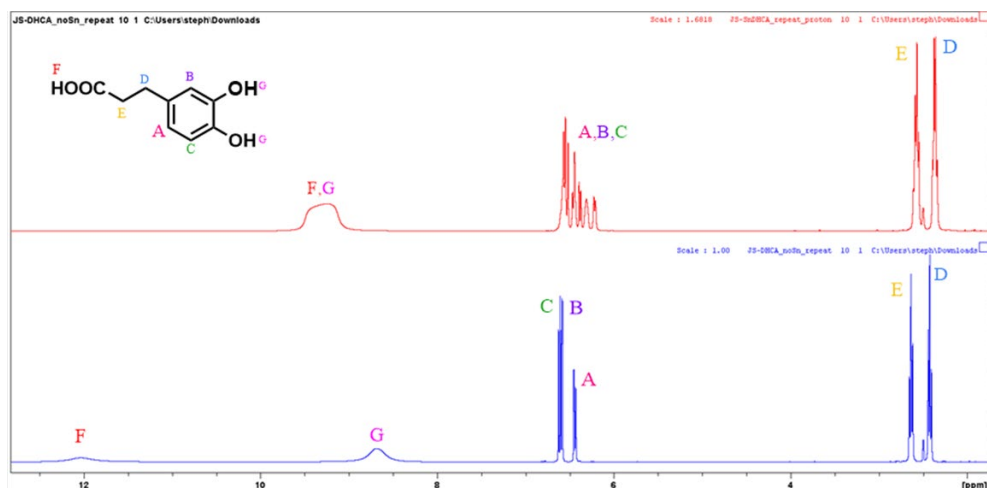
Figure 4.21 Comparison of $^1$H NMR spectra of DHCA ligand alone (blue) and coordinating SnI$_4$ (red) in DMSO-$d_6$, at $\delta = 2.50$ ppm.
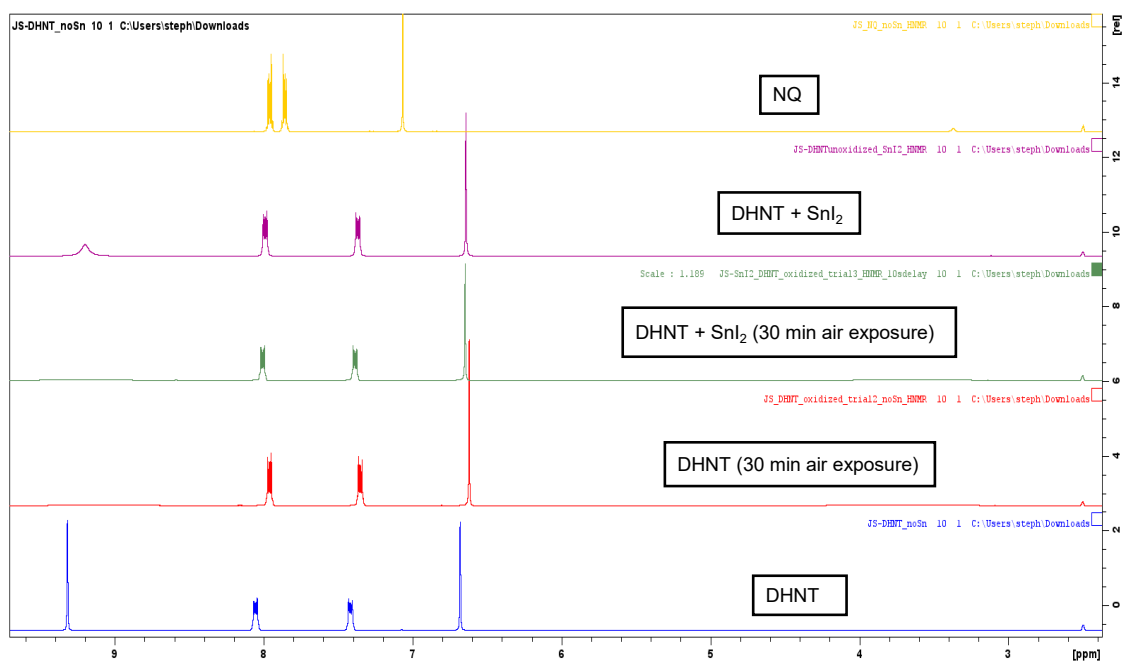


Figure 4.22 Comparison of $^1$H NMR spectra of NQ (yellow), SnI$_2$:DHNT at a 1:1 mole ratio (purple), SnI$_2$:DHNT at a 1:1 mole ratio after 30 minutes of air exposure (green), DHNT after 30 minutes of air exposure (red), and DHNT with no air exposure (blue). NQ is included to show that DHNT does not oxidize to form NQ upon air exposure. All spectra are in DMSO-$d_6$, at $\delta = 2.50$ ppm.
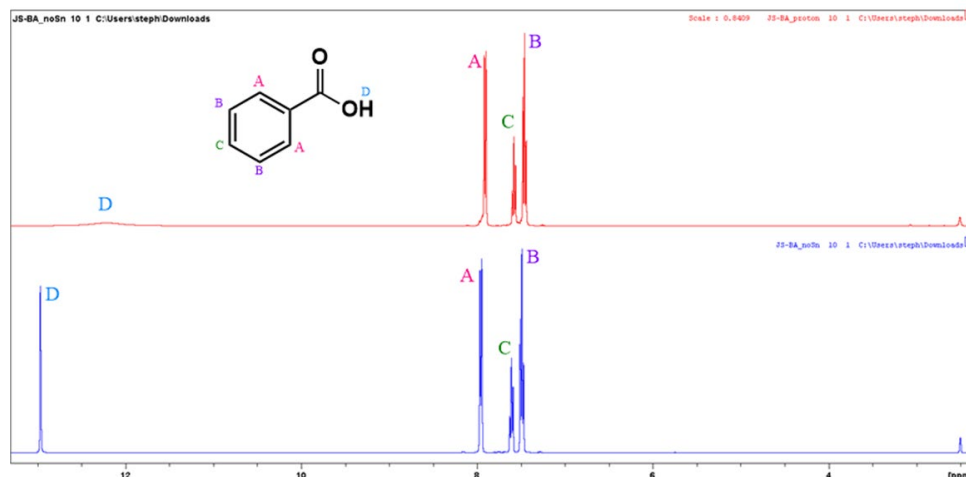
Figure 4.23 Comparison of $^1$H NMR spectra of DHBA ligand alone (blue) and coordinating SnI$_4$ (red) in DMSO-$d_6$, at δ = 2.50 ppm.
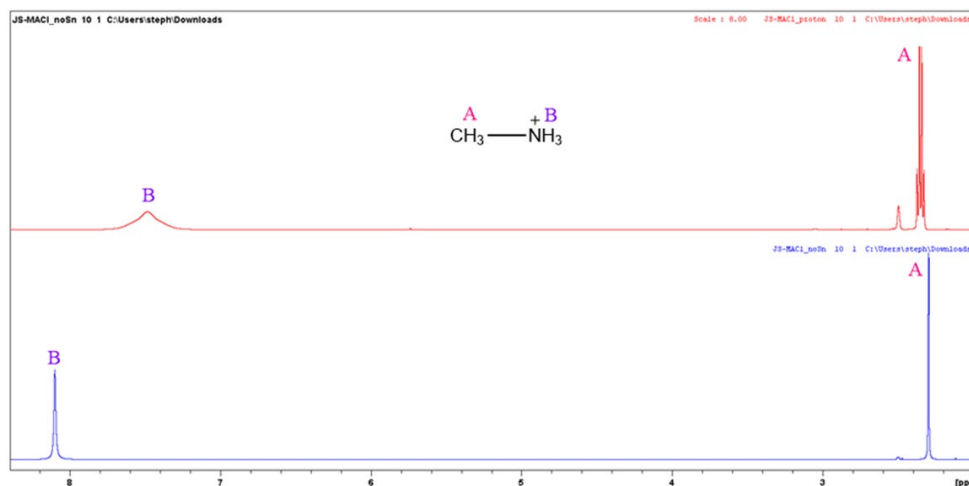


Figure 4.24 Comparison of $^1$H NMR spectra of MACl ligand alone (blue) and coordinating SnI$_4$ (red) in DMSO-$d_6$, at δ = 2.50 ppm.

CHAPTER 5. DEFECT MODULATION VIA $S_NX_2$ ADDITIVES IN FAS$_{NI3}$ PEROVSKITE SOLAR CELLS

*"Adapted with permission from Joy, S.; Hossain, T.; Tichy, A.; Johnson, S.; Graham, K.*

*R. Defects Modulation via SnX$_2$ Additives in FASnI$_3$ Perovskite Solar Cells. J. Phys. Chem.*

*Lett.* **2024,** *15, 14, 3851–3858. Copyright (2024) American Chemical Society."*

5.1    Introduction

Tin halide perovskites (Sn-HPs) have emerged as promising alternatives to lead halide perovskites (Pb-HPs). Sn-HPs have comparable optoelectronic properties to Pb-HPs, including a narrower band gap of ~1.3-1.4 eV that is more ideal for single-junction solar cells, low exciton binding energies, and relatively high charge-carrier mobility, while also  being less toxic than Pb.[80, 114-118] The record power conversion efficiency (PCE) for Sn-HPs is now 14.8%,[49] which is still significantly lower than their Pb-containing counterparts. The main reason for the inferior efficiency of Sn-HPs is ascribed to the instability of the $Sn^{2+}$ oxidation state in Sn-HPs, with minimal amounts of oxygen and/or dimethyl sulfoxide (DMSO) solvent often leading to oxidation to $Sn^{4+}$ even in an inert glovebox atmosphere.[106, 107, 119] Consequently, $Sn^{4+}$ species, *i.e.* SnI$_4$, an oxidation product of SnI$_2$, causes the release of two holes to the valence band in Sn-HPs, resulting in self-p-type doping characteristics with increased background hole density of ~$10^{20}$ cm$^{-3}$.[120, 121] In Sn-HPs it is also known that surface defects such as tin vacancies ($V_{Sn}$), caused by the formation of SnI$_4$ at the surface or grain boundaries, are thermodynamically stable and detrimental to device performance and stability.[122-124] The increased defect states at the

surface, triggered by $SnI_4$, act as electron traps and centers for non-radiative recombination.[125]

Numerous approaches have thus been adopted to retard $Sn^{2+}$ oxidation, including additives that act as anti-oxidants or passivate surfaces,[83, 84, 89] mixed A-site cations that increase stability,[113] mixed dimensional 3D/2D phases that impede moisture ingression,[73, 126, 127] and alternative solvent systems that do not oxidize $Sn^{2+}$.[128, 129] The most ubiquitous additive used in pure Sn and mixed Sn-Pb perovskites is $SnF_2$. The incorporation of $SnF_2$ into Sn-HPs precursor solution improves the substrate coverage, film morphology, and photovoltaic performance.[99, 130, 131] However, $SnCl_2$ and $SnBr_2$ can play a similar role as $SnF_2$, including improving crystallization dynamics as well as decreasing $V_{Sn}$ defect concentrations, but only a few works report using $SnCl_2$ or $SnBr_2$ as additives.[89, 132, 133]

It was previously proposed that $SnF_2$ acts as a reducing agent, either reducing the $SnI_4$ and/or suppressing the $SnI_2$ oxidation by creating a Sn-rich environment, which results in decreased Sn vacancies with less background charge carrier density.[91, 98] However, Pascual et al.[99] reported that both $SnF_2$ and $SnCl_2$ can decrease the $SnI_4$ concentration by undergoing halide exchange reactions with $SnI_4$ to form $SnF_4$ and $SnCl_4$, respectively, that can reduce the insertion of $Sn^{4+}$ into the Sn-HPs crystal lattice, leading to decreased defect states. We also showed that chloride-containing organic salts can undergo a similar halide exchange reaction with $SnI_4$, which decreases the $SnI_4$ concentration in solution as well as in thin films.[134] Recently, Meggiolaro et al.[135] reported that $SnF_2$ can decrease the $SnI_4$ concentration by forming a mixed valence $Sn_3F_8$ phase, which is thermodynamically preferred over $SnF_4$. In addition, halide ion migration is a well-recognized problem for HPs that increases hysteresis in current-voltage scans and results in decreased device stability.[60]

In addition, phase segregation is also observed in mixed-halides HPs under light or bias stress.[136, 137] However, a recent study showed that there is significantly less halide ion migration in Sn-HPs compared to Pb-HPs due to the strong Sn-halide bond.[138]

While much has been done to elucidate how $SnF_2$ improves the electronic properties and performance of Sn-HPs, a complete picture of how $SnX_2$ additives with varying halides affect the electronic and ionic defect properties in $FASnI_3$ perovskites is still missing. Herein, we use a combination of photothermal deflection spectroscopy (PDS) and ultraviolet photoemission spectroscopy (UPS) to provide insight into defect states in $FASnI_3$ films fabricated with and without $SnX_2$ additives. The activation energies of ion migration in $FASnI_3$ devices are determined using thermal admittance spectroscopy (TAS). Our results show that $SnF_2$ decreases energetic disorder in $FASnI_3$ films and decreases ion migration more than $SnCl_2$ and $SnBr_2$, while also resulting in improved film morphologies. As a result, $FASnI_3$ devices with $SnF_2$ display the highest PCE compared to devices with $SnCl_2$ and $SnBr_2$. Moreover, impurities such as $SnI_4$ and $I_2$ are intentionally introduced into the $FASnI_3$ precursor solution with $SnF_2$ as an additive, and we directly observe that $SnF_2$ decreases the detrimental effects of $SnI_4$.

## 5.2    Experimental Details

*Materials*

Tin powder (99.8%, Sigma Aldrich), iodine (99.8%, Thermo Scientific), tin (IV) iodide ($SnI_4$, 99.99%, Alfa Aesar), tin (II) fluoride ($SnF_2$, 99.99%, Acros Organics), tin (IV) fluoride ($SnF_4$, 99% metals basis, Thermo Scientific),  tin (II) chloride ($SnCl_2$, 98%, Fluka), tin (IV) chloride ($SnCl_4$, 99.99% trace metals basis, Beantown chemical), tin (II)

bromide (SnBr$_2$, 99.2%, Alfa Aesar), tin (IV) bromide (SnBr$_4$, 99%, Strem Chemicals), formamidinium iodide (FAI, Greatcell solar), ethane-1,2-diamine (EDA, 99%, Alfa Aesar), poly(3,4-ethylenedioxythiophene) polystyrene sulfonate (PEDOT:PSS, Clevios PVP.Al 4083 Heraeus), indene-C$_{60}$ bisadduct (ICBA, Nano-C), bathocuproine (BCP, 99.0%, TCI), silver (99.99%, Kurt J. Lesker), perfluorohexanes (98%, Alfa Aesar), anhydrous N,N-dimethylformamide (DMF, 99.98%, DriSolv®), anhydrous dimethyl sulfoxide (DMSO, 99.9%, Sigma-Aldrich), anhydrous toluene (99.8%, Alfa Aesar), anhydrous chlorobenzene (CB, 99.8%, Acros Organics), deuterated dimethyl sulfoxide (DMSO-$d_6$, 99.5%, Cambridge Isotope Laboratories), indium tin oxide (ITO) coated glass (12 Ω/□). All chemicals other than solvents were used as received without further purification. Prior to use, all solvents were degassed by three freeze-pump-thaw cycles to remove dissolved oxygen and then dried over molecular sieves.

*Synthesis of SnI$_2$*

SnI$_2$ was synthesized according to the literature.[73] In brief, 3.0457 g of iodine was dissolved completely in 2.50 mL of DMSO by vortex mixing, followed by the addition of 12.50 mL of DMF (DMF:DMSO= 5:1, v/v) to form 0.8 M I$_2$ solution. Excessive tin powder was added into I$_2$ solution, and then the solution was kept stirring at room temperature for 12 hours to form 0.8 M SnI$_2$ solution.

*Perovskite precursor preparation*

1 mL of 0.8 M precursor solution in DMF:DMSO (5:1) was prepared by mixing FAI (0.1376 g) and SnI$_2$ in a 1:1 molar ratio. 7.5 mol% (w.r.t. SnI$_2$) of additives *i.e.*, SnF$_2$, SnCl$_2$ or SnBr$_2$ was added to the FASnI$_3$ precursor mixture, respectively. The resulting

mixture was dissolved by vortex mixing for 5 min, and then heated at 60 $^{\circ}$C for 1 hour. After cooling, the solution was filtered through a 0.2 μm PTFE filter immediately prior to use.

*Device Fabrication*

ITO patterned glass was cleaned through sequential sonication with a sodium dodecylsulfate solution, deionized water, acetone, and 2-propanol for 20 minutes each, followed by 20 min UV-ozone cleaning. Before deposition, PEDOT:PSS solution was filtered through a 0.45 μm Nylon filter, followed by spin coating at 5000 rpm for 30 s, and then annealed at 140 $^{\circ}$C for 10 min in air. After annealing, PEDOT:PSS-coated ITO substrates were immediately transferred to the $N_2$-filled glovebox with oxygen and moisture levels of <0.1 ppm. Film processing inside the glovebox was carried out under continuous $N_2$ purging to remove solvent vapors. The $FASnI_3$ precursor solution with additives was prepared inside the glovebox as described above. Then, the precursor solution was spun-cast at 8000 rpm with 0 s ramp time for 60 s while 120 μL of CB was dropped after 12 s of spinning. The resulting perovskite film was annealed at 80 $^{\circ}$C for 10 min. After cooling the substrates, 100 μL of EDA (0.1 mM in toluene) was dynamically spun-cast on $FASnI_3$ films at 5000 rpm for 30 sec, followed by annealing at 80 $^{\circ}$C for 3 min. Then, 40 μL of ICBA (20 mg/mL in CB) was spun-cast at 1200 rpm for 30 s, followed by annealing at 100 $^{\circ}$C for 10 min. The substrates were then transferred to a thermal evaporator chamber without being exposed to air. Finally, 5 nm BCP (0.25 Å/s) and 100 nm Ag (10 nm at 0.5 Å/s and 90 nm at 2.0 Å/s) were thermally evaporated under a base pressure of $< 2\times10^{-6}$ mbar using an Angstrom Engineering deposition system.

*Device characterization*

The devices were characterized using a solar simulator (ABET technologies, 11002) with simulated AM 1.5G solar illumination at 1 sun (100 mW/cm$^2$). The light intensity was calibrated by a silicon photodiode (Thorlabs, FDS1010-CAL) under a KG2 filter. All devices have an active area of 0.1 cm$^2$. The current density-voltage (J-V) curves were recorded in the N$_2$-filled glovebox and scanned from -0.2 V to 1.2 V in forward direction and from 1.2 V to -0.2 V in reverse direction with a 0.01 V step size and 10 ms delay time using a Keithley 2450 source meter. Thermal admittance spectroscopy (TAS) experiments were carried out using a Zurich Instruments MFLI lock-in amplifier and a liquid nitrogen cooled cryo-station (Janis ST100) equipped with a Lakeshore 336 temperature controller. TAS was performed in the temperature range of 160 K to 300 K with a step size of 10 K. All temperatures were stabilized within ±1 K for 10 min before measurement. All measurements were recorded under dark at 0 V DC bias and 10 mV AC bias amplitude with AC frequency ranging from 10 Hz to 1 MHz. Capacitance-voltage (C-V) measurements were performed under dark at 10 mV AC bias and 10 kHz AC frequency. The thermal emission rate ($e_p$) for a given trap is calculated by the following equation:

$$e_p = N_V < v_{th} > \sigma_p \exp\left(\frac{-E_a}{kT}\right) = \vartheta_0 \exp\left(\frac{-E_a}{kT}\right)$$

where $N_V$ is the effective density of states of the valence band, $v_{th}$ is the average thermal velocity, $\sigma_p$ is the capture cross section of the trap state, $\vartheta_0$ is the temperature independent attempt-to-escape frequency, T is the measured temperature, $E_a$ is the trap activation energy, and $e_p$ is the measurement frequency (f) at which trap peak occurs. The $E_a$ is

determined from the fitting of Arrhenius plot ($\ln(f/T^2)$ vs. $1/T$) obtained at different T, where the slope gives the $E_a$.[66, 70]

*Absorbance and photoluminescence spectroscopy*

UV-vis absorbance spectra were collected using an Ocean Optics QE Pro high-performance spectrometer. For solution absorbance measurements, the final concentration of analytes was kept at 1.0 mM in DMSO. For thin film measurements, perovskite films were deposited on glass substrates as described before. Photoluminescence (PL) spectra of thin films were collected using a 532 nm laser (Thorlabs, CPS532) and an Ocean Optics QE pro high-performance spectrometer with 1100 ms integration time and 100 μm slit width.

*X-ray diffraction*

Perovskite films for XRD measurements were prepared on non-pattered ITO coated glass as mentioned before. The XRD patterns were recorded with a Bruker-AXS D8 DISCOVER diffractometer with Cu Kα radiation ($\lambda$ = 1.5418 Å) operating at 40 kV and 40 mA.

*Scanning electron microscopy (SEM)*

Perovskite films for SEM image were fabricated on continuous ITO coated glass as described before. SEM images were collected using Helios Nanolab 660/G3 duel-beam SEM instrument from ThermoFisher Scientific with voltage 2.0 kV and current 0.2 nA.

*X-ray and ultraviolet photoemission spectroscopy (XPS and UPS)*

XPS and UPS measurements were carried out in a PHI 5600 ultra-high vacuum (UHV) system under a base pressure of $< 5 \times 10^{-10}$ mbar. All films were prepared on non-pattered ITO/PEDOT:PSS coated substrates according to the procedure as described previously. The as-prepared films were transferred into the UHV chamber without air exposure through a glovebox under $N_2$ atmosphere. XPS measurements were carried out using an Al Kα source (1486.6 eV) with a pass energy of 23.5 eV. UPS measurements were conducted with 10.2 eV photons for excitation using an Excitech H Lyman-α lamp. The pass energy of 5.85 eV was used, and a -5 V bias was employed in all UPS measurements. All measurements were conducted within 24 hours of sample preparation, and the samples were kept entirely under nitrogen (<0.1 ppm $O_2$ and $H_2O$).

*$^{119}$Sn NMR*

The reference solutions *i.e.,* 0.5 M of $SnI_4$, $SnI_2$, $SnF_2$, $SnF_4$, $SnCl_2$, $SnCl_4$, $SnBr_2$, $SnBr_4$, and a mixture of $SnI_4$ with $SnF_2$, $SnCl_2$, and $SnBr_2$ in a 1:2 mole ratio, respectively, were prepared in anhydrous and degassed DMSO-*$d_6$* solvent. All solutions were filtered through 0.2 μm PTFE filters before measurements. $^{119}$Sn NMR experiments were conducted with a Bruker Advance NEO (400 MHz) spectrometer equipped with a 5mm broadband SmartProbe. All measurements were carried out at 298K. $Sn(CH_3)_4$ was used as an external reference (δ = 0.00 ppm). $^{119}$Sn was detected using the spectral width of 500 kHz, 3.33 μs 30° excitation pulse with 4 s relaxation delays between transients, and 2048 scans.

*Photothermal deflection spectroscopy (PDS)*

PDS measurement was carried out according to the literature.[119, 139] The Urbach energy ($E_U$) is determined from the following equation:

$$ln\alpha = \frac{1}{E_U}E - \frac{E_g}{E_U} + ln\alpha_0$$

where, $\alpha$ is the absorption coefficient, $\alpha$o is the material dependent constant, $E$ is the photon energy, $E_g$ is the band gap energy. The inverse slope of the linear fit determines $E_U$ energy.

## 5.3   Results and Discussion

To qualitatively probe halide exchange with $SnX_2$ additives, we prepared mixed solutions of $SnI_4$ with $SnF_2$, $SnCl_2$, and $SnBr_2$, respectively, and first examined the solution color change. As shown in Figure 5.1a, the red color of the initial $SnI_4$ solution turns colorless, yellow, or orange after the addition of $SnF_2$, $SnCl_2$, or $SnBr_2$, respectively, and the absorbance of $SnI_4$ decreases as evidenced by the UV-vis absorbance spectra (Figure 5.6). While readily observable color changes and UV-vis absorbance measurements provide a qualitative indicator that the $SnI_4$ concentration is reduced upon addition of $SnX_2$, ^{119}Sn NMR can provide a more comprehensive picture of the different Sn species in the mixed solution. Here, $SnI_4$ shows a peak at a chemical shift of -2023 ppm while the $SnI_2$ peak appears at -699 ppm (Figure 5.1b). As previously reported,[99] $SnI_4$ is able to undergo complete halide exchange with $SnF_2$ when mixed at 1:2  ($SnI_4$:$SnF_2$) mole ratio, and we observe similar results. When $SnF_2$ is mixed with $SnI_4$, there is a disappearance of the $SnI_4$ signal in the ^{119}Sn NMR and a corresponding increase in two new peaks at -700 and -771

ppm, confirming the formation of $SnF_4$ and $SnI_2$. This halide exchange occurs because F is a highly electronegative anion with hard Lewis base character, and it has a greater affinity towards the harder $Sn^{4+}$ Lewis acid as opposed to the softer $Sn^{2+}$. Therefore, $F^-$ replaces $I^-$ from $SnI_4$ and forms $SnF_4$ and $SnI_2$.[99] Similarly, reaction with $SnCl_2$ completely eliminates the $SnI_4$ signal through the formation of $Sn^{4+}$ complexes, *i.e.*, $SnCl_4$ and/or $SnI_xCl_y$ species with signals at -606, -610, -625 and -634 ppm (reference $SnCl_4$ peak appears at -625 ppm), and no $SnI_2$ is observed. When $SnBr_2$ is mixed with $SnI_4$, four signals show up at -583, -1013, -1270, and -1347 ppm (reference $SnBr_4$ shows two peaks at -1013 and -1270 ppm) and again no $SnI_4$ peak remains. However, while $SnF_2$ leaves no doubt that complete halide exchange to form $SnI_2$ and $SnF_4$ occurs, both $SnCl_2$ and $SnBr_2$ show evidence of incomplete halide exchange (*i.e.*, the formation of $SnI_xCl_y$ and $SnI_xBr_y$, where x and y are both greater than zero).
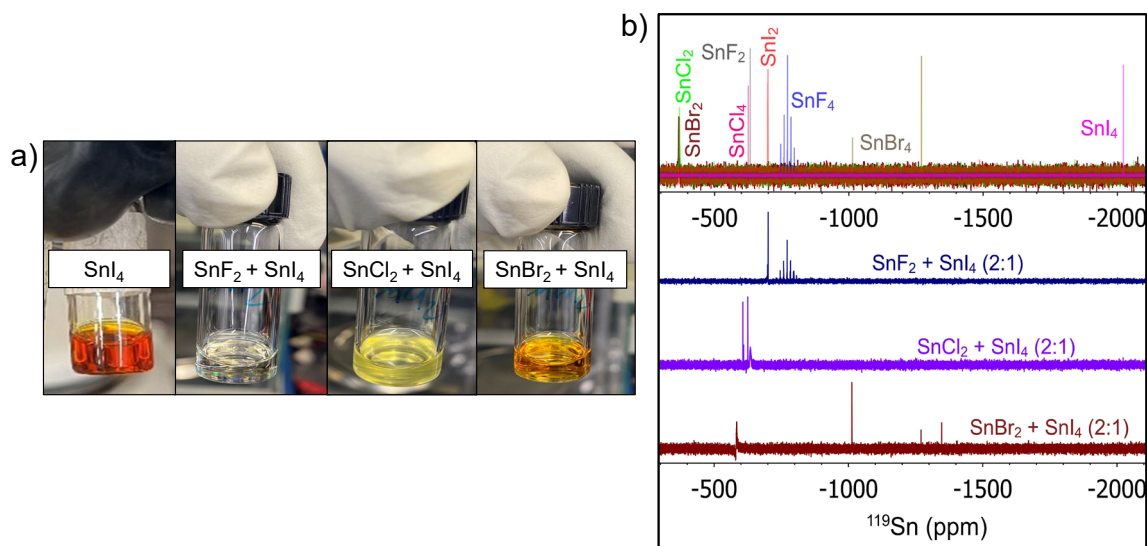


Figure 5.1 a) Photographic images of 0.5 M solution of reference $SnI_4$ and a mixture of $SnF_2$, $SnCl_2$, and $SnBr_2$ with $SnI_4$ (2:1 mole ratio), respectively, in DMSO. b) ^{119}Sn NMR of the reference Sn compounds (top), and a mixture of $SnF_2$, $SnCl_2$, and $SnBr_2$ with $SnI_4$ (2:1 mole ratio), respectively, in DMSO-$d_6$.

With a clear picture of solution behavior, we next turn to understand how different

$SnX_2$ additives affect the $FASnI_3$ perovskite thin film properties. To do so, $FASnI_3$ was

fabricated with 7.5 mol% $SnX_2$ additives. The XRD spectra of the resulting perovskite

films show no new peaks or significant peak shifts upon the addition of $SnX_2$ additives

compared to the reference $FASnI_3$ film (Figure 5.7a). SEM images (Figure 5.8) show that

in the case of $FASnI_3$ + $SnF_2$ the grain size increases compared to the $FASnI_3$ film without

$SnX_2$ additives. This increase in grain size with $SnF_2$ is attributed to the ability of $SnF_2$ to

slow the prompt nucleation of Sn-HPs, which helps increase the grain size.[131, 140] On the

contrary, $FASnI_3$ + $SnCl_2$ and $FASnI_3$ + $SnBr_2$ films exhibit similar or worse morphologies

than the pristine $FASnI_3$ film. Here, $SnCl_2$ leads to similar morphologies as observed for

the control while $SnBr_2$ results in a significantly higher pin-hole density. Since $SnI_4$ and $I_2$

are degradation products of Sn-HPs, we then intentionally added 2 mol% $SnI_4$ and 2 mol%

$I_2$ to $FASnI_3$ + $SnF_2$ precursor solutions. The XRD patterns with $SnI_4$ or $I_2$ introduced show

no major changes relative to the control. The SEM images show that grain sizes decrease

and pinhole densities increase upon addition of $SnI_4$, and with $I_2$ the grain sizes and pinhole

densities are similar to the pristine $FASnI_3$ film.

To quantify how the $SnX_2$ additives impact disorder at the band-edge in the $FASnI_3$

thin films, we carried out PDS measurements, as shown in Figure 5.2a. The Urbach energy

($E_U$) is evaluated from the exponential function of the decaying absorption onset tail at the

band edge,[53] and provides a quantitative measurement of energetic disorder at and near the

band edge. The lower the $E_U$ value, the less energetic disorder is present. The pristine

$FASnI_3$ film shows an $E_U$ of 37 meV, which decreases to 19 meV with $SnF_2$. The $E_U$ of

$FASnI_3$ with $SnCl_2$ and $SnBr_2$ are 30 and 33 meV, respectively, which are significantly

higher than the $FASnI_3 + SnF_2$ film but less than the pristine $FASnI_3$ film. Therefore, all $SnX_2$ additives decrease electronic disorder at the band-edge, with $SnF_2$ proving more effective than $SnCl_2$ and $SnBr_2$. When an intentional impurity of 2% $SnI_4$ is added to the $FASnI_3 + SnF_2$ solution, the resulting $E_U$ of the film increases to 26 meV. This $E_U$ is still significantly lower than the 37 meV observed for the film without $SnF_2$ and no added impurities. On the contrary, the $E_U$ is further increased to 47 meV after adding 2% $I_2$ to the $FASnI_3 + SnF_2$ solution. It is reported that when $I_2$ is formed during the degradation of Sn-HPs, it facilitates the further oxidation of $SnI_2$.[106, 141] As a result, $I_2$ addition consumes $SnI_2$ from the precursor solution and makes the solution more Sn deficient as compared to when $SnI_4$ is added. This increased Sn deficiency could result in increased $V_{Sn}$ and/or Frenkel pair type defects, leading to more energetic disorder in the material.
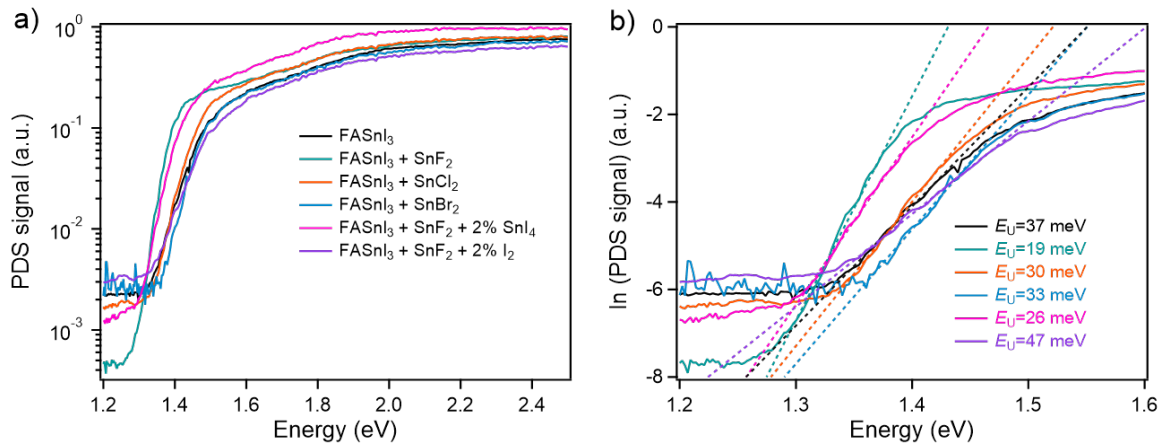


Figure 5.2 PDS spectra on a semi-log plot (a) and after taking the natural log of the PDS signal (b) to extract the Urbach energy ($E_U$) of $FASnI_3$, $FASnI_3 + SnF_2$, $FASnI_3 + SnCl_2$, $FASnI_3 + SnBr_2$, $FASnI_3 + SnF_2 + 2\%$ $SnI_4$, and $FASnI_3 + SnF_2 + 2\%$ $I_2$ films.

The PDS spectra also show that the absorption onset of the $FASnI_3 + SnF_2$ film red shifts by 60 meV with respect to the pristine $FASnI_3$ film. The red shift of this absorbance onset for the $FASnI_3 + SnF_2$ film is also confirmed by the UV-vis absorbance spectra

(Figure 5.9). On the other hand, $FASnI_3$ films with $SnCl_2$ and $SnBr_2$ show similar absorption onsets as the pristine $FASnI_3$ film. The increased $Sn^{4+}$-related defects likely induce more lattice distortion, which increases the optical gap.[142] These trends are consistent with the Urbach energies and suggest that $Sn^{4+}$ associated defects increase the optical gap.

Photoluminescence (PL) measurements were carried out to gain insight into radiative and nonradiative recombination dynamics. All films are prepared on glass substrates for PL measurements to avoid quenching by the electrodes or transport layers. As shown in Figure 5.10a and b, the PL intensity of $FASnI_3$ + $SnF_2$ is 6.6 times higher than pristine $FASnI_3$, which is consistent with decreased non-radiative recombination at defect sites following $SnF_2$ addition. Also, the emission peak of $FASnI_3$ + $SnF_2$ film red shifts by ~15 nm and the full-width half maxima (FWHM) decreases from 82 nm to 70 nm compared to the pristine $FASnI_3$ film. In contrast, the PL intensities of $FASnI_3$ with $SnCl_2$ and $SnBr_2$ are more comparable to pristine $FASnI_3$, with $SnCl_2$ and $SnBr_2$ showing slightly increased and decreased emission intensity, respectively, relative to pristine $FASnI_3$. Furthermore, the FWHM with $SnCl_2$ and $SnBr_2$ is 79 and 73 nm, respectively, which are narrower than pristine $FASnI_3$ and wider than with $SnF_2$. The emission peaks with $SnCl_2$ and $SnBr_2$ blue shift by 9 nm compared to pristine $FASnI_3$. Considering that the Urbach energies with $SnCl_2$ and $SnBr_2$ are lower than the pristine $FASnI_3$, we suspect the blueshift in emission may be due to a small amount of Cl and Br incorporation into the $FASnI_3$ lattice. This Cl or Br incorporation is consistent with the (001) plane peak shift to a slightly higher diffraction angle with $SnCl_2$ and $SnBr_2$ addition (see Figure 5.7b). Similar to the PDS results, it appears that the 2% $SnI_4$ impurity addition is compensated by the presence of

78

SnF$_2$, as it shows higher PL intensity and slightly redshifted emission compared to the pristine FASnI$_3$ film. On the other hand, the emission peak with 2% I$_2$ is much broader with FWHM of ~95 nm and the intensity is ~2 times lower than the control FASnI$_3$ film.
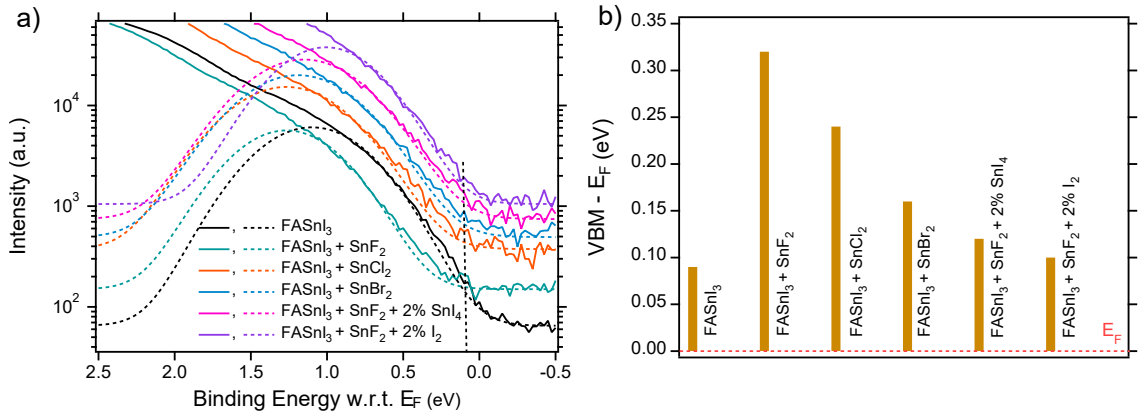


Figure 5.3 a) UPS spectra zoomed into the valence band maxima (VBM) region with the Gaussian fits used to extract the VBM onset energy displayed (dashed lines) and b) difference between the VBM and Fermi energy (E$_F$).

Ultraviolet photoemission spectroscopy (UPS) can provide insight into the p-type characteristic of the respective Sn-HP films. Here, more Sn$^{4+}$ in the film will lead to more p-type character as the p-type charge carriers (holes) increase with increasing Sn$^{4+}$ in FASnI$_3$. The extent of p-type doping is related to the energy difference between the valence band maximum (VBM) and the Fermi energy (E$_F$), where this energy difference decreases as the amount of p-type charge-carriers increases. The pristine FASnI$_3$ film without any additives shows a WF of 4.60 eV and VBM of 0.09 eV vs. E$_F$ (Figure 5.3, SI Figure 5.11 and Table 5.2). The Sn$^{4+}$ and Sn$^{2+}$ content determined by X-ray photoelectron spectroscopy (XPS) is 8.2% and 91.8%, respectively, in the pristine FASnI3 film (Figure 5.12 and Table 5.3). In the case of FASnI$_3$ + SnF$_2$, a deeper WF of 4.73 eV is determined and the VBM lies 0.32 eV away from E$_F$, which confirms that SnF$_2$ decreases the p-type character of the

FASnI$_3$ film. The XPS spectra confirm that the Sn$^{4+}$ content decreases upon SnF$_2$ addition, with the FASnI$_3$ + SnF$_2$ film displaying a Sn$^{4+}$ concentration of 6.1% as compared to 8.2% for the control film in the near-surface region. In the case of FASnI$_3$ with SnCl$_2$ and SnBr$_2$, the difference between the VBM and E$_F$ is greater than for pristine FASnI$_3$ and less than with SnF$_2$. These trends further support that SnCl$_2$ and SnBr$_2$ both play a role in passivating Sn$^{4+}$ associated defects, yet both are less effective than SnF$_2$. Surprisingly, the addition of 2% SnI$_4$ and 2% I$_2$ to the FASnI$_3$+SnF$_2$ solution leads to more p-type character and higher Sn$^{4+}$ concentrations of 13.5% and 12.8%, respectively. Additionally, the addition of both SnCl$_2$ and SnBr$_2$ increase the Sn$^{4+}$ content detected by XPS. Such increases in Sn$^{4+}$ relative to pristine FASnI$_3$ does not agree with the PDS and PL intensity trends, which could be attributed to differences between the film surface probed by XPS and UPS and the bulk film probed by PDS and PL. For example, we expect that the majority of Sn$^{4+}$ is at the film surface or at grain boundaries, as theoretical calculations indicate that Sn$^{4+}$formation is unfavorable in the bulk and highly favorable at the surface.[99, 120, 122]

To understand how electronic defects impact the FASnI$_3$ photovoltaic (PV) devices with and without SnX$_2$ additives, we fabricated p-i-n devices with a ITO/PEDOT:PSS/FASnI$_3$/ICBA/BCP/Ag structure. The current density-voltage (*J-V*) plots and statistical distributions of PV performance of the corresponding devices are shown in Figure 5.4a-e. The best performing control FASnI$_3$ device without SnX$_2$ additives has a PCE of 1.39% (average of forward and reverse scans), with a $J_{SC}$, $V_{OC}$, and FF of 5.22 mA·cm$^{-2}$, 0.520 V, and 0.513, respectively (Table 5.1). In the case of the FASnI$_3$ + SnF$_2$ devices, the best performing device shows a $J_{SC}$ of 17.5 mA·cm$^{-2}$, $V_{OC}$ of 0.641 V, and FF of 0.665 and thus a PCE of 7.47% (average of forward and reverse scans), which

corresponds with the decrease in defect states observed upon $SnF_2$ addition. On the contrary, the best performing cells with $SnCl_2$ and $SnBr_2$ show PCEs close to the control device *i.e.*, 1.84% and 1.20%, respectively. Such results are comparable to previous Sn-HP devices, where devices with $SnCl_2$ and $SnBr_2$ as additives reach PCEs of 2.71 and 0.35%, respectively.[133] The improvement in PCE with $SnCl_2$ relative to the control may be attributed to the lower energetic disorder and decreased p-type character, while the decreased average performance with $SnBr_2$ compared to the control likely stems from the poor film morphology.

There are multiple reports on halide perovskite devices where there is a correlation between $E_U$ and $V_{OC}$ deficit along with their PV performance.[52, 53, 143] We observe a similar trend, with the $V_{OC}$ of $FASnI_3$ + $SnF_2$ surpassing the $V_{OC}$ of the pristine $FASnI_3$ devices and the devices with $SnCl_2$ and $SnBr_2$. Moreover, large grain sizes and fewer grain boundaries lead to less non-radiative recombination and higher shunt resistance, resulting in higher $J_{SC}$, $V_{OC}$, and FF of $FASnI_3$ + $SnF_2$ device. In the case of $FASnI_3$ with $SnCl_2$ and $SnBr_2$, smaller grains and higher pinhole densities relative to with $SnF_2$, as seen from SEM images (Figure 5.8), likely contribute further to the decreased PV performance. In general, the much more pronounced PCE increase with $SnF_2$ arises from the culmination of multiple beneficial effects, including the complete conversion of $SnI_4$ to $SnF_4$, significantly decreased energetic disorder observed with PDS, largest decrease in p-type character, greatest proportion of radiative emission, and uniform film morphologies with increased grain sizes.
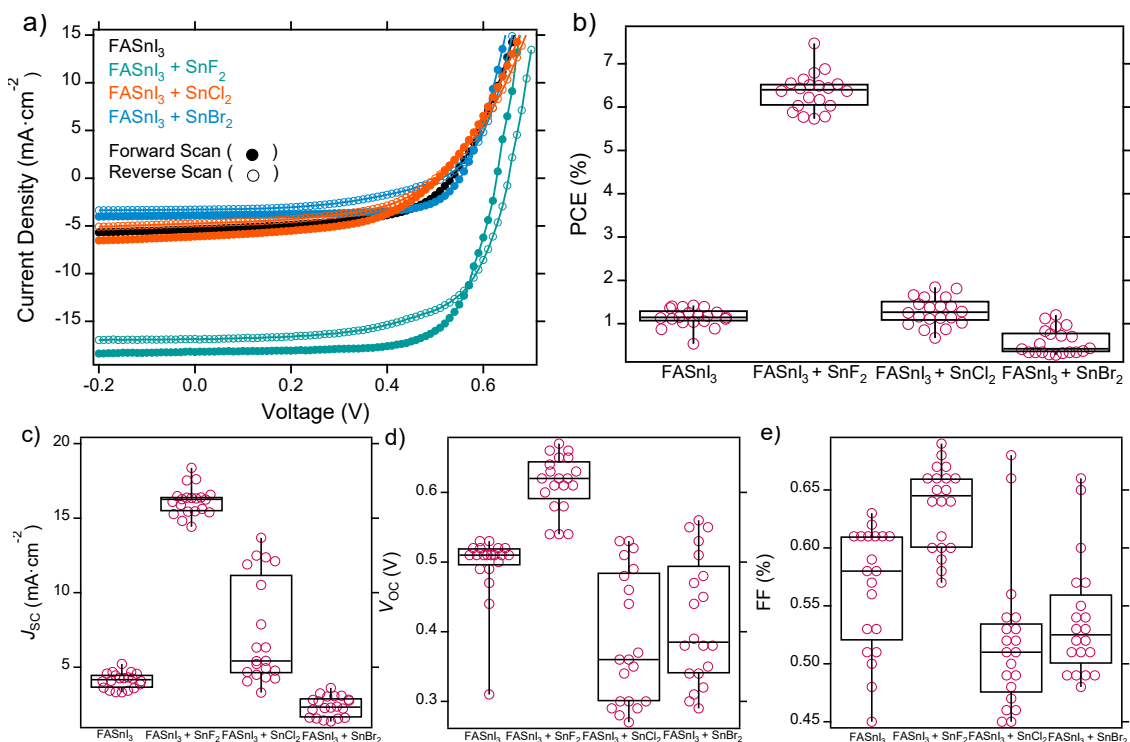
Figure 5.4 a) Current density-voltage (*J-V*) plots, and statistical distributions of b) power conversion efficiency (PCE), c) short-circuit current ($J_{SC}$), d) open-circuit voltage ($V_{OC}$), and e) fill factor (FF) for FASnI$_3$, FASnI$_3$ + SnF$_2$, FASnI$_3$ + SnCl$_2$, and FASnI$_3$ + SnBr$_2$ devices.

Table 5.1 Photovoltaic performance

| Samples | | $J_{SC}$ (mA·cm$^{-2}$) | $V_{OC}$ (V) | FF | PCE (%) |
|---|---|---|---|---|---|
| FASnI$_3$ | Average* | 4.09±0.54 | 0.494±0.050 | 0.561±0.058 | 1.15±0.24 |
| FASnI$_3$ + SnF$_2$ | Average | 16.1±1.2 | 0.612±0.041 | 0.634±0.047 | 6.35±0.76 |
| FASnI$_3$ + SnCl$_2$ | Average | 7.22±3.43 | 0.388±0.132 | 0.516±0.086 | 1.28±0.56 |
| FASnI$_3$ + SnBr$_2$ | Average | 2.37±0.68 | 0.414±0.117 | 0.535±0.082 | 0.575±0.333 |

*Average value is calculated from the forward and reverse scans of 20 devices.

82

To calculate the carrier concentration in FASnI$_3$ PV cells with and without SnX$_2$ additives, the capacitance-voltage (C-V) measurement was performed using the Mott-Schottky approach according to the following equation[65]:

$$\frac{1}{C^2} = \frac{2(V_{bi}-V)}{e\varepsilon_0\varepsilon_r N_i}$$

(1)

where $C$ is the measured capacitance, $V$ is the applied voltage, $V_{bi}$ is the built-in voltage, $e$ is the elementary charge, $\varepsilon_0$ is the vacuum permittivity, $\varepsilon_r$ is the dielectric constant of perovskite material, and $N_i$ is the intrinsic carrier density. By fitting equation (1) in the Mott-Schottky plot (Figure 5.13b), the built-in potential ($V_{bi}$) and intrinsic carrier density ($N_i$) are extracted. The $V_{bi}$ extracted for the FASnI$_3$ + SnF$_2$, FASnI$_3$ + SnCl$_2$, and FASnI$_3$ + SnBr$_2$ devices is 0.63, 0.54, and 0.47 V, respectively. The calculated $N_i$ of FASnI$_3$ + SnF$_2$, FASnI$_3$ + SnCl$_2$, and FASnI$_3$ + SnBr$_2$ devices is $9.05 \times 10^{15}$, $1.38 \times 10^{16}$, and $1.11 \times 10^{16}$ cm$^{-3}$, respectively, which are comparable to the literature values determined by capacitance and Hall measurements.[128, 130, 144-146] The lower $N_i$ of FASnI$_3$ + SnF$_2$ relative to with SnCl$_2$ and SnBr$_2$ supports that the formation of Sn$^{4+}$ is most suppressed, leading to less background carriers (holes) and lower defect densities, which agrees with the UPS and XPS measurements. Dark J-V measurements (Figure 5.14) also support the decreased hole density, with decreased dark current densities for FASnI$_3$ + SnF$_2$ compared to with other SnX$_2$ additives. The higher $V_{bi}$ and decreased $N_i$ of FASnI$_3$ + SnF$_2$ device is expected to lead to better charge extraction and decreased charge carrier recombination, which is consistent with the enhanced $J_{SC}$, $V_{OC}$, and FF.

Thermal admittance spectroscopy was carried out to determine the activation energy ($E_a$) for ion migration in the devices, as shown in Figure 5.5. Notably, we attribute the TAS signals to ionic migration as opposed to electronic trapping and detrapping based

on recent work with Pb-HPs performed by the Deibel group.[147] The emission rate is directly related to the applied frequency ($f$), and $E_a$ is calculated from the slope of the Arrhenius plot (details are included in the SI). For the pristine $FASnI_3$ device (Figure 5.5a and b, Figure 5.16a), two ionic defect species with $E_{a1}$ of 1.05 eV and $E_{a2}$ of 0.24 eV are determined. In the case of the $FASnI_3$ + $SnF_2$ device (Figure 5.5 c and d, Figure 5.16b), $E_a$ is increased to 1.33 eV, indicating that ionic migration will be decreased during device operation. We find a similar $E_a$ of 1.29 eV for $FASnI_3$ + $SnCl_2$ (Figure 5.17). In contrast, the lowest $E_a$ of 0.79 eV is found for $FASnI_3$ + $SnBr_2$ (Figure 5.18).

Insight into the nature of the defects can be inferred from previous computational results.[123, 148] Here, $V_{Sn}$ is the dominant defect (*i.e.*, it has the lowest formation energy) under Sn-poor conditions and $V_I$ has the lowest formation energy under Sn-rich conditions.[148] It is reported that the energy barrier for migration of $V_{Sn}$ and $V_I$ is 2.40 eV and <0.60 eV, respectively.[39, 149] Our TAS measurements, with an $E_{a1}$ of 1.05 eV and $E_{a2}$ of 0.24 eV, are approximately half of these calculated values and are tentatively attributed to $V_{Sn}$ and $V_I$, respectively. X-ray photoemission spectroscopy indicates that the $FASnI_3$ film with no additive is Sn deficient, with a N:Sn:I ratio of 2.2:1:3.4 (Table 5.5); however, when $SnF_2$ is added the stoichiometry becomes nearly ideal at 2.0:1:2.9. The $V_{Sn}$ concentration should therefore decrease upon addition of $SnF_2$. The $E_a$ for $V_{Sn}$ in the $FASnI_3$ + $SnF_2$ sample increases to 1.33 eV. A similar stoichiometry is observed with $SnCl_2$, and a similarly high $E_a$ is also observed. On the other hand, the $E_a$ with $SnBr_2$ is reduced to even less than pristine $FASnI_3$, even though the stoichiometry is closer to ideal (2.1:1:3.1) than pristine $FASnI_3$.
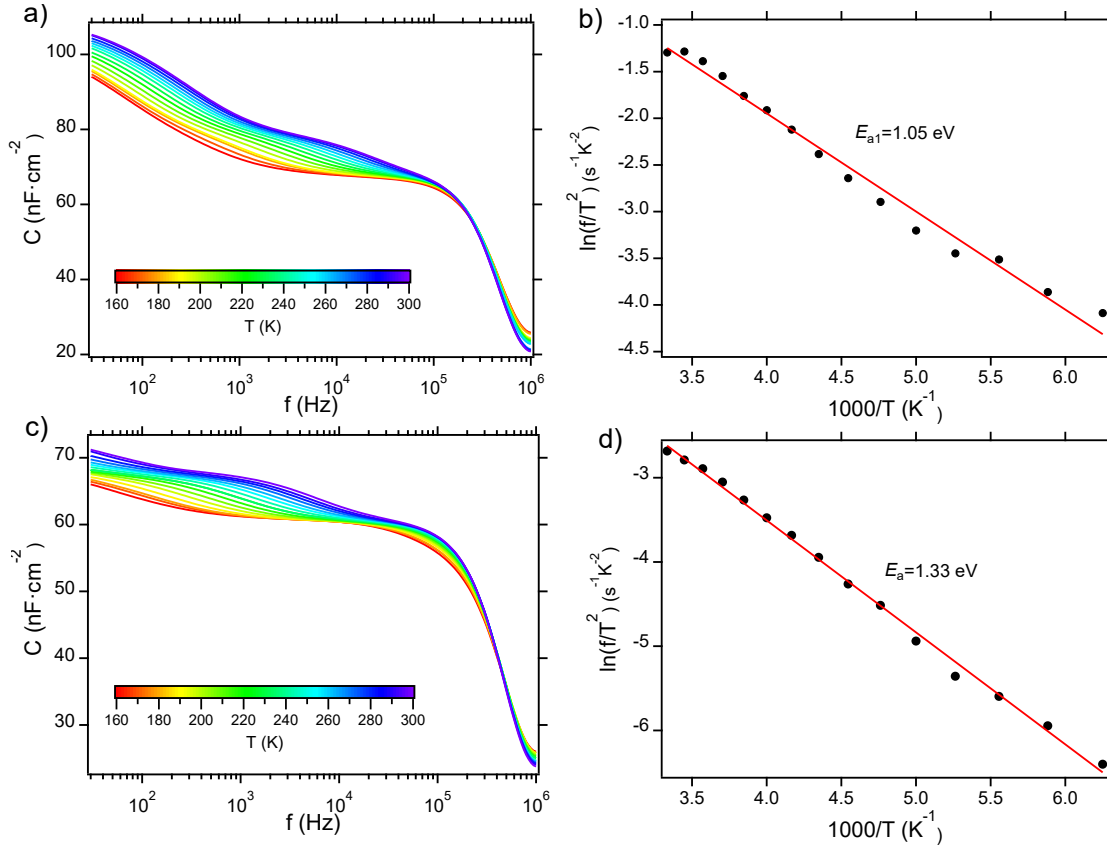
Figure 5.5 Capacitance-frequency (C-f) plots from TAS measurements a) FASnI$_3$ and c) FASnI$_3$ + SnF$_2$ devices carried out under dark conditions between 160 and 300 K at 0 V DC bias with an AC bias amplitude of 10 mV. Activation energy ($E_a$) of the ionic defects of b) FASnI$_3$ and d) FASnI$_3$ + SnF$_2$ devices extracted from Arrhenius plots of the characteristic peak frequency, obtained from the differential capacitance (-f.dC/df ) at various temperatures.

## 5.4    Conclusion

In summary, the work presented here identifies the role of SnX$_2$ additives on electronic and ionic defects in FASnI$_3$ perovskite solar cells. The beneficial role of the SnF$_2$ additive in FASnI$_3$ can be attributed to improved morphology, less energetic disorder, and decreased Sn$^{4+}$ associated defects in the film, whereas these benefits are significantly decreased with SnCl$_2$ and SnBr$_2$ additives. Here, the formation of SnF$_4$ through the halide exchange reaction with SnI$_4$ prevents the insertion of Sn$^{4+}$ into the crystal lattice, which

retards the self p-type doping and decreases the background hole density and dark current. Moreover, the activation energy of ion migration increases upon $SnF_2$ addition, which could be attributed to the strong Sn-F bond and its effect on passivating grain boundaries as well as the decreased concentration of $Sn^{4+}$. Consequently, the photovoltaic performance of $FASnI_3 + SnF_2$ is significantly improved relative to the control and the other $SnX_2$ additives.

## 5.5 Additional Figures and Tables
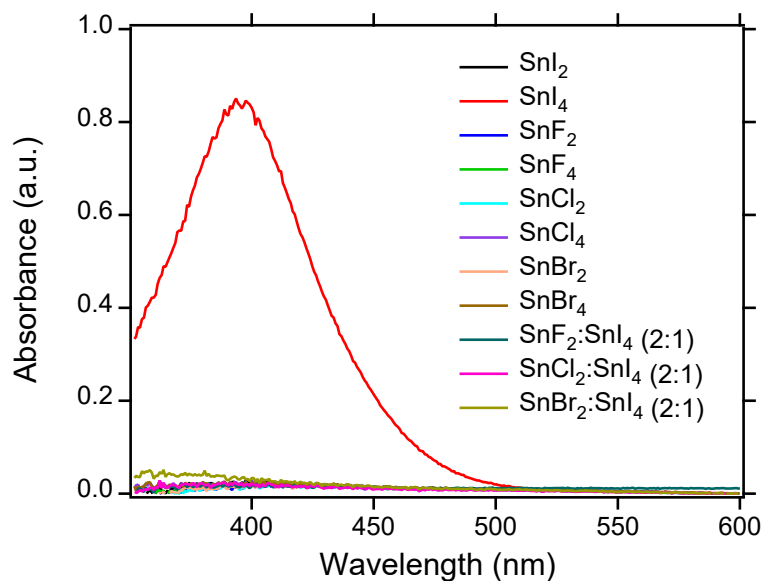


Figure 5.6 Solution absorbance of different Sn species, and a mixture of $SnI_4$ with $SnF_2$, $SnCl_2$, and $SnBr_2$ (1 to 2 mole ratio), respectively. The total solution concentration is kept at 1.0 mM in DMSO.
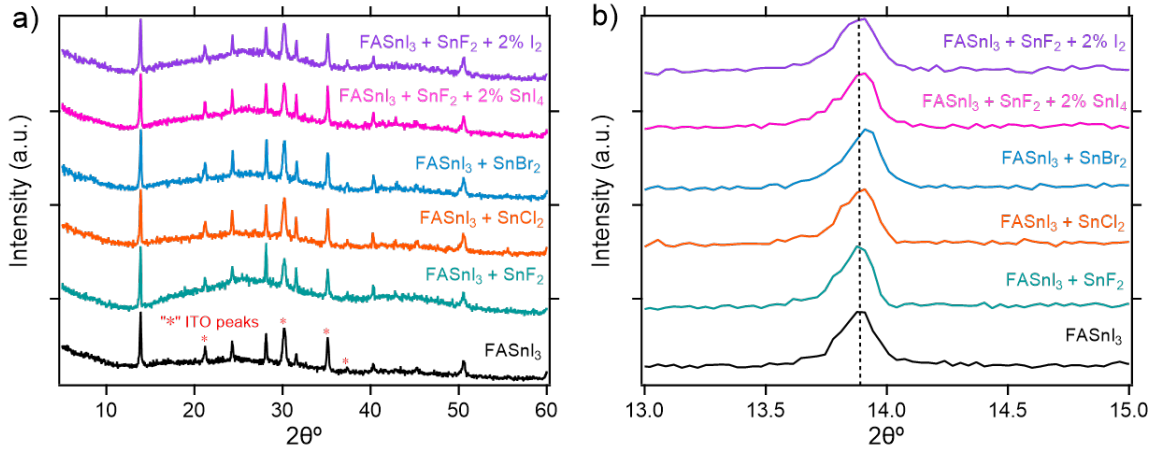
Figure 5.7 a) XRD patterns and b) (001) plane peaks of $FASnI_3$, $FASnI_3 + SnF_2$, $FASnI_3 + SnCl_2$, $FASnI_3 + SnBr_2$, $FASnI_3 + SnF_2 + 2\%$ $SnI_4$, and $FASnI_3 + SnF_2 + 2\%$ $I_2$ films.
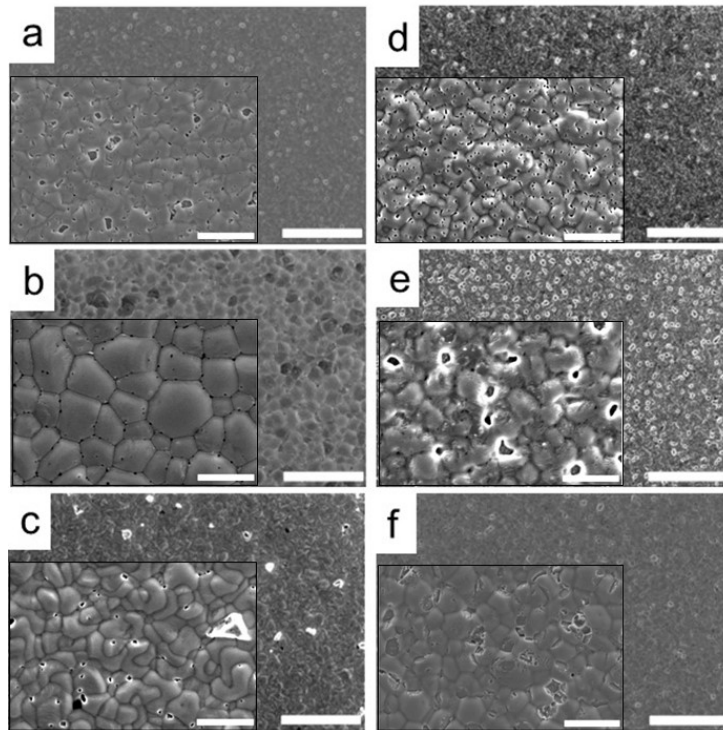


Figure 5.8 SEM images of a) $FASnI_3$, b) $FASnI_3 + SnF_2$, c) $FASnI_3 + SnCl_2$, d) $FASnI_3 + SnBr_2$, e) $FASnI_3 + SnF_2 + 2\%$ $SnI_4$, and f) $FASnI_3 + SnF_2 + 2\%$ $I_2$ films. Scale bar is 5 μm. Inset image has 1 μm scale bar.
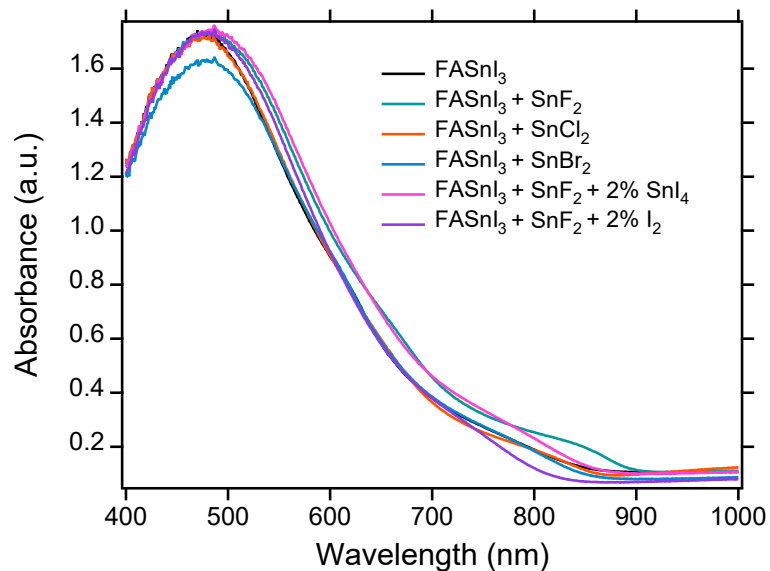
Figure 5.9 Absorbance spectra of FASnI₃, FASnI₃ + SnF₂, FASnI₃ + SnCl₂, FASnI₃ + SnBr₂, FASnI₃ + SnF₂ + 2% SnI₄, FASnI₃ + SnF₂ + 2% I₂ films.
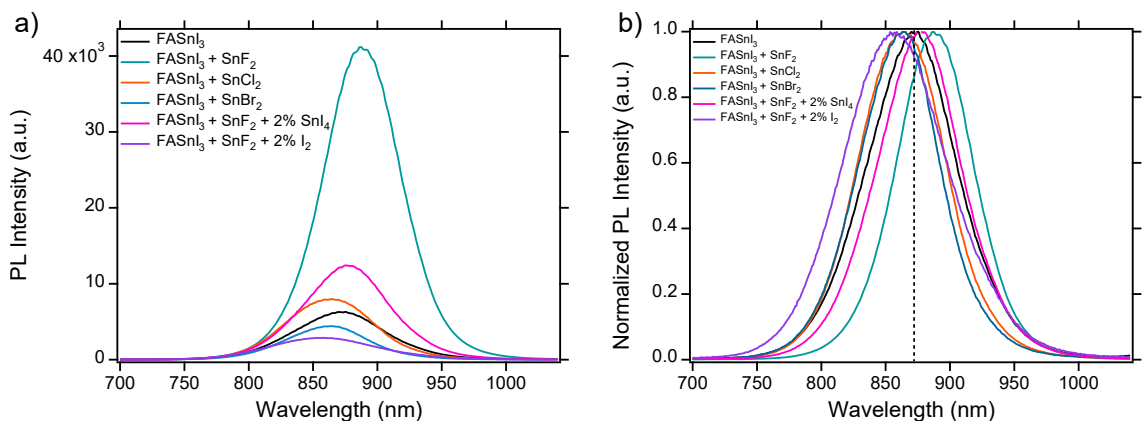


Figure 5.10 a) Raw photoluminescence (PL) and b) normalized PL spectra of FASnI₃, FASnI₃ + SnF₂, FASnI₃ + SnCl₂, FASnI₃ + SnBr₂, FASnI₃ + SnF₂ + 2% SnI₄, FASnI₃ + SnF₂ + 2% I₂ films.
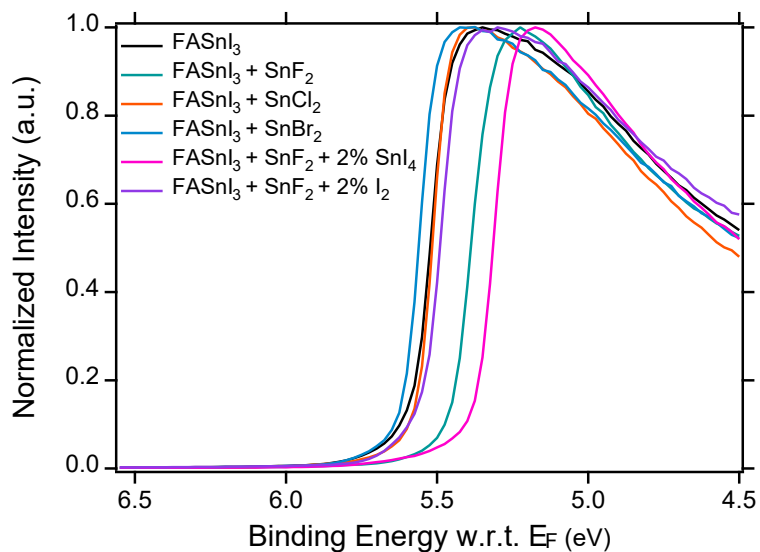
Figure 5.11 UPS spectra of the secondary electron cut-off (SECO) region for FASnI$_3$, FASnI$_3$ + SnF$_2$, FASnI$_3$ + SnCl$_2$, FASnI$_3$ + SnBr$_2$, FASnI$_3$ + SnF$_2$ + 2% SnI$_4$, FASnI$_3$ + SnF$_2$ + 2% I$_2$ films. The work function (WF) of the respective films is calculated by subtracting the SECO energy from the excitation energy (10.2 eV).

Table 5.2 Work function (WF) vs. Ionization energy (IE)

| Samples | WF (eV) | IE (eV) |
|---|---|---|
| FASnI$_3$ | 4.60 | 4.69 |
| FASnI$_3$ + SnF$_2$ | 4.73 | 5.05 |
| FASnI$_3$ + SnCl$_2$ | 4.62 | 4.86 |
| FASnI$_3$ + SnBr$_2$ | 4.57 | 4.73 |
| FASnI$_3$ + SnF$_2$ + 2% SnI$_4$ | 4.81 | 4.93 |
| FASnI$_3$ + SnF$_2$ + 2% I$_2$ | 4.63 | 4.73 |
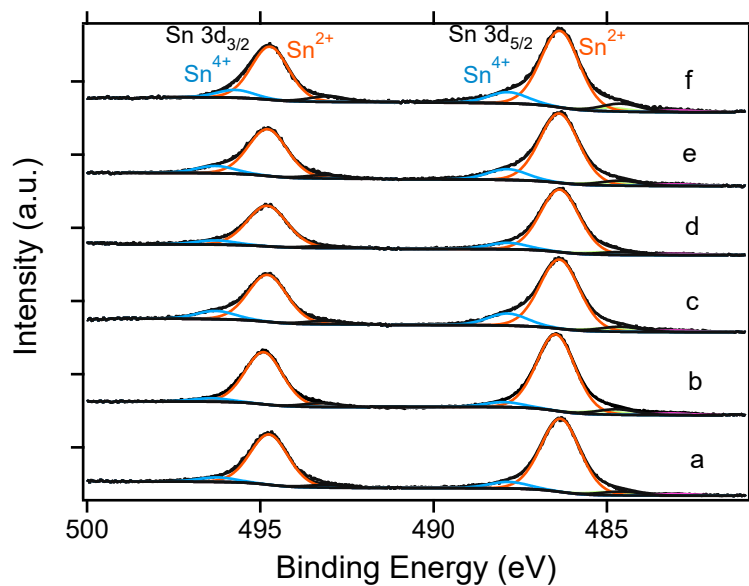
Figure 5.12 XPS spectra of the Sn 3d regions fitted to the $Sn^{2+}$ and $Sn^{4+}$ peaks for a) $FASnI_3$, b) $FASnI_3 + SnF_2$, c) $FASnI_3 + SnCl_2$, d) $FASnI_3 + SnBr_2$, e) $FASnI_3 + SnF_2 + 2\%$ $SnI_4$, and f) $FASnI_3 + SnF_2 + 2\%$ $I_2$ films.

Table 5.3 Percentage of $Sn^{2+}$ and $Sn^{4+}$

| Samples | %$Sn^{2+}$ | %$Sn^{4+}$ |
|---|---|---|
| $FASnI_3$ | 91.8 | 8.2 |
| $FASnI_3 + SnF_2$ | 93.9 | 6.1 |
| $FASnI_3 + SnCl_2$ | 85.1 | 14.9 |
| $FASnI_3 + SnBr_2$ | 90.6 | 9.4 |
| $FASnI_3 + SnF_2 + 2\%$ $SnI_4$ | 86.5 | 13.5 |
| $FASnI_3 + SnF_2 + 2\%$ $I_2$ | 87.2 | 12.8 |

Table 5.4 Atomic ratios determined by XPS.

| Samples | $N:Sn^{2+}:I$ |
|---|---|
| $FASnI_3$ | 2.6:1:3.9 |
| $FASnI_3 + SnF_2$ | 2.3:1:3.3 |
| $FASnI_3 + SnCl_2$ | 2.5:1:3.4 |
| $FASnI_3 + SnBr_2$ | 2.4:1:3.6 |
| $FASnI_3 + SnF_2 + 2\% SnI_4$ | 2.3:1:3.6 |
| $FASnI_3 + SnF_2 + 2\% I_2$ | 2.7:1:3.7 |

Table 5.5 Atomic ratios determined by XPS.

| Samples | N:Total Sn:I |
|---|---|
| $FASnI_3$ | 2.2:1:3.4 |
| $FASnI_3 + SnF_2$ | 2.0:1:2.9 |
| $FASnI_3 + SnCl_2$ | 2.0:1:2.7 |
| $FASnI_3 + SnBr_2$ | 2.1:1:3.1 |
| $FASnI_3 + SnF_2 + 2\% SnI_4$ | 1.9:1:2.9 |
| $FASnI_3 + SnF_2 + 2\% I_2$ | 2.2:1:3.0 |
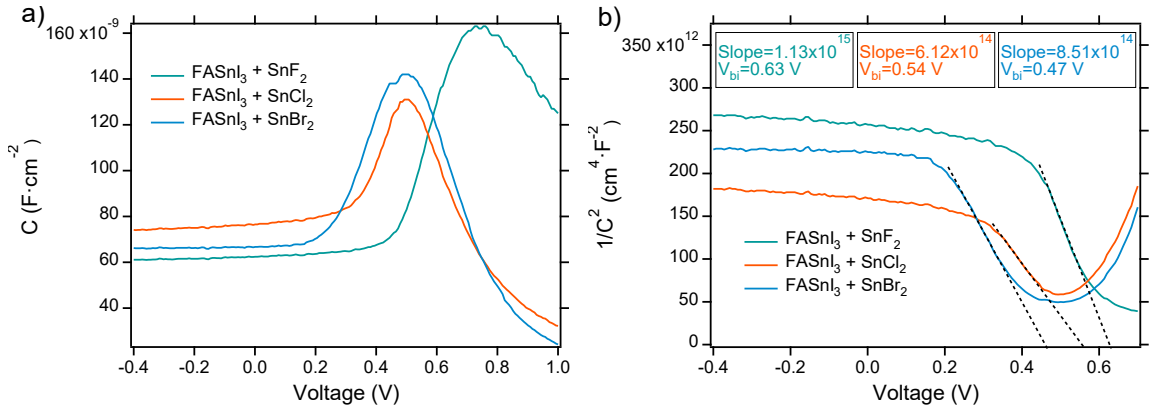
Figure 5.13 a) Capacitance-voltage (C-V) plots and b) Mott-Schottky plots of FASnI$_3$ + SnF$_2$, FASnI$_3$ + SnCl$_2$, and FASnI$_3$ + SnBr$_2$ devices.
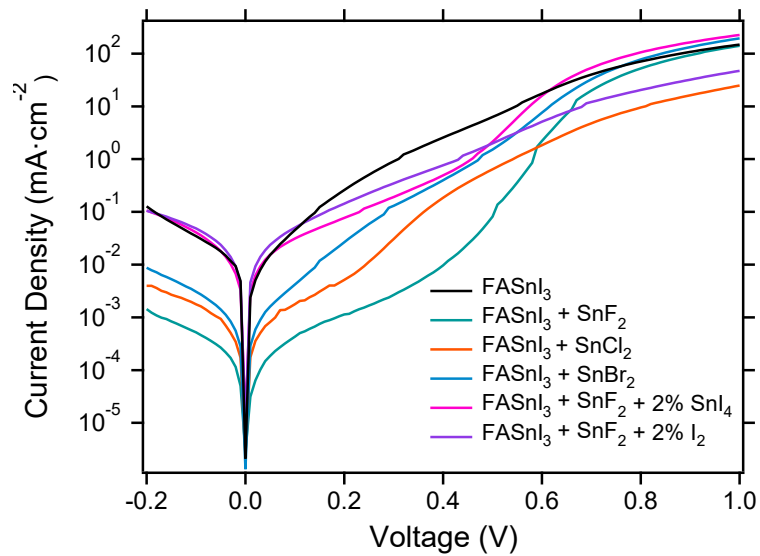


Figure 5.14 Dark current density-voltage (*J-V*) plots of FASnI$_3$, FASnI$_3$ + SnF$_2$, FASnI$_3$ + SnCl$_2$, FASnI$_3$ + SnBr$_2$, FASnI$_3$ + SnF$_2$ + 2% SnI$_4$, and FASnI$_3$ + SnF$_2$ + 2% I$_2$ devices.
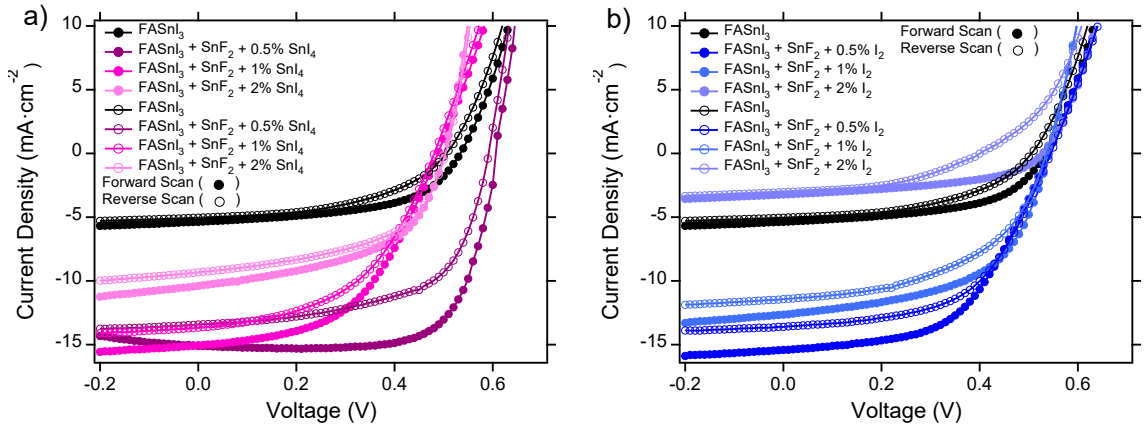
Figure 5.15 Illuminated current density-voltage ($J$-$V$) plots of a) FASnI$_3$, FASnI$_3$ + SnF$_2$ + 0.5% SnI$_4$, FASnI$_3$ + SnF$_2$ + 1% SnI$_4$, FASnI$_3$ + SnF$_2$ + 2% SnI$_4$ and b) FASnI$_3$, FASnI$_3$ + SnF$_2$ + 0.5% I$_2$, FASnI$_3$ + SnF$_2$ + 1% I$_2$, FASnI$_3$ + SnF$_2$ + 2% I$_2$ devices.

Table 5.6 Photovoltaic performance

| Samples | | $J_{SC}$ (mA·cm$^{-2}$) | $V_{OC}$ (V) | FF | PCE (%) |
|---|---|---|---|---|---|
| FASnI$_3$+SnF$_2$+ 0.5% SnI$_4$ | Average* | 14.1±1.2 | 0.604±0.0189 | 0.633±0.055 | 5.40±0.63 |
| FASnI$_3$+SnF$_2$+ 1% SnI$_4$ | Average | 11.5±1.5 | 0.500±0.015 | 0.490±0.026 | 2.83±0.33 |
| FASnI$_3$+SnF$_2$+ 2% SnI$_4$ | Average | 7.83±1.08 | 0.374±0.112 | 0.435±0.071 | 1.32±0.59 |
| FASnI$_3$+SnF$_2$+ 0.5% I$_2$ | Average | 11.6±1.7 | 0.528±0.021 | 0.490±0.037 | 3.00±0.55 |
| FASnI$_3$+SnF$_2$+ 1% I$_2$ | Average | 9.36±1.71 | 0.511±0.066 | 0.503±0.053 | 2.47±0.80 |
| FASnI$_3$+SnF$_2$+ 2% I$_2$ | Average | 2.06±1.44 | 0.375±0.139 | 0.399±0.079 | 0.384±0.374 |

*Average value is calculated from the forward and reverse scans of 20 devices.
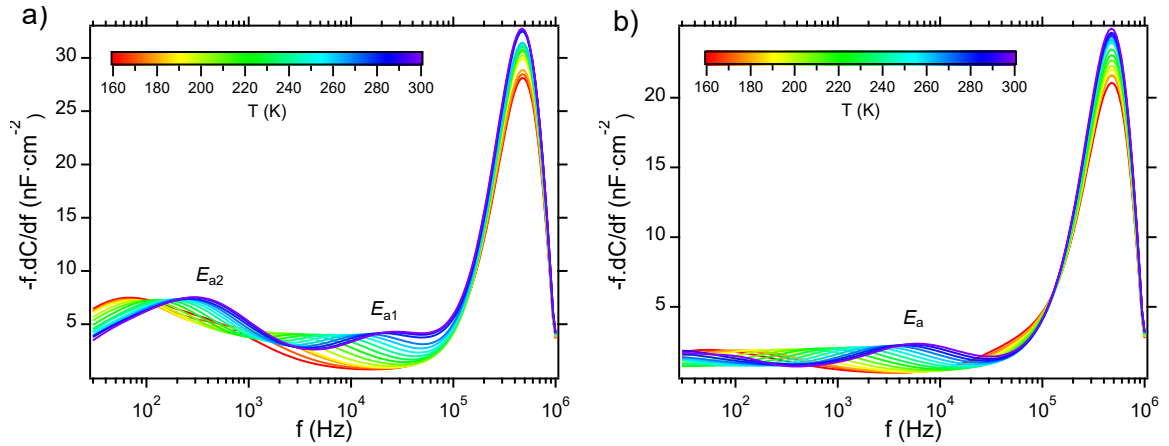
Figure 5.16 The derivative of capacitance (C) with respect to the frequency (f) *i.e.,* -f.dC/df at various temperatures for a) FASnI$_3$ and b) FASnI$_3$ + SnF$_2$ devices.
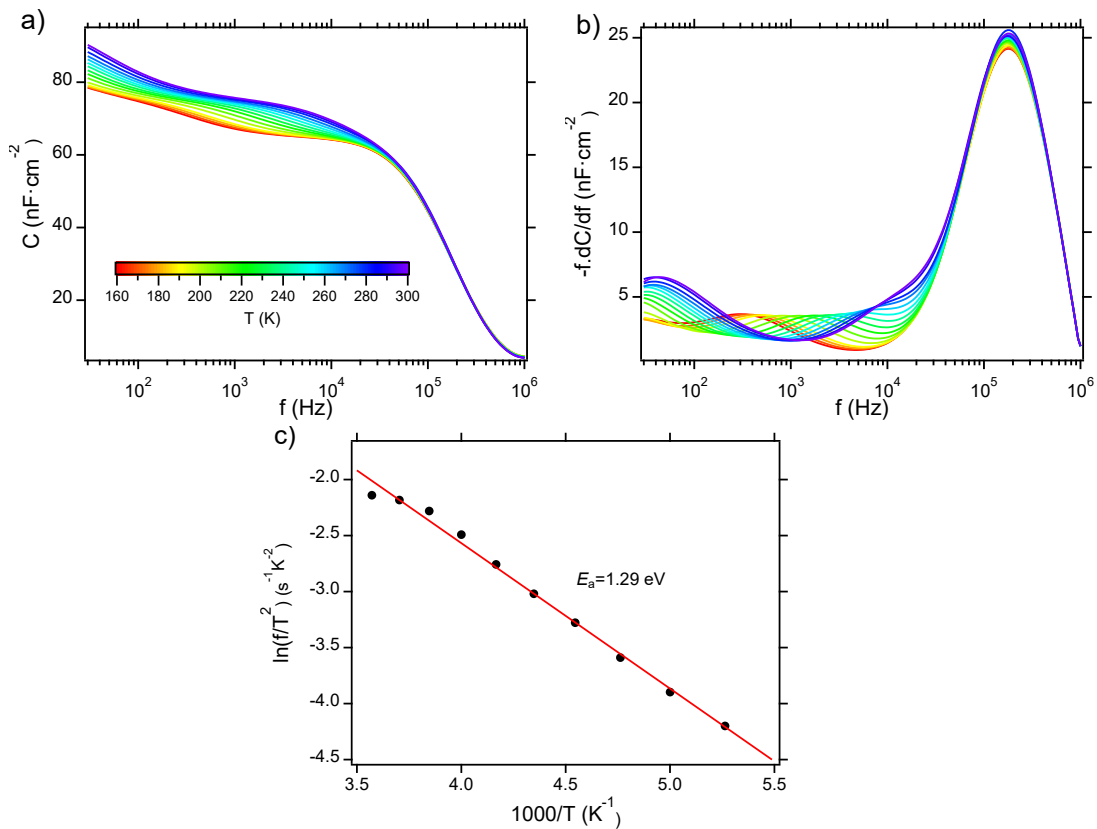


Figure 5.17 TAS measurement of FASnI$_3$ + SnCl$_2$ device. a) C-f plot, b) differential capacitance (-f.dC/df) plot, and c) Arrhenius plot.
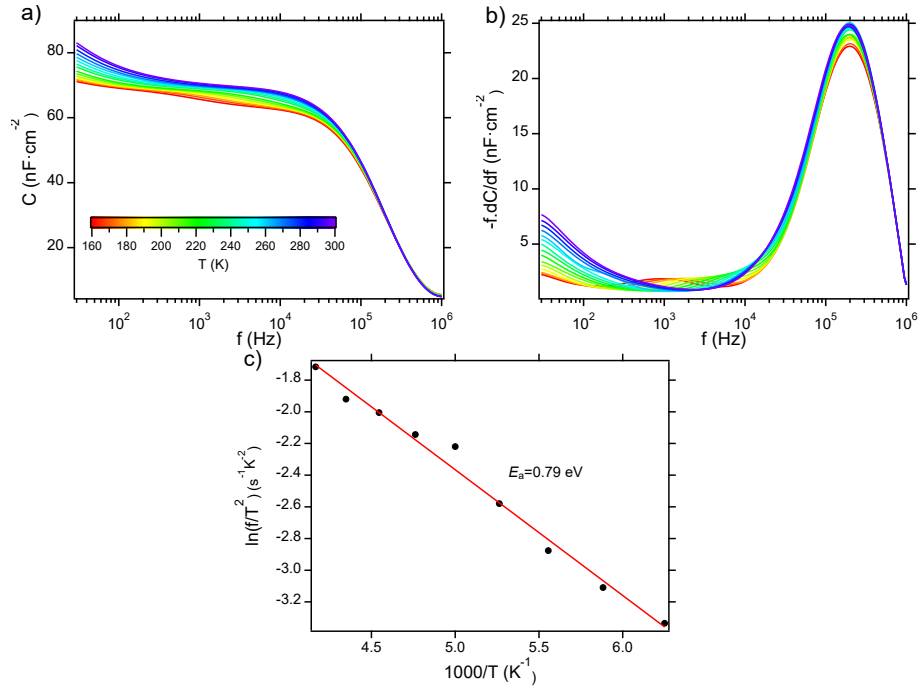
Figure 5.18 TAS measurement of FASnI$_3$ + SnBr$_2$ device. a) C-f plot, b) differential capacitance (-f.dC/df) plot, and c) Arrhenius plot.
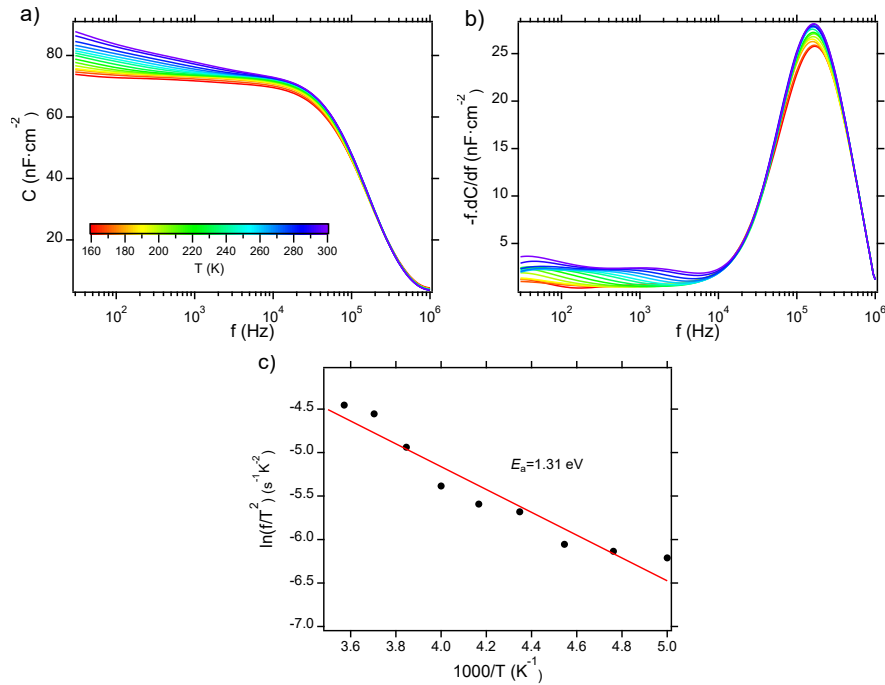


Figure 5.19 TAS measurement of FASnI$_3$ + SnF$_2$ + 2% SnI$_4$ device. a) C-f plot, b) differential capacitance (-f.dC/df) plot, and c) Arrhenius plot.
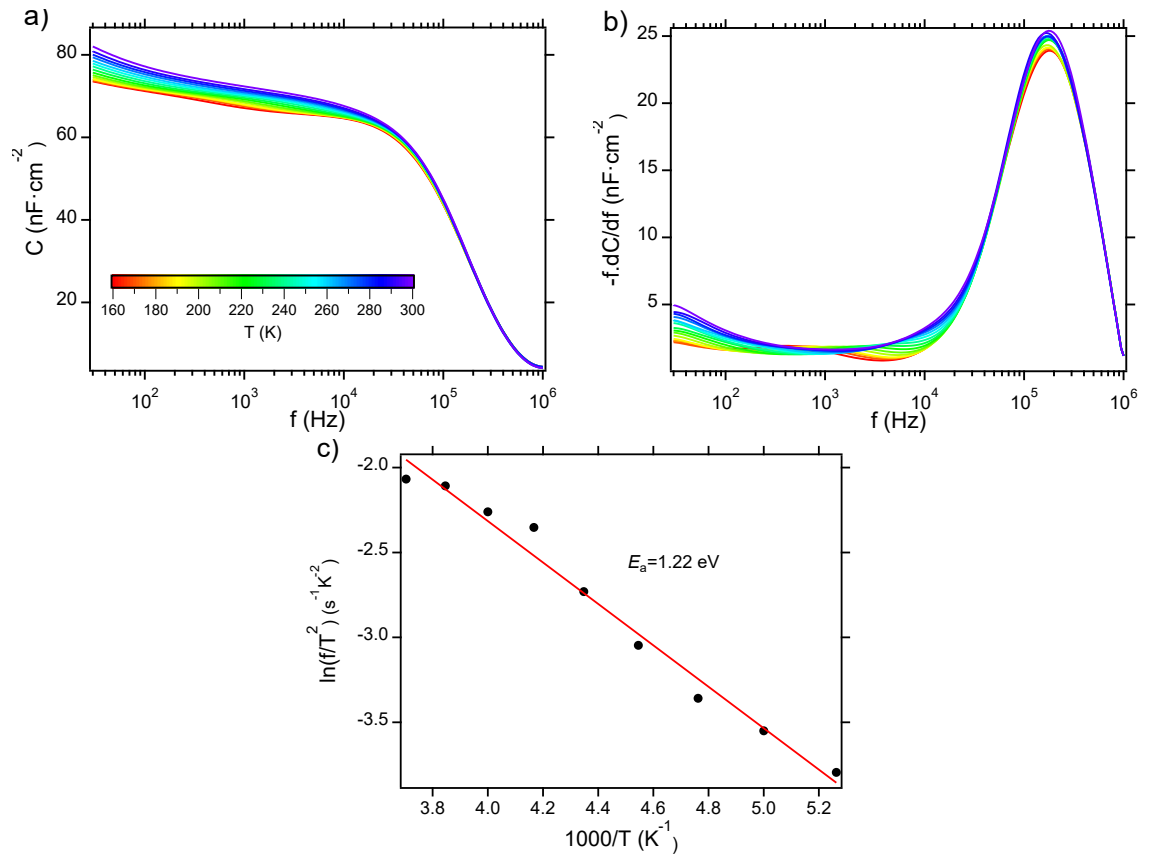
Figure 5.20 TAS measurement of FASnI$_3$ + SnF$_2$ + 2% I$_2$ device. a) C-f plot, b) differential capacitance (-f.dC/df) plot, and c) Arrhenius plot.

CHAPTER 6. SUMMARY AND PERSPECTIVES

In this Ph.D. work, I have endeavored to work with promising halide perovskite semiconductors, especially tin-based perovskites. This thesis is centered on understanding additives role in further development of tin halide perovskites photovoltaics. To do so, we have first studied the fundamental chemistry of additives and how they work in tin perovskite precursor solution as well as thin films to retard $Sn^{2+}$ oxidation and mitigate $Sn^{4+}$ concentration. This study serves as a template to design and develop new additives to stabilize tin halide perovskites.

After that, we investigated the different $SnX_2$ additives (X=F, Cl, Br) impact on morphology, electronic and ionic defect properties, and photovoltaic performance of $FASnI_3$ perovskites. It was uncovered that $SnF_2$ incorporation into $FASnI_3$ precursor shows better morphology and less electronic defects of the film, and increases photovoltaic performance and activation energy of ion migration of the device as compared to the $SnCl_2$ and $SnBr_2$ additives. This study provides insight into the reason why $SnF_2$ is a universally used additive in processing tin perovskite solar cells.

Furthermore, we set up TAS instrument to characterize the ionic defect properties of tin halide perovskite photovoltaics. By using this technique, activation energy of ion migration was determined. It was found that pristine $FASnI_3$ photovoltaic device shows more migration of ionic defects species than the $SnF_2$-added $FASnI_3$ device.

Despite tremendous efforts done by research community, the efficiency and stability of Sn perovskite photovoltaics still lags their Pb-analogs. To further advance this field, efforts such as designing new additives, finding alternative charge transporting

materials, understanding and controlling crystallization dynamics, digging more into the origin and mitigation of defects are to be investigated. Altogether, this dissertation work has provided insights into the importance of understanding of processing additives role in tin halide perovskites. We have done systemic studies to get the fundamental understanding of additives function so as to improve the stability of tin perovskites. We hope these efforts will help researchers in the field of perovskite research to further develop this material and its photovoltaic device, so that the dream of commercialization of perovskite photovoltaics comes into reality sooner than late

REFERENCES

(1) Haegel, N. M.; Kurtz, S. R. Global Progress Toward Renewable Electricity: Tracking the Role of Solar (Version 3). *IEEE J. Photovolt.* **2023**, *13* (6), 768-776.

(2) Nijsse, F.; Mercure, J. F.; Ameli, N.; Larosa, F.; Kothari, S.; Rickman, J.; Vercoulen, P.; Pollitt, H. The momentum of the Solar Energy Transition. *Nat. Comm.* **2023**, *14* (1), 6542.

(3) Fritts, C. E. On the Fritts Selenium Cell and Batteries. *J. Frank. Inst.* **1885**, 221-232.

(4) Chapin, D. M.; Fuller, C. S.; Pearson, G. L. A New Silicon p-n Junction Photocell for Converting Solar Radiation into Electrical Power. *J. Appl. Phys.* **1954**, *25* (5), 676-677.

(5) Dambhare, M. V.; Butey, B.; Moharil, S. V. Solar Photovoltaic Technology: A Review of Different Types of Solar Cells and its Future Trends. *J Phys.* **2021**, *1913*, 012053.

(6) Bagher, A. M.; Vahid, M. M. A.; Mohsen, M. Types of Solar Cells and Application. *Am. J. Opt. Phot.* **2015**, *3* (5).

(7) National Renewable Energy Laboratory Best Research-Cell Efficiencies. https://www.nrel.gov/pv/assets/pdfs/best-research-cell-efficiencies.pdf (accessed on April 2024).

(8) Yan, J.; Saunders, B. R. Third-Generation Solar Cells: A Review and Comparison of Polymer:Fullerene, Hybrid Polymer and Perovskite Solar Cells. *RSC Adv.* **2014**, *4* (82), 43286-43314.

(9) Sharif, R.; Khalid, A.; Ahmad, S. W.; Rehman, A.; Qutab, H. G.; Akhtar, H. H.; Mahmood, K.; Afzal, S.; Saleem, F. A Comprehensive Review of the Current Progresses and Material Advances in Perovskite Solar Cells. *Nanoscale Adv.* **2023**, *5* (15), 3803-3833.

(10) Correa-Baena, J.-P.; Abate, A.; Saliba, M.; Tress, W.; Jesper Jacobsson, T.; Grätzel, M.; Hagfeldt, A. The Rapid Evolution of Highly Efficient Perovskite Solar Cells. *Energy Environ. Sci.* **2017**, *10* (3), 710-727.

(11) Yi, Z.; Ladi, N. H.; Shai, X.; Li, H.; Shen, Y.; Wang, M. Will Organic-Inorganic Hybrid Halide Lead Perovskites Be Eliminated from Optoelectronic Applications? *Nanoscale Adv.* **2019**, *1* (4), 1276-1289.

(12) Goldschmidt, V. M. Die gesetze der krystallochemie. *Naturwissenschaften* **1926**, *14* (21), 477-485.

(13) Travis, W.; Glover, E. N. K.; Bronstein, H.; Scanlon, D. O.; Palgrave, R. G. On the Application of the Tolerance Factor to Inorganic and Hybrid Halide Perovskites: A Revised System. *Chem. Sci.* **2016**, *7* (7), 4548-4556.

(14) Fu, Y.; Hautzinger, M. P.; Luo, Z.; Wang, F.; Pan, D.; Aristov, M. M.; Guzei, I. A.; Pan, A.; Zhu, X.; Jin, S. Incorporating Large A Cations into Lead Iodide Perovskite Cages: Relaxed Goldschmidt Tolerance Factor and Impact on Exciton-Phonon Interaction. *ACS Cent. Sci.* **2019**, *5* (8), 1377-1386.

(15) Li, Z.; Yang, M.; Park, J.-S.; Wei, S.-H.; Berry, J. J.; Zhu, K. Stabilizing Perovskite Structures by Tuning Tolerance Factor: Formation of Formamidinium and Cesium Lead Iodide Solid-State Alloys. *Chem. Mater.* **2015**, *28* (1), 284-292.

(16) Mitzi, D. B. Introduction: Perovskites. *Chem. Rev.* **2019**, *119*, 3033-3035.

(17) Kojima, A.; Teshima, K.; Shirai, Y.; Miyasaka, T. Organometal Halide Perovskites as Visible-Light Sensitizers for Photovoltaic Cells. *J. Am. Chem. Soc.* **2009**, *131* (17), 6050-6051.

(18) Chung, I.; Lee, B.; He, J.; Chang, R. P.; Kanatzidis, M. G. All-Solid-State Dye-Sensitized Solar Cells with High Efficiency. *Nature* **2012**, *485* (7399), 486-489.

(19) Yu, Y.; Xia, J.; Liang, Y. Basic Understanding of Perovskite Solar Cells and Passivation Mechanism. *AIP Adv.* **2022**, *12* (5), 055307.

(20) Liu, T.; Scheidt, R. A.; Zheng, X.; Joy, S.; Jiang, Q.; Atapattu, H. R.; Chen, M.; Pruett, H.; Zhu, K.; Luther, J. M.; et al. Tuning Interfacial Energetics with Surface Ligands to Enhance Perovskite Solar Cell Performance. *Cell Reports Phys. Sci.* **2023**, *4* (11).

(21) Zhong, Y.; Munir, R.; Li, J.; Tang, M.-C.; Niazi, M. R.; Smilgies, D.-M.; Zhao, K.; Amassian, A. Blade-Coated Hybrid Perovskite Solar Cells with Efficiency >17%: An In Situ Investigation. *ACS Energy Lett.* **2018**, *3* (5), 1078-1085.

(22) Whitaker, J. B.; Kim, D. H.; Larson, Bryon W.; Zhang, F.; Berry, J. J.; van Hest, M. F. A. M.; Zhu, K. Scalable Slot-Die Coating of High Performance Perovskite Solar Cells. *Sustainable Energy Fuels* **2018**, *2* (11), 2442-2449.

(23) Uličná, S.; Dou, B.; Kim, D. H.; Zhu, K.; Walls, J. M.; Bowers, J. W.; van Hest, M. F. A. M. Scalable Deposition of High-Efficiency Perovskite Solar Cells by Spray-Coating. *ACS Appl. Energy Mater.* **2018**, *1* (5), 1853-1857.

(24) Li, Z.; Li, P.; Chen, G.; Cheng, Y.; Pi, X.; Yu, X.; Yang, D.; Han, L.; Zhang, Y.; Song, Y. Ink Engineering of Inkjet Printing Perovskite. *ACS Appl. Mater. Interfaces* **2020**, *12* (35), 39082-39091.

(25) Mei, A.; Li, X.; Liu, L.; Ku, Z.; Liu, T.; Rong, Y.; Xu, M.; Hu, M.; Chen, J.; Yang, Y.; et al. A Hole-Conductor-Free, Fully Printable Mesoscopic Perovskite Solar Cell with High Stability. *Science* **2014**, *345* (6194), 295-298.

(26) Yan, J.; Savenije, T. J.; Mazzarella, L.; Isabella, O. Progress and Challenges on Scaling up of Perovskite Solar Cell Technology. *Sustainable Energy & Fuels* **2022**, *6* (2), 243-266.

(27) Park, N.-G.; Zhu, K. Scalable Fabrication and Coating Methods for Perovskite Solar Cells and Solar Modules. *Nat. Rev. Mater.* **2020**, *5* (5), 333-350.

(28) Lee, J.-W.; Dai, Z.; Lee, C.; Lee, H. M.; Han, T.-H.; Marco, N. D.; Lin, O.; Choi, C. S.; Dunn, B.; Koh, J.; et al. Tuning Molecular Interactions for Highly Reproducible and Efficient Formamidinium Perovskite Solar Cells via Adduct Approach. *J. Am. Chem. Soc.* **2018**, *140* (20), 6317-6324.

(29) Wu, Z.; Bi, E.; Li, C.; Chen, L.; Song, Z.; Yan, Y. Scalable Two-Step Production of High-Efficiency Perovskite Solar Cells and Modules. *Solar RRL* **2022**, *7* (1).

(30) Yan, J.; Qiu, W.; Wu, G.; Heremans, P.; Chen, H. Recent Progress in 2D/Quasi-2D Layered Metal Halide Perovskites for Solar Cells. *J. Mater. Chem. A* **2018**, *6* (24), 11063-11077.

(31) Chen, X.; Zhou, H.; Wang, H. 2D/3D Halide Perovskites for Optoelectronic Devices. *Front. Chem.* **2021**, *9*, 715157.

(32) Ge, C.; Xue, Y. Z. B.; Li, L.; Tang, B.; Hu, H. Recent Progress in 2D/3D Multidimensional Metal Halide Perovskites Solar Cells. *Front. Mater.* **2020**, *7*.

(33) Smith, I. C.; Hoke, E. T.; Solis-Ibarra, D.; McGehee, M. D.; Karunadasa, H. I. A Layered Hybrid Perovskite Solar-Cell Absorber with Enhanced Moisture Stability. *Angew. Chem. Int. Ed. Engl.* **2014**, *53* (42), 11232-11235.

(34) Azmi, R.; Ugur, E.; Seitkhan, A.; Aljamaan, F.; Subbiah, A. S.; Liu, J.; Harrison, G. T.; Nugraha, M. I.; Eswaran, M. K.; Babics, M.; et al. Damp Heat–Stable Perovskite Solar Cells with Tailored-Dimensionality 2D-3D Heterojunctions. *Science* **2022**, *376* (6588), 73-77.

(35) Ball, J. M.; Petrozza, A. Defects in Perovskite-Halides and their Effects in Solar Cells. *Nat. Energy* **2016**, *1* (11), 16149.

(36) Kim, J.; Lee, S.-H.; Lee, J. H.; Hong, K.-H. The Role of Intrinsic Defects in Methylammonium Lead Iodide Perovskite. *J. Phys. Chem. Lett.* **2014**, *5* (8), 1294-1504.

(37) Chen, X.; Cheng, S.; Xiao, L.; Sun, H. Identifying, Understanding and Controlling Defects and Traps in Halide Perovskites for Optoelectronic Devices: A Review. *J. Phys. D: Appl. Phys.* **2020**, *53* (37).

(38) Li, W.; Liu, J.; Bai, F.-Q.; Zhang, H.-X.; Prezhdo, O. V. Hole Trapping by Iodine Interstitial Defects Decreases Free Carrier Losses in Perovskite Solar Cells_ A Time-Domain Ab Initio Study. *ACS Energy Lett.* **2017**, *2* (6), 1257-1478.

(39) Eames, C.; Frost, J. M.; Barnes, P. R.; O'Regan, B. C.; Walsh, A.; Islam, M. S. Ionic Transport in Hybrid Lead Iodide Perovskite Solar Cells. *Nat. Comm.* **2015**, *6*, 7497.

(40) Azpiroz, J. M.; Mosconi, E.; Bisquert, J.; Angelis, F. D. Defect Migration in Methylammonium Lead Iodide and its Role in Perovskite Solar Cell Operation. *Energy Environ. Sci.* **2015**, *8* (7), 2118-2127.

(41) Hailegnaw, B.; Kirmayer, S.; Edri, E.; Hodes, G.; Cahen, D. Rain on Methylammonium Lead Iodide Based Perovskites: Possible Environmental Effects of Perovskite Solar Cells. *J. Phys. Chem. Lett.* **2015**, *6* (9), 1543-1547.

(42) Li, J.; Cao, H. L.; Jiao, W. B.; Wang, Q.; Wei, M.; Cantone, I.; Lu, J.; Abate, A. Biological Impact of Lead from Halide Perovskites Reveals the Risk of Introducing a Safe Threshold. *Nat. Comm.* **2020**, *11* (1), 310.

(43) Infante, I.; Manna, L. Are There Good Alternatives to Lead Halide Perovskite Nanocrystals? *Nano Lett.* **2021**, *21*, 6-9.

(44) Vargas, B.; Rodríguez-López, G.; Solis-Ibarra, D. The Emergence of Halide Layered Double Perovskites. *ACS Energy Lett.* **2020**, *5* (11), 3591-3608.

(45) Shockley, W.; Queisser, H. J. Detailed Balance Limit of Efficiency of p-n Junction Solar Cells. *J. Appl. Phys.* **1961**, *32* (3), 510-519.

(46) Konstantakou, M.; Stergiopoulos, T. A Critical Review on Tin Halide Perovskite Solar Cells. *J. Mater. Chem. A* **2017**, *5* (23), 11518-11549.

(47) Noel, N. K.; Stranks, S. D.; Abate, A.; Wehrenfennig, C.; Guarnera, S.; Haghighirad, A.-A.; Sadhanala, A.; Eperon, G. E.; Pathak, S. K.; Johnston, M. B.; et al. Lead-Free Organic–Inorganic Tin Halide Perovskites for Photovoltaic Applications. *Energy Environ. Sci.* **2014**, *7* (9), 3061-3068.

(48) Hao, F.; Stoumpos, C. C.; Cao, D. H.; Chang, R. P. H.; Kanatzidis, M. G. Lead-Free Solid-State Organic–Inorganic Halide Perovskite Solar Cells. *Nat. Photon.* **2014**, *8* (6), 489-494.

(49) Yu, B. B.; Chen, Z.; Zhu, Y.; Wang, Y.; Han, B.; Chen, G.; Zhang, X.; Du, Z.; He, Z. Heterogeneous 2D/3D Tin-Halides Perovskite Solar Cells with Certified Conversion Efficiency Breaking 14%. *Adv. Mater.* **2021**, *33* (36), e2102055.

(50) Awais, M.; Kirsch, R. L.; Yeddu, V.; Saidaminov, M. I. Tin Halide Perovskites Going Forward: Frost Diagrams Offer Hints. *ACS Mater. Lett.* **2021**, *3* (3), 299-307.

(51) Johnson, W., Jr.; Bergfeld, W. F.; Belsito, D. V.; Hill, R. A.; Klaassen, C. D.; Liebler, D. C.; Marks, J. G., Jr.; Shank, R. C.; Slaga, T. J.; Snyder, P. W.; et al. Safety Assessment of Tin(IV) oxide as Used in Cosmetics. *Int. J. Toxicol.* **2014**, *33*, 40S-66S.

(52) Ledinsky, M.; Schonfeldova, T.; Holovsky, J.; Aydin, E.; Hajkova, Z.; Landova, L.; Neykova, N.; Fejfar, A.; Wolf, S. D. Temperature Dependence of the Urbach Energy in Lead Iodide Perovskites. *J. Phys. Chem. Lett.* **2019**, *10* (6), 1368-1373.

(53) Subedi, B. L., C.; Chen, C.; Liu, D.; Junda, M. M.; Song, Z.; Yan, Y.; Podraza, N. J. Urbach Energy and Open-Circuit Voltage Deficit for Mixed Anion–Cation Perovskite Solar Cells. *ACS Appl. Mater. Interfaces* **2022**, *14*, 7796-7804.

(54) Aalbers, G. J. W.; van der Pol, T. P. A.; Datta, K.; Remmerswaal, W. H. M.; Wienk, M. M.; Janssen, R. A. J. Effect of Sub-Bandgap Defects on Radiative and Non-Radiative Open-Circuit Voltage Losses in Perovskite Solar Cells. *Nat. Comm.* **2024**, *15* (1), 1276.

(55) Murphy, J. C.; Aamodt, L. C. Photothermal Spectroscopy using Optical Beam Probing: Mirage Effect. *J. Appl. Phys.* **1980**, *51* (9), 4580-4588.

(56) Kocha, N.; Pop, D.; Weber, R. L.; Bowering, N.; Winter, B.; Wick, M.; Leising, G.; Hertel, I. V.; Braun, W. Radiation Induced Degradation and Surface Charging of Organic Thin Films in Ultraviolet Photoemission Spectroscopy. *Thin Solid Films* **2001**, *391*, 81-87.

(57) Song, Q. L.; Wang, M. L.; Obbard, E. G.; Sun, X. Y.; Ding, X. M.; Hou, X. Y.; Li, C. M. Degradation of Small-Molecule Organic Solar Cells. *Appl. Phys. Lett.* **2006**, *89*, 251118.

(58) Boehm, A. M.; Wieser, J.; Butrouna, K.; Graham, K. R. A New Photon Source for Ultraviolet Photoelectron Spectroscopy of Organic and Other Damage-Prone Materials. *Org. Electronics* **2017**, *41*, 9-16.

(59) Endres, J.; Egger, D. A.; Kulbak, M.; Kerner, R. A.; Zhao, L.; Silver, S. H.; Hodes, G.; Rand, B. P.; Cahen, D.; Kronik, L.; et al. Valence and Conduction Band Densities of States of Metal Halide Perovskites: A Combined Experimental-Theoretical Study. *J. Phys. Chem. Lett.* **2016**, *7* (14), 2722-2729.

(60) Sakhatskyi, K.; John, R. A.; Guerrero, A.; Tsarev, S.; Sabisch, S.; Das, T.; Matt, G. J.; Yakunin, S.; Cherniukh, I.; Kotyrba, M.; et al. Assessing the Drawbacks and Benefits of Ion Migration in Lead Halide Perovskites. *ACS Energy Lett.* **2022**, *7*, 3401-3414.

(61) Liu, J.; Hu, M.; Dai, Z.; Que, W.; Padture, N. P.; Zhou, Y. Correlations between Electrochemical Ion Migration and Anomalous Device Behaviors in Perovskite Solar Cells. *ACS Energy Lett.* **2021**, *6* (6), 1003-1014.

(62) Walter, T.; Herberholz, R.; Müller, C.; Schock, H. W. Determination of Defect Distributions from Admittance Measurements and Application to Cu(In,Ga)Se$_2$ Based Heterojunctions. *J. Appl. Phys.* **1996**, *80* (8), 4411-4420.

(63) Kneisel, J.; Siemer, K.; Luck, I.; Bräunig, D. Admittance Spectroscopy of Efficient CuInS$_2$ Thin Film Solar Cells. *J. Appl. Phys.* **2000**, *88* (9), 5474-5481.

(64) Proskuryakov, Y. Y.; Durose, K.; Taele, B. M.; Welch, G. P. Admittance Spectroscopy of CdTe/CdS Solar Cells Subjected to Varied Nitric-Phosphoric Etching Conditions. *J. Appl. Phys.* **2007**, *101*, 0124505.

(65) Reichert, S.; An, Q.; Woo, Y. W.; Walsh, A.; Vaynzof, Y.; Deibel, C. Probing the Ionic Defect Landscape in Halide Perovskite Solar Cells. *Nat. Comm.* **2020**, *11* (1), 6098.

(66) Futscher, M. H.; Gangishetty, M. K.; Congreve, D. N.; Ehrler, B. Quantifying Mobile Ions and Electronic Defects in Perovskite-based Devices with Temperature-Dependent

Capacitance Measurements: Frequency vs Time Domain. *J. Chem. Phys.* **2020**, *152* (4), 044202.

(67) Muntasir, T.; Chaudhary, S. Defects in Solution-Processed Dithienylsilole-Based Small-Molecule Photovoltaic Thin-Films. *J. Appl. Phys.* **2016**, *119* (2), 025501.

(68) Muntasir, T.; Chaudhary, S. Understanding Defect Distributions in Polythiophenes Via Comparison of Regioregular and Regiorandom Species. *J. Appl. Phys.* **2015**, *118* (20), 205504.

(69) Wang, S.; Kaienburg, P.; Klingebiel, B.; Schillings, D.; Kirchartz, T. Understanding Thermal Admittance Spectroscopy in Low-Mobility Semiconductors. *J. Phys. Chem. C* **2018**, *122* (18), 9795-9803.

(70) Ni, Z.; Jiao, H.; Fei, C.; Gu, H.; Xu, S.; Yu, Z.; Yang, G.; Deng, Y.; Jiang, Q.; Liu, Y.; et al. Evolution of Defects During the Degradation of Metal Halide Perovskite Solar Cells under Reverse Bias and Illumination. *Nat. Energy* **2022**, *7* (1), 65-73.

(71) Kojima, A.; Teshima, K.; Shirai, Y.; Miyasaka, T. Organometal Halide Perovskites as Visible-Light Sensitizers for Photovoltaic Cells. *J. Am. Chem. Soc.* **2009**, *131*, 6050-6051.

(72) Jeong, J.; Kim, M.; Seo, J.; Lu, H.; Ahlawat, P.; Mishra, A.; Yang, Y.; Hope, M. A.; Eickemeyer, F. T.; Kim, M.; et al. Pseudo-Halide Anion Engineering for Alpha- $FAPbI_3$ Perovskite Solar Cells. *Nature* **2021**, *592* (7854), 381-385.

(73) Jiang, X.; Li, H.; Zhou, Q.; Wei, Q.; Wei, M.; Jiang, L.; Wang, Z.; Peng, Z.; Wang, F.; Zang, Z.; et al. One-Step Synthesis of $SnI_2.(DMSO)_x$ Adducts for High-Performance Tin Perovskite Solar Cells. *J. Am. Chem. Soc.* **2021**, *143* (29), 10970-10976.

(74) Jiang, X.; Zang, Z.; Zhou, Y.; Li, H.; Wei, Q.; Nin, Z. Tin Halide Perovskite Solar Cells: An Emerging Thin-Film Photovoltaic Technology. *Acc. Mater. Res.* **2021**, *2*, 210-219.

(75) Ke, W.; Kanatzidis, M. G. Prospects for Low-Toxicity Lead-Free Perovskite Solar Cells. *Nat. Comm.* **2019**, *10* (1), 965.

(76) Pitaro, M.; Tekelenburg, E. K.; Shao, S.; Loi, M. A. Tin Halide Perovskites: From Fundamental Properties to Solar Cells. *Adv. Mater.* **2022**, *34* (1), e2105844.

(77) Smith, P. J. *Chemistry of Tin*; 1998.

(78) Stoumpos, C. C.; Malliakas, C. D.; Kanatzidis, M. G. Semiconducting Tin and Lead Iodide Perovskites with Organic Cations: Phase Transitions, High Mobilities, and Near-Infrared Photoluminescent Properties. *Inorg. Chem.* **2013**, *52* (15), 9019-9038.

(79) Chen, Z.; Wang, J. J.; Ren, Y.; Yu, C.; Shum, K. Schottky Solar Cells Based on $CsSnI_3$ Thin-Films. *Appl. Phys. Lett.* **2012**, *101* (9).

(80) Lanzetta, L.; Webb, T.; Marin-Beloqui, J. M.; Macdonald, T. J.; Haque, S. A. Halide Chemistry in Tin Perovskite Optoelectronics: Bottlenecks and Opportunities. *Angew. Chem. Int. Ed. Engl.* **2023**, *62* (8), e202213966.

(81) Ozaki, M.; Katsuki, Y.; Liu, J.; Handa, T.; Nishikubo, R.; Yakumaru, S.; Hashikawa, Y.; Murata, Y.; Saito, T.; Shimakawa, Y.; et al. Solvent-Coordinated Tin Halide Complexes as Purified Precursors for Tin-Based Perovskites. *ACS Omega* **2017**, *2* (10), 7016-7021.

(82) Wang, C.; Gu, F.; Zhao, Z.; Rao, H.; Qiu, Y.; Cai, Z.; Zhan, G.; Li, X.; Sun, B.; Yu, X.; et al. Self-Repairing Tin-Based Perovskite Solar Cells with a Breakthrough Efficiency Over 11%. *Adv. Mater.* **2020**, *32* (31), e1907623.

(83) Tai, Q.; Guo, X.; Tang, G.; You, P.; Ng, T. W.; Shen, D.; Cao, J.; Liu, C. K.; Wang, N.; Zhu, Y.; et al. Antioxidant Grain Passivation for Air-Stable Tin-Based Perovskite Solar Cells. *Angew. Chem. Int. Ed. Engl.* **2019**, *58* (3), 806-810.

(84) Liu, H.; Wang, L.; Li, R.; Shi, B.; Wang, P.; Zhao, Y.; Zhang, X. Modulated Crystallization and Reduced $V_{OC}$ Deficit of Mixed Lead–Tin Perovskite Solar Cells with Antioxidant Caffeic Acid. *ACS Energy Lett.* **2021**, *6* (8), 2907-2916.

(85) Jokar, E.; Chien, C. H.; Tsai, C. M.; Fathi, A.; Diau, E. W. Robust Tin-Based Perovskite Solar Cells with Hybrid Organic Cations to Attain Efficiency Approaching 10%. *Adv. Mater.* **2019**, *31* (2), e1804835.

(86) Tsai, C.-M.; Lin, Y.-P.; Pola, M. K.; Narra, S.; Jokar, E.; Yang, Y.-W.; Diau, E. W.-G. Control of Crystal Structures and Optical Properties with Hybrid Formamidinium and 2-Hydroxyethylammonium Cations for Mesoscopic Carbon-Electrode Tin-Based Perovskite Solar Cells. *ACS Energy Lett.* **2018**, *3* (9), 2077-2085.

(87) Abdel-Shakour, M.; Chowdhury, T. H.; Matsuishi, K.; Bedja, I.; Moritomo, Y.; Islam, A. High Efficiency Tin Halide Perovskite Solar Cells: The Chemistry of Tin (II) Compounds and their Interaction with Lewis Base Additives During Perovskite Film Formation. *Solar RRL* **2021**, *5*, 2000606.

(88) Song, T. B.; Yokoyama, T.; Stoumpos, C. C.; Logsdon, J.; Cao, D. H.; Wasielewski, M. R.; Aramaki, S.; Kanatzidis, M. G. Importance of Reducing Vapor Atmosphere in the Fabrication of Tin-Based Perovskite Solar Cells. *J. Am. Chem. Soc.* **2017**, *139* (2), 836-842.

(89) Wang, T.; Tai, Q.; Guo, X.; Cao, J.; Liu, C.-K.; Wang, N.; Shen, D.; Zhu, Y.; Lee, C.-S.; Yan, F. Highly Air-Stable Tin-Based Perovskite Solar Cells through Grain-Surface Protection by Gallic Acid. *ACS Energy Lett.* **2020**, *5* (6), 1741-1749.

(90) Song, T.-B.; Yokoyama, T.; Logsdon, J.; Wasielewski, M. R.; Aramaki, S.; Kanatzidis, M. G. Piperazine Suppresses Self-Doping in $CsSnI_3$ Perovskite Solar Cells. *ACS Appl. Energy Mater.* **2018**, *1* (8), 4221-4226.

(91) Gupta, S.; Cahen, D.; Hodes, G. How $SnF_2$ Impacts the Material Properties of Lead-Free Tin Perovskites. *J. Phys. Chem. C* **2018**, *122* (25), 13926-13936.

(92) Li, F.; Fan, H.; Zhang, J.; Huang, J. H.; Wang, P.; Gao, C.; Yang, L. M.; Zhu, Z.; Jen, A. K. Y.; Song, Y.; et al. Trihydrazine Dihydriodide-Assisted Fabrication of Efficient Formamidinium Tin Iodide Perovskite Solar Cells. *Solar RRL* **2019**, *3*, 1900285.

(93) Tsarev, S.; Boldyreva, A. G.; Luchkin, S. Y.; Elshobaki, M.; Afanasov, M. I.; Stevenson, K. J.; Troshin, P. A. Hydrazinium-Assisted Stabilisation of Methylammonium Tin Iodide for Lead-Free Perovskite Solar Cells. *J. Mater. Chem. A* **2018**, *6* (43), 21389-21395.

(94) Li, F.; Zhang, C.; Huang, J. H.; Fan, H.; Wang, H.; Wang, P.; Zhan, C.; Liu, C. M.; Li, X.; Yang, L. M.; et al. A Cation-Exchange Approach for the Fabrication of Efficient Methylammonium Tin Iodide Perovskite Solar Cells. *Angew. Chem. Int. Ed. Engl.* **2019**, *58* (20), 6688-6692.

(95) You, J.; Wang, M.; Xu, C.; Yao, Y.; Zhao, X.; Liu, D.; Dong, J.; Guo, P.; Xu, G.; Luo, C.; et al. Hydrazine Dihydrochloride as A New Additive to Promote the Performance of Tin-Based Mixed Organic Cation Perovskite Solar Cells. *Sustainable Energy Fuels* **2021**, *5* (10), 2660-2667.

(96) Kayesh, M. E.; Matsuishi, K.; Kaneko, R.; Kazaoui, S.; Lee, J.-J.; Noda, T.; Islam, A. Coadditive Engineering with 5-Ammonium Valeric Acid Iodide for Efficient and Stable Sn Perovskite Solar Cells. *ACS Energy Lett.* **2018**, *4* (1), 278-284.

(97) Lin, R.; Xu, J.; Wei, M.; Wang, Y.; Qin, Z.; Liu, Z.; Wu, J.; Xiao, K.; Chen, B.; Park, S. M.; et al. All-Perovskite Tandem Solar Cells with Improved Grain Surface Passivation. *Nat. Energy* **2022**, *603* (7899), 73-78.

(98) Chen, Q.; Luo, J.; He, R.; Lai, H.; Ren, S.; Jiang, Y.; Wan, Z.; Wang, W.; Hao, X.; Wang, Y.; et al. Unveiling Roles of Tin Fluoride Additives in High-Efficiency Low-Bandgap Mixed Tin-Lead Perovskite Solar Cells. *Adv. Energy Mater.* **2021**, *11* (29), 2101045.

(99) Pascual, J. F., M.; Félix, R.; Li, G.; Turren-Cruz, S.-H.; Aldamasy, M. H.; Hartmann, C.; Li, M.; Girolamo, D. D.; Nasti, G.; Hüsam, E.; Wilks, R. G.; Dallmann, A.; Bär, M.; Hoell, A.; Abate, A. Fluoride Chemistry in Tin Halide Perovskites. *Angew. Chem. Int. Ed.* **2021**, *60*, 21583 – 21591.

(100) Takashima, T.; Hashimoto, K.; Nakamura, R. Mechanisms of pH-Dependent Activity for Water Oxidation to Molecular Oxygen by $MnO_2$ Electrocatalysts. *J. Am. Chem. Soc.* **2012**, *134* (3), 1519-1527.

(101) Nakamura, T.; Yakumaru, S.; Truong, M. A.; Kim, K.; Liu, J.; Hu, S.; Otsuka, K.; Hashimoto, R.; Murdey, R.; Sasamori, T.; et al. Sn(IV)-Free Tin Perovskite Films Realized by In- situ Sn(0) Nanoparticle Treatment of the Precursor Solution. *Nat. Comm.* **2020**, *11* (1), 3008.

(102) Li, W.; Li, J.; Li, J.; Fan, J.; Mai, Y.; Wang, L. Addictive-Assisted Construction of All-Inorganic $CsSnIBr_2$ Mesoscopic Perovskite Solar Cells with Superior Thermal Stability up to 473 K. *J. Mater. Chem. A* **2016**, *4* (43), 17104-17110.

(103) Meng, X.; Wu, T.; Liu, X.; He, X.; Noda, T.; Wang, Y.; Segawa, H.; Han, L. Highly Reproducible and Efficient $FASnI_3$ Perovskite Solar Cells Fabricated with Volatilizable Reducing Solvent. *J. Phys. Chem. Lett.* **2020**, *11* (8), 2965-2971.

(104) Xu, X.; Chueh, C.-C.; Yang, Z.; Rajagopal, A.; Xu, J.; Jo, S. B.; Jen, A. K. Y. Ascorbic Acid as An Effective Antioxidant Additive to Enhance the Efficiency and Stability of Pb/Sn-Based Binary Perovskite Solar Cells. *Nano Energy* **2017**, *34*, 392-398.

(105) He, X.; Wu, T.; Liu, X.; Wang, Y.; Meng, X.; Wu, J.; Noda, T.; Yang, X.; Moritomo, Y.; Segawa, H.; et al. Highly Efficient Tin Perovskite Solar Cells Achieved in a Wide Oxygen Concentration Range. *J. Mater. Chem. A* **2020**, *8* (5), 2760-2768.

(106) Pascual, J.; Nasti, G.; Aldamasy, M. H.; Smith, J. A.; Flatken, M.; Phung, N.; Di Girolamo, D.; Turren-Cruz, S.-H.; Li, M.; Dallmann, A.; et al. Origin of Sn(II) Oxidation in Tin Halide Perovskites. *Mater. Adv.* **2020**, *1* (5), 1066-1070.

(107) Saidaminov, M. I.; Spanopoulos, I.; Abed, J.; Ke, W.; Wicks, J.; Kanatzidis, M. G.; Sargent, E. H. Conventional Solvent Oxidizes Sn(II) in Perovskite Inks. *ACS Energy Lett.* **2020**, *5* (4), 1153-1155.

(108) Huynh, M. T.; Anson, C. W.; Cavell, A. C.; Stahl, S. S.; Hammes-Schiffer, S. Quinone 1 $e^-$ and 2 $e^-$/2 $H^+$ Reduction Potentials: Identification and Analysis of Deviations from Systematic Scaling Relationships. *J. Am. Chem. Soc.* **2016**, *138* (49), 15903-15910.

(109) Wrackmeyer, B. ^{119}Sn-NMR Parameters. Annual Reports on NMR Spectroscopy, 1985; pp 73-186.

(110) Burke, J. J.; Lauterbur, P. C. Sn[119] Nuclear Magnetic Resonance Spectra. *J. Am. Chem. Soc.* **2002**, *83* (2), 326-331.

(111) *CRC Handbook of Chemistry and Physics, ed. D. R. Lide, CRC Press LLC, Boca Raton, FL, 81st edn, 2000.*

(112) Yang, S. J.; Choi, J.; Song, S.; Park, C.; Cho, K. Enhancing air-stability and reproducibility of lead-free formamidinium-based tin perovskite solar cell by chlorine doping. *Sol. Energy Mater. Sol. Cells* **2021**, *227*. DOI: 10.1016/j.solmat.2021.111072.

(113) Zhou, J.; Hao, M.; Zhang, Y.; Ma, X.; Dong, J.; Lu, F.; Wang, J.; Wang, N.; Zhou, Y. Chemo-Thermal Surface Dedoping for High-Performance Tin Perovskite Solar Cells. *Matter* **2022**, *5* (2), 683-693.

(114) Liu, H.; Zhang, Z.; Zuo, W.; Roy, R.; Li, M.; Byranvand, M. M.; Saliba, M. Pure Tin Halide Perovskite Solar Cells: Focusing on Preparation and Strategies. *Adv. Energy Mater.* **2022**, *13* (3).

(115) Tong, J.; Jiang, Q.; Ferguson, A. J.; Palmstrom, A. F.; Wang, X.; Hao, J.; Dunfield, S. P.; Louks, A. E.; Harvey, S. P.; Li, C.; et al. Carrier Control in Sn–Pb Perovskites via 2D Cation Engineering for All-Perovskite Tandem Solar Cells with Improved Efficiency and Stability. *Nat. Energy* **2022**, *7* (7), 642-651.

(116) Hu, M.; Zhang, Y.; Gong, J.; Zhou, H.; Huang, X.; Liu, M.; Zhou, Y.; Yang, S. Surface Sn(IV) Hydrolysis Improves Inorganic Sn–Pb Perovskite Solar Cells. *ACS Energy Lett.* **2023**, *8* (2), 1035-1041.

(117) Song, D.; Li, H.; Xu, Y.; Yu, Q. Amplifying Hole Extraction Characteristics of PEDOT:PSS via Post-treatment with Aromatic Diammonium Acetates for Tin Perovskite Solar Cells. *ACS Energy Lett.* **2023**, *8* (8), 3280-3287.

(118) Zhao, J.; Zhang, Z.; Li, G.; Aldamasy, M. H.; Li, M.; Abate, A. Dimensional Tuning in Lead-Free Tin Halide Perovskite for Solar Cells. *Adv. Energy Mater.* **2023**, *13* (13).

(119) Hossain, T.; Joy, S.; Draffen, K.; Bright, R.; Johnson, S.; Graham, K. R. Oxidation in Tin Halide Perovskites: Influence of Acidic and Basic Additives. *ACS Appl. Energy Mater.* **2023**, *6* (24), 12334-12342.

(120) Ricciarelli, D.; Meggiolaro, D.; Ambrosio, F.; Angelis, F. D. Instability of Tin Iodide Perovskites: Bulk p-Doping versus Surface Tin Oxidation. *ACS Energy Lett.* **2020**, *5* (9), 2787-2795.

(121) Milot, R. L.; Klug, M. T.; Davies, C. L.; Wang, Z.; Kraus, H.; Snaith, H. J.; Johnston, M. B.; Herz, L. M. The Effects of Doping Density and Temperature on the Optoelectronic Properties of Formamidinium Tin Triiodide Thin Films. *Adv. Mater.* **2018**, *30* (44), e1804506.

(122) Meggiolaro, D.; Ricciarelli, D.; Alasmari, A. A.; Alasmary, F. A. S.; De Angelis, F. Tin versus Lead Redox Chemistry Modulates Charge Trapping and Self-Doping in Tin/Lead Iodide Perovskites. *J. Phys. Chem. Lett.* **2020**, *11* (9), 3546-3556.

(123) Shi, T.; Zhang, H.-S.; Meng, W.; Teng, Q.; Liu, M.; Yang, X.; Yan, Y.; Yip, H.-L.; Zhao, Y.-J. Effects of Organic Cations on the Defect Physics of Tin Halide Perovskites. *J. Mater. Chem. A* **2017**, *5* (29), 15124-15129.

(124) Naito, T.; Takagi, M.; Tachikawa, M.; Yamashita, K.; Shimazaki, T. Theoretical Study of the Molecular Passivation Effect of Lewis Base/Acid on Lead-Free Tin Perovskite Surface Defects. *J. Phys. Chem. Lett.* **2023**, *14* (29), 6695-6701.

(125) Treglia, A.; Ambrosio, F.; Martani, S.; Folpini, G.; Barker, A. J.; Albaqami, M. D.; De Angelis, F.; Poli, I.; Petrozza, A. Effect of Electronic Doping and Traps on Carrier Dynamics in Tin Halide Perovskites. *Mater. Horizon* **2022**, *9* (6), 1763-1773.

(126) Jokar, E.; Cheng, P.-Y.; Lin, C.-Y.; Narra, S.; Shahbazi, S.; Diau, E. W.-G. Enhanced Performance and Stability of 3D/2D Tin Perovskite Solar Cells Fabricated with a Sequential Solution Deposition. *ACS Energy Lett.* **2021**, *6* (2), 485-492.

(127) Wang, F.; Jiang, X.; Chen, H.; Shang, Y.; Liu, H.; Wei, J.; Zhou, W.; He, H.; Liu, W.; Ning, Z. 2D-Quasi-2D-3D Hierarchy Structure for Tin Perovskite Solar Cells with Enhanced Efficiency and Stability. *Joule* **2018**, *2*, 2732-2743.

(128) Nasti, G.; Aldamasy, M. H.; Flatken, M. A.; Musto, P.; Matczak, P.; Dallmann, A.; Hoell, A.; Musiienko, A.; Hempel, H.; Aktas, E.; et al. Pyridine Controlled Tin Perovskite Crystallization. *ACS Energy. Lett.* **2022**, *7* (10), 3197-3203.

(129) Aktas, E.; Poli, I.; Ponti, C.; Li, G.; Olivati, A.; Girolamo, D. D.; Alharthi, F. A.; Li, M.; Polamares, E.; Petrozza, A.; et al. One-Step Solution Deposition of Tin-Perovskite onto a Self-Assembled Monolayer with a DMSO-Free Solvent System. *ACS Energy Lett.* **2023**, *8*, 5170-5174.

(130) Kumar, M. H.; Dharani, S.; Leong, W. L.; Boix, P. P.; Prabhakar, R. R.; Baikie, T.; Shi, C.; Ding, H.; Ramesh, R.; Asta, M.; et al. Lead-free Halide Perovskite Solar Cells with High Photocurrents Realized through Vacancy Modulation. *Adv. Mater.* **2014**, *26* (41), 7122-7127.

(131) Liao, W.; Zhao, D.; Yu, Y.; Grice, C. R.; Wang, C.; Cimaroli, A. J.; Schulz, P.; Meng, W.; Zhu, K.; Xiong, R. G.; et al. Lead-Free Inverted Planar Formamidinium Tin Triiodide Perovskite Solar Cells Achieving Power Conversion Efficiencies up to 6.22%. *Adv. Mater.* **2016**, *28* (42), 9333-9340.

(132) Liu, X.; Wang, Y.; Wu, T.; He, X.; Meng, X.; Barbaud, J.; Chen, H.; Segawa, H.; Yang, X.; Han, L. Efficient and Stable Tin Perovskite Solar Cells Enabled by Amorphous-Polycrystalline Structure. *Nat. Comm.* **2020**, *11* (1), 2678.

(133) Marshall, K. P.; Walker, M.; Walton, R. I.; Hatton, R. A. Enhanced Stability and Efficiency in Hole-Transport-Layer-Free CsSnI$_3$ Perovskite Photovoltaics. *Nat. Energy* **2016**, *1* (12), 16178.

(134) Joy, S.; Atapattu, H. R.; Sorensen, S.; Pruett, H.; Olivelli, A. B.; Huckaba, A. J.; Miller, A.-F.; Graham, K. R. How Additives for Tin Halide Perovskites Influence the Sn$^{4+}$ Concentration. *J. Mater. Chem. A* **2022**, *10* (25), 13278-13285.

(135) Meggiolaro, D.; Gregori, L.; De Angelis, F. Formation of a Mixed Valence Sn$_3$F$_8$ Phase May Explain the SnF$_2$ Stabilizing Role in Tin-Halide Perovskites. *ACS Energy Lett.* **2023**, *8* (5), 2373-2375.

(136) Brennan, M. C.; Draguta, S.; Kamat, P. V.; Kuno, M. Light-Induced Anion Phase Segregation in Mixed Halide Perovskites. *ACS Energy Lett.* **2018**, *3*, 204-213.

(137) Xiao, Z.; Zhao, L.; Tran, N. L.; Lin, Y. L.; Silver, S. H.; Kerner, R. A.; Yao, N.; Kahn, A.; Scholes, G. D.; Rand, B. P. Mixed-Halide Perovskites with Stabilized Bandgaps. *Nano Lett.* **2017**, *17*, 6863-6869.

(138) Ighodalo, K. O.; Chen, W.; Liang, Z.; Shi, Y.; Chu, S.; Zhang, Y.; Khan, R.; Zhou, H.; Pan, X.; Ye, J.; et al. Negligible Ion Migration in Tin-Based and Tin-Doped Perovskites. *Angew. Chem. Int. Ed.* **2023**, *62* (5), e202213932.

(139) Shahi, M.; Atapattu, H. R.; Baustert, K. N.; Anthony, J. E.; Brill, J. W.; Johnson, S.; Graham, K. R. Probing Transport Energies and Defect States in Organic Semiconductors Using Energy Resolved Electrochemical Impedance Spectroscopy. *Adv. Mater. Interfaces* **2023**, *10* (19).

(140) Xiao, M.; Gu, S.; Zhu, P.; Tang, M.; Zhu, W.; Lin, R.; Chen, C.; Xu, W.; Yu, T.; Zhu, J. Tin-Based Perovskite with Improved Coverage and Crystallinity through Tin-Fluoride-Assisted Heterogeneous Nucleation. *Adv. Optical Mater.* **2017**, *6* (1), 1700615.

(141) Lanzetta, L.; Webb, T.; Zibouche, N.; Liang, X.; Ding, D.; Min, G.; Westbrook, R. J. E.; Gaggio, B.; Macdonald, T. J.; Islam, M. S.; et al. Degradation Mechanism of Hybrid Tin-based Perovskite Solar Cells and the Critical Role of Tin (IV) Iodide. *Nat. Comm.* **2021**, *12* (1), 2853.

(142) Girolamo, D. D.; Blundo, E.; Folpini, G.; Ponti, C.; Li, G.; Aldamasy, M. H.; Iqbal, Z.; Pascual, J.; Nasti, G.; Li, M.; et al. Energy Distribution in Tin Halide Perovskite. *Solar RRL* **2021**, *6* (8), 2100825.

(143) Mahesh, S.; Ball, J. M.; Oliver, R. D. J.; McMeekin, D. P.; Nayak, P. K.; Johnston, M. B.; Snaith, H. J. Revealing the Origin of Voltage Loss in Mixed-Halide Perovskite Solar Cells. *Energy Environ. Sci.* **2020**, *13* (1), 258-267.

(144) Lee, S. J.; Shin, S. S.; Im, J.; Ahn, T. K.; Noh, J. H.; Jeon, N. J.; Seok, S. I.; Seo, J. Reducing Carrier Density in Formamidinium Tin Perovskites and Its Beneficial Effects on Stability and Efficiency of Peorvskite Solar Cells. *ACS Energy Lett.* **2018**, *3*, 46-53.

(145) Ke, W.; Stoumpos, C. C.; Spanopoulos, I.; Chen, M.; Wasielewski, M. R.; Kanatzidis, M. G. Diammonium Cations in the FASnI$_3$ Perovskite Structure Lead to Lower Dark Currents and More Efficient Solar Cells. *ACS Energy Lett.* **2018**, *3* (7), 1470-1476.

(146) Khadka, D. B.; Shirai, Y.; Yanagida, M.; Tadano, T.; Miyano, K. Alleviating Defect and Oxidation in Tin Perovskite Solar Cells Using a Bidentate Ligand. *Chem. Mater.* **2023**, *35* (11), 4250-4258.

(147) Futscher, M. H.; Deibel, C. Defect Spectroscopy in Halide Perovskites Is Dominated by Ionic Rather than Electronic Defects. *ACS Energy Lett.* **2021**, *7* (1), 140-144.

(148) Zhang, Z.; Huang, Y.; Wang, C.; Jiang, Y.; Jin, J.; Xu, J.; Li, Z.; Su, Z.; Zhou, Q.; Zhu, J.; et al. Green-Antisolvent-Regulated Distribution of P-type Self-Doping Enables Tin Perovskite Solar Cells with An Efficiency of Over 14%. *Energy Environ. Sci.* **2023**, *16* (8), 3430-3440.

(149) Zhou, S.; Zhu, S.; Guan, J.; Wang, R.; Zheng, W.; Gao, P.; Lu, X. Confronting the Air Instability of Cesium Tin Halide Perovskites by Metal Ion Incorporation. *J. Phys. Chem. Lett.* **2021**, *12* (45), 10996-11004.

VITA

# SYED RAHMATH ULLAH JOY

**EDUCATION**

**University of Kentucky, Lexington, KY**                                              *05/2024*
Ph.D. in Chemistry
**Eastern Illinois University, Charleston, IL**                                          *2018*
M.S. in Chemistry
**University of Dhaka**, **Bangladesh**                                               *2015*
B.S. in Applied Chemistry & Chemical Engineering

**RESEARCH EXPERIENCE**

**University of Kentucky,** Lexington, KY
*Research Assistant*                                                              *2019-Present*

**Eastern Illinois University,** Charleston, IL
*Research Assistant*                                                              *2016-2018*

**PUBLICATIONS**

1. **Joy, S.;** Hossain, T.; Tichy, A.; Johnson, S.; Graham, K. R. Defects Modulation *via* $SnX_2$ Additives in $FASnI_3$ Perovskite Solar Cells. *J. Phys. Chem. Lett.* **2024,** *15*, 14, 3851–3858.

2. Nguyen-Dang, T.; Kaiyasuan, C.; Li, K.; Chae, S.; Yi, A.; **Joy, S.**; Kim, J. Y.; Pallini, F.; Bao, A. S. T.; Harrision, K.; Graham, K. R.; Nuckolls, C.; Nguyen, T.-Q. Air-Stable Perylene Diimide Trimer Material for n-type Organic Electrochemical Transistors." *Adv. Mater.* **2024**.

3. Liu, T.; Scheidt, R. A.; Zheng, X.; **Joy, S.**; Jiang, Q.; Atapattu, H. R.; Chen, M.; Pruett, H.; Zhu, K.; Luther, J. M.; Beard, M. C.; Graham, K. R. Tuning Interfacial Energetics with Surface Ligands to Enhance Perovskite Solar Cell Performance. *Cell Reports Phys. Sci.* **2023**.

4. Hossain, T.; **Joy, S.**; Bright, R.; Johnson, S.; Graham, K. R. Oxidation in Tin Halide Perovskite: Influence of Acidic and Basic Additives. *ACS Appl. Energy Mater.* **2023**, 6, *24*, 12334–12342.

5. Lungwitz, D.; **Joy, S.**; Mansour, A. E.; Opitz, A.; Karunasena, C.; Li, H.; Panjwani, N. A.; Moudgil, K.; Tang, K.; Behrends, J.; Barlow, S.; Marder, S. R.; Bredas, J.-L.; Graham, K. R.; Koch, N.; Kahn, A. Spectral Signatures of a Negative Polaron in a Doped Polymer Semiconductor. *J. Phys. Chem. Lett.* **2023**, 14, *24*, 5633–5640.

6. **Joy, S.**; Atapattu, H. R.; Sorensen, S.; Pruett, H.; Olivelli, A. B.; Huckaba, A. J.; Miller, A.-F.; Graham, K. R. How Additives for Tin Halide Perovskites Influence the $Sn^{4+}$ Concentration. *J. Mater. Chem. A* **2022**, 10, 13278–13285.

7. Uddin, M. A.; Hossain, T.; Kothalawala, N. L.; **Joy, S.**; Kim, D.-Y.; Graham, K. R. Multifunctional Thiol-Containing Additives for Improved Photoluminescence and

Photovoltaic Performance of $Cs_{0.15}FA_{0.85}PbI_3$ Organic Metal Halide Perovskites. *ACS Appl. Electr. Mater.* **2022**, 4, *3*, 903–909.

## PRESENTATIONS

1. **Joy, S.**; Atapattu, H. R.; Sorensen, S.; Pruett, H.; Olivelli, A. B.; Huckaba, A. J.; Miller, A.-F.; Graham, K. R. "Effects of Additives and their Redox Potential on the Sn(IV) Concentration in Tin Halide Perovskites" *ACS Spring Meeting*, March **2023**, Indianapolis, IN. *Oral presentation.*

2. **Joy, S.**; Atapattu, H. R.; Sorensen, S.; Pruett, H.; Olivelli, A. B.; Huckaba, A. J.; Miller, A.-F.; Graham, K. R. "Effects of Additives and their Redox Potential on the Sn(IV) Concentration in Tin Halide Perovskites" *Naff Symposium*, University of Kentucky, March **2022**, Lexington, KY. *Poster presentation.*

3. **Joy, S.**; Atapattu, H. R.; Sorensen, S.; Pruett, H.; Olivelli, A. B.; Huckaba, A. J.; Miller, A.-F.; Graham, K. R. "Effects of Additives and their Redox Potential on the Sn(IV) Concentration in Tin Halide Perovskites" *Gordon Research Conference*, June **2022**, Ventura, CA. *Poster presentation.*

4. **Joy, S.**; Graham, K. R. "Development of Tin Halide Perovskite Photovoltaics - Towards Improved Stability and Air Tolerant Processing" *NSF EPSCoR Meeting*, February **2023**, Lexington, KY. *Poster Presentation.*

5. **Joy, S.**; Graham, K. R. "Toward Printed Silver Nanowire-Polymer Composite Electrode for Solution-Processed Perovskite Solar Cells" *NSF EPSCoR Meeting*, Sep **2020**, Lexington, KY. *Oral Presentation.*

## LEADERSHIP and AWARD

- Secretary, Materials Research Society (MRS)
  University of Kentucky Chapter                                          *05/2023-05/2024*
- Steckler fellowship, University of Kentucky                             *2021*
- Steckler fellowship, University of Kentucky                             *2024*